Nonlinear Energy Harvesting

A thesis submitted to the University of Sheffield
for the degree of Doctor of Philosophy in the Faculty of Engineering

by

P. L. Green

Department of Mechanical Engineering

University of Sheffield

October 2012

Contents

ABSTRACT

The concept of harvesting electrical energy from ambient vibration sources has been a popular topic of research in recent years. The motivation behind this research is largely due to recent advancements in microelectromechanical systems (MEMS) technology - specifically the construction of small low powered sensors which are capable of being placed in inaccessible or hostile environments. The main drawback with these devices is that they require an external power source. For example, if one considers large networks of low powered sensors (such as those which may be attached to a bridge as part of a structural health monitoring system) then one can envisage a scenario where energy harvesters are used to transfer the vibration energy of the bridge into electrical energy for the sensors. This would alleviate the need for batteries which, in this scenario, would be difficult to replace.

Initial energy harvester designs suffered from a major flaw: they were only able to produce useful amounts of power if they were excited close to their resonant frequency. This narrow bandwidth of operation meant that they were poorly suited to harvesting energy from ambient vibration sources which are often broadband and have time dependent dominant frequencies. This led researchers to consider the concept of nonlinear energy harvesting - the hypothesis that the performance of energy harvesters could be improved via the deliberate introduction of dynamic nonlinearities. This forms the main focus of the work in this thesis.

The first major part of this work is concerned with the development of an experimentally validated physical-law based model of an electromagnetic energy harvester with Duffing-type nonlinearities. To this end, a self-adaptive differential evolution

(SADE) algorithm is used in conjunction with experimental data to estimate the parameters needed to accurately model the behaviour of the device. During this investigation it is found that the response of the energy harvesting device in question is very sensitive to the effects of friction. Consequently, a detailed study is undertaken with the aim of finding whether the model performance could be improved by accounting for this complex nonlinear phenomenon. After investigating several different friction models, a reliable and extensively validated digital model of a nonlinear energy harvesting device is realised. With the appropriate equations of motion identified, analytical approximation methods are used to analyse the response of the device to sinusoidal excitations.

The motivation for the second main part of this work arises from the fact that ambient excitations are often stochastic in nature. As a result, much of the work in this section is directed towards gaining an understanding of how nonlinear energy harvesters respond to random excitations. This is an interesting problem because, as a result of the random excitation, it is impossible to say *exactly* how such a device will respond - the problem must be tackled using a probabilistic approach. To this end, the Fokker-Planck-Kolmogorov (FPK) equation is used to develop probability density functions describing how the nonlinear energy harvester in question responds to Gaussian white noise excitations. By conducting this analysis, previously unrecognised benefits of Duffing-type nonlinearities in energy harvesters are identified along with important findings with regards to device electrical optimisation. As for friction effects, the technique of equivalent linearisation is employed alongside known solutions of the FPK equation to develop expressions approximating the effect of friction on randomly excited energy harvesters. These results are then validated using Monte-Carlo methods thus revealing important results about the interaction between Duffing-type and friction nonlinearities.

Having investigated sinusoidal and random excitations, the final part of this work focuses on the application of nonlinear energy harvesting techniques to real energy harvesting scenarios. Excitation data from human walking motion and bridge vibrations is used to excite digital models of a variety of recently proposed nonlinear energy harvesters. This analysis reveals important information with respect to how well energy harvesting solutions developed under the assumption of Gaussian white noise excitations can be extended to real world scenarios.

ACKNOWLEDGEMENTS

I would like to thank Neil Sims for his excellent supervision during my PhD. His ability to provide guidance when needed while also allowing me the freedom to explore my own research ideas (even if some of them were a bit rubbish) has made the last three years a very enjoyable experience and has inspired me continue researching after my PhD. I must also thank Keith Worden who provided much additional help and support (even though he didn't really have to). I look forward to tackling more 'hard sums', talking more of cats and eating more curries with Keith! I would also like to show my gratitude to my second supervisor Kais Atallah for taking the time to very patiently explain some simple electrical engineering concepts to a mechanical engineer. Of course, I must thank everyone in the Sheffield Dynamics Research group past and present (too many to name!) not only for making such a friendly environment in which to work but also for being such excellent and inspirational researchers - it makes me proud to be part of such an excellent group! Finally I would like to thank my family, Rach and Luke simply for remaining lovely people over the ups and downs of the last three years as well as Penny the cat for maintaining a high standard of fluffiness and cuteness.

Chapter 1

INTRODUCTION

1.1 Motivation

The overall goal of energy harvesting (sometimes referred to as energy scavenging) is to create electrical energy from an energy source which is already present in the environment. Possible ambient sources include light, thermal energy, volume flow and mechanical energy. This work focuses on the harvesting of energy from ambient mechanical vibrations. This is a topic which has not received much attention until relatively recently due to the small amount of energy available for capture (when compared with other ambient sources such as solar power). However, recent developments in small low powered sensor systems has made the concept of harvesting energy from ambient vibrations more attractive - as discussed more in the following paragraphs.

Recent improvements in Microelectromechanical systems (MEMS) technology has led to the development of small electronic devices which are low power, low weight, cheap to produce and, because of their small size, can be applied to a large variety of scenarios [1, 2, 3]. In [1] it is shown that, using an assortment of different sensing techniques, MEMS technology can be used to develop sensors of millimeter-order size that can accurately measure displacement, velocity, acceleration, torques, stress and strain. Such technology is not limited to mechanical applications, in [2] and [3] it is shown that MEMS sensors can also be used in the biomedical domain (devices which can detect cells, proteins or measure blood count for example) as well as the thermo-fluid domain (pressure, fluid flow, viscosity and temperature sensors). Consequently, MEMS technology can be now be found in modern constructions such as pacemakers [4] and electrical stimulation pain management devices [5, 6]. It has also been suggested that such small sensors could form part of a wearable network of autonomous sensor systems which can monitor the health and/or comfort of an individual [7]. Additionally, using small wireless devices (as suggested in [8]) one can envisage a situation where large networks of MEMS devices are used as part of a structural health monitoring system.

All of these devices will, of course, require a supply of electrical power - an obvious choice of power source being the battery. There are several disadvantages to this approach: batteries can by bulky, they have a finite life and they contain hazardous chemicals. Furthermore, the need to replace batteries would make it difficult to have MEMS devices that are completely embedded in structures, in hostile environments or difficult to access locations (upon a bridge, or within the body of a car tyre for example). This need for an alternative power source of infinite life for MEMS sensors forms one of the main motivations behind the energy harvesting research detailed within this thesis.

Moving away from MEMS applications it has also been suggested that, as vibrational energy harvesters[1] are essentially removing kinetic energy from a vibration source, they could be used to simultaneously suppress the vibrations of a host structure while creating electrical energy [9] for low powered sensors. Clearly, for this to be effective, the size of the device has to be of significance when compared with that of the host structure. While this is certainly an application which is worthy of further research, this thesis focuses on the development of small scale energy harvesters whose size is small compared to the host structure to which they are attached.

1.2 Objectives of this work

The main objective of the work in this thesis is to investigate whether one can improve the performance of energy harvesting devices through the deliberate intro-

---

[1] From now on, the term ‘energy harvester’ will be used to refer to the vibrational variety only.

duction of dynamic nonlinearities. This forms an interesting research topic for a variety of reasons. Firstly, it is clear that one cannot simply look for solutions which enhance the dynamic response of such a device - one must also carefully consider the device electronics and electromechanical transfer mechanism. Secondly, one must think carefully about the scenarios in which energy harvesters are likely to be used. While much of the early work in this field was focused on the response of energy harvesters to sinusoidal excitations it was soon realised that this was not a sufficient representation of the majority of ambient excitation sources. As an illustrative example one can consider a device which is designed to harvest energy from bridge vibrations. One could hardly expect such an ambient excitation to take the form of a monotone sinusoid - its nature will depend on so many variables (traffic, wind speed, temperature etc.) that the signal may actually appear to be random. In actuality this uncertainty about excitation type forms one of the biggest challenges for researchers aiming to successfully develop energy harvesters - a significant portion of this thesis is devoted towards investigating the role of nonlinear dynamics in randomly excited energy harvesters. Once these issues have been addressed there is still the added complication of efficient energy storage, although the work shown herein primarily focuses on device dynamics.

Clearly, the harvesting of energy from ambient vibrations is an interesting challenge which can be tackled from both a mechanical and an electrical perspective. In this thesis, the research challenges associated with energy harvesting are approached from the perspective of a nonlinear dynamist although, as will be shown in Chapter 6, this has not prevented the realisation of important conclusions with regards to device electronics.

1.3 Outline of chapters

This thesis is written such that, by reading front to back, the reader can see how energy harvesting research has changed over recent years. The hope is that this will not only give the reader an outline of the research that has been conducted, but also to give an idea of the trends that have been followed in the energy harvesting community. In the final chapters, areas where future research should be focused are proposed.

Chapter 2 - Literature review

This chapter is concerned with the description of energy harvesting literature relevant to this thesis. This begins with a brief description of various electromechanical transducer mechanisms as well as some of the key papers which, it can be argued, pioneered energy harvesting as a research topic. The remainder of the chapter is dedicated to a review of proposed nonlinear energy harvesting techniques. Of particular relevance to this thesis is a description of a monostable energy harvester which features hardening spring Duffing-type nonlinearities. This device will frequently be referred to as the ‘Mann and Sims device’ and is the subject of focus in much of this thesis.

Chapter 3 - Experiment

As described previously, the layout of this thesis is designed to reflect trends in energy harvesting work. With that in mind, this chapter is devoted towards developing an understanding of the physics governing the behavior of energy harvesting devices. Consequently, a physical-law based model of the Mann and Sims device is developed and extensively validated using a series of experimental tests. A key conclusion from this chapter is the fact that, to effectively model such devices, one must consider the effects of unintended nonlinearities (friction in this case) as well as those which have been deliberately introduced to enhance device performance.

Chapter 4 - Harmonic excitations

With a reliable physical model of a nonlinear energy harvester developed and validated, the aim of this chapter is to describe the response of the device to sinusoidal excitations. This is harmonious with early energy harvesting research in which it was assumed that ambient vibration sources would be of a sinusoidal nature. After a brief description of the various methods which one can use to analyse nonlinear systems with this type of excitation, the method of harmonic balance is used to demonstrate the effect of different types of nonlinearity on device performance. It is shown that a significant change in device performance can be witnessed as a result of a relatively small change in friction. As well as this, expressions are developed which are shown to accurately predict when friction effects will prevent energy harvesters from functioning.

Chapter 5 - Random excitations: Monte Carlo Simulation

The discernment that ambient vibration sources are often of a stochastic nature led to a number of authors focusing specifically on understanding how energy harvesters respond to random excitations - this is also the focus of chapters 5, 6 and 7. This forms a particularly interesting challenge as the nature of such an excitation compels one to approach the problem from a probabilistic point of view as apposed to the deterministic approaches detailed in Chapter 4.

In Chapter 5 Monte Carlo simulations are used to analyse the response of the Mann and Sims energy harvester to white and coloured noise excitations. As part of this analysis the method of dimensional analysis is used to arrange the parameters of the Mann and Sims device into dimensionless groups. This is for two reasons. Firstly, it allows the response of all energy harvesters of this type to be analysed regardless of device dimensions. Secondly, by conducting experiments using varying amplitudes of excitation it is shown that one can analyse the effects of changing the dimensionless group which contained the nonlinear stiffness term without having to actually alter the nonlinear term experimentally. This allowed the energy harvester model developed in Chapter 3 to be validated experimentally over a region of parameter space. With regards to Gaussian white noise excitations it is shown that Duffing-type nonlinearities cannot enhance the power output of the Mann and Sims energy harvester and the detrimental effects of frictional losses are demonstrated. This analysis is then extended to the case of coloured noise excitations where it is shown that hardening spring nonlinearities can be employed as a resonance tuning mechanism.

Chapter 6 - Random excitations: Fokker-Planck-Kolmogorov equation

This chapter utilises the Fokker-Planck-Kolmogorov (FPK) equation to develop an analytical expression detailing the response of the Mann and Sims energy harvester to a Gaussian white noise excitation. This expression proves to be more informative than the Monte Carlo simulations of Chapter 5 and reveals several important findings with regards to energy harvester design. Firstly it is shown that Duffing-type nonlinearities can be used to reduce the rattle-space of the Mann and Sims device without harming power output thus allowing one to reduce device size without effecting performance. An expression detailing the effect of the nonlinear spring term on the displacement variance of the device is shown and validated using Monte Carlo simulations. Secondly, it is shown that the optimum load resistance of such a device is not equal to its coil resistance (as dictated by the principle of impedance matching) but is in fact a function of its flux displacement relationship. This finding is then validated experimentally.

Chapter 7 - Random excitations: Equivalent Linearisation

The discussion in Chapter 6 is limited to the study of Duffing-type nonlinearities specifically and does not address the nonlinear friction effects owing to difficulties in solving the corresponding FPK equation. Consequently, the aim of this chapter is develop analytical expressions approximating the effects of Duffing-type and friction nonlinearities on the Mann and Sims device using the method of Equivalent Linearisation.

In Chapter 6 an expression was derived detailing the effect of Duffing-type nonlinearities on the displacement variance of the Mann and Sims device although the complexity of the expression made it difficult to interpret. Consequently, in this chapter a relatively simple expression is developed which, using Monte Carlo simulations, is shown to closely approximate the benefits of the spring nonlinearity with regards to device size. As well as this an expression approximating the effect of friction on the average power output of the device is derived and, again, validated using Monte Carlo simulations.

Chapter 8 - Ambient excitations

The aim of this chapter is to highlight important challenges which must be overcome before energy harvesters can be successfully implemented in real world scenarios. Specifically, using experimental data of real ambient vibration sources, this work shows how difficult it is to implement current nonlinear energy harvesting solutions in a real scenario. Much of this chapter is devoted to describing where energy harvesting research should be focused in the future.

Chapter 9 - Conclusions

Conclusions from this work are drawn. References and appendices follow.

Chapter 2

LITERATURE REVIEW

2.1 Introduction

What follows in this chapter is a discussion of energy harvesting literature relevant to the work in this thesis. The first parts of this chapter focus on describing energy harvester transducer mechanisms before providing a summary of some relatively early works - most of which are focused on the response of linear energy harvesters to sinusoidal excitations. Following this, the focus shifts to the discussion of devices which possess nonlinearities and/or are subjected to random excitation conditions - two subject areas which are analysed in detail in this thesis.

2.2 Comparing energy harvesting technologies

While this thesis is concerned only with the harvesting of energy from ambient vibrations it is instructive to briefly discuss and compare other forms of ambient energy harvesting. One of the most well-known forms of energy harvesting is solar power. This technology uses photo-voltaic conversion to generate electrical energy from light. When in direct sunlight solar cells have the largest power density of all current energy harvesting technologies but will perform poorly in dim ambient light conditions and cannot be used in embedded applications [10]. Thermoelectric technology has been developed which, using the Seebeck effect, can convert thermal energy into electrical energy. While the power output of such devices is relatively low ($\approx 1\mu W$) they have been used to successfully supply power to pacemakers [11]. Table 2.1 shows a comparison between the power density of the afore mentioned energy harvesting technologies (this was originally published in [8]). For a more detailed comparison the work [12] is recommended.

Harvesting Technology	Power Density ($\mu W/cm^3$)
Solar (outdoors)	15000 - Direct sun, 150 Cloudy day
Solar (indoors)	6 (office desk)
Vibrations (piezoelectric conversion)	250
Vibrations (electrostatic conversion)	50
Thermoelectric	15 at 10 C gradient

Table 2.1: The power densities of different energy harvesting technologies (originally published in [8]).

2.3 Energy conversion

Clearly, energy harvesters require a mechanism that will transfer mechanical energy into the electrical domain. In [13, 14, 10] it is stated that this can be achieved using three different methods: electromagnetic, piezoelectric and electrostatic.

2.3.1 Electromagnetic

Electromagnetic energy harvesters are based on Faraday's law of induction - the property that a change in the magnetic flux of a circuit will result in the induction of an electromotive force (EMF). Typically, this is achieved by constructing a device such that the ambient vibration source excites a permanent magnet thus resulting in relative motion between the magnet and a coil of wire around the outer shell of the device. This relative motion results in a time varying magnetic flux which, in turn, generates an EMF in the coil. This work will mostly be dedicated to energy devices of the electromagnetic variety and, consequently, this method of transduction will be discussed in more detail in Chapter 3.

2.3.2 Piezoelectric

When subjected to mechanical strain, piezoelectric materials become electrically polarised. Clearly, such materials have great potential with regards to energy harvesting applications. Many different piezoelectric energy harvesting solutions have been proposed, the majority of which use an ambient vibration source to induce strain in a piezoelectric material. Often this takes the form of a cantilever beam with a piezoceramic layer - as shown in Figure 2.1.

2.3.3 Electrostatic

Electrostatic generators use capacitors to transfer mechanical energy into the electrical domain. Typically, these devices rely on an initial voltage source to create equal but opposite amount of charge on the plates of a capacitor. As a consequence of this charge accumulation, an electrostatic force is generated between the two plates. An ambient vibration source is then used to work against this electrostatic force which results in a change in capacitance and, consequently, an electromotive force being induced in the device circuitry.

The obvious disadvantage of electrostatic generators is their need for an external power source and, ergo, the majority of energy harvesting research has focused on the use of electromagnetic or piezoelectric transduction mechanisms (at least with regards to device dynamics).

2.4 Linear Resonance Energy Harvesting

In one of the earliest studies on energy harvester dynamics [13] an energy harvesting device was proposed which relied on electromagnetic induction. To achieve this, a permanent magnet was attached to a vibrating base via a linear spring such that, when excited, the magnet oscillated within the coil. The device was modelled as a linear, base excited, mass-spring-damper where the damper was used to represent a combination of parasitic losses and the transfer of energy from the mechanical to the electrical domains (see Figure 2.2). The assumption that the electromechanical coupling can be modelled as an additional viscous damping term was employed in

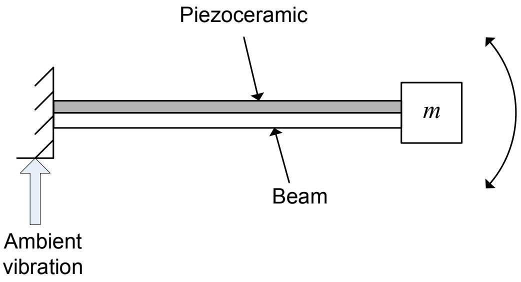

Figure 2.1: Schematic diagram of cantilever piezoelectric device.

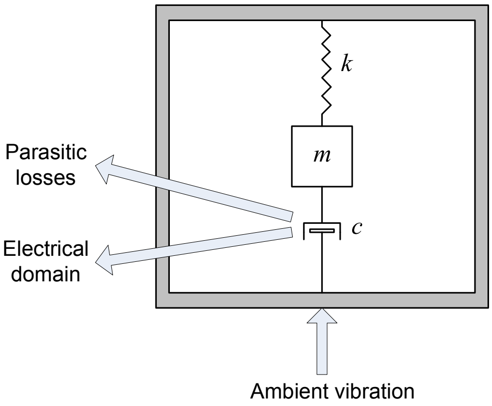

Figure 2.2: Schematic diagram of the device proposed by Williams and Yates [13].

several works ([13, 14, 10, 15, 16]) and will be discussed in more detail in Chapter 3.

Exciting the device with a sinusoidal base excitation of the form $y = Y \sin(\omega t)$ and assuming that the mass of the device was negligible relative to the mass of the excitation source, in [13] an expression for the average power output per cycle of the device was shown to be:

$$p_{av} = \frac{\zeta \omega^3 \omega_r^3 Y^2 m}{(1-\omega_r^2)^2 + (2\zeta\omega_r)^2}, \tag{2.1}$$

where ω_r is the ratio of excitation frequency to natural frequency of the device, ζ is the damping ratio (assuming that all energy losses are accounted for by the electromechanical coupling), m is the mass of the magnet and Y is the amplitude of the displacement. Consequently, when excited at resonance (such that $\omega_r = 1$):

$$p_{av(res)} = \frac{\omega^3 Y^2 m}{4\zeta}. \tag{2.2}$$

These expressions were frequently used in early energy harvesting papers [8, 14, 10, 15] and so their derivations are shown in Appendix B.1.

Upon studying equations (2.1) and (2.2) one can see that the power generated is proportional to the cube of the excitation frequency which, in [13], led to the conclusion that 'the generator is likely to produce much more power in applications where there is a fairly high frequency of vibration, and is likely to perform poorly at low frequencies'. However, in [8] it is stated that 'the converter should be designed to resonate at the lowest fundamental frequency in the input spectrum'. To clarify what may appear to be two contradictory statements one must recall that equations (2.1) and (2.2) are derived assuming that the base *displacement* amplitude is independent of excitation frequency, i.e.:

$$y = Y\sin(\omega t). \tag{2.3}$$

However, if one were to assume that the base *acceleration* amplitude was independent of excitation frequency:

$$\ddot{y} = A\sin(\omega t) \tag{2.4}$$

then the amplitude of base displacement becomes $Y = A/\omega^2$ and equations (2.1) and (2.2) become:

$$p_{av} = \frac{A^2}{\omega}\frac{\zeta\omega_r^3 m}{(1-\omega_r^2)^2 + (2\zeta\omega_r)^2} \tag{2.5}$$

and

$$p_{av(res)} = \frac{A^2 m}{4\omega\zeta} \tag{2.6}$$

respectively such that power is now inversely proportional to excitation frequency. Consequently then, high frequency excitations are desirable for a scenario where base displacement amplitude is independent of excitation frequency while low frequency excitations are desirable for the scenario where base acceleration amplitude is independent of excitation frequency. With regards to harvesting from low frequencies it is stated in [10] that 'this is compounded by practical observations that acceleration levels associated with environmental vibrations tend to reduce with increasing frequency'. One can at least conclude that careful consideration should be given to the excitation spectra when considering energy harvester design. These issues are discussed extensively in Chapter 8 of this work.

All of the early literature on linear SDOF resonant energy harvesters agree on some key points:

1. Maximum power will be generated if the device is excited at resonance [13, 14, 15, 17]
2. Increasing the damping of the device (by increasing the electromechanical coupling) will extend the bandwidth over which it functions effectively [13, 10, 15]
3. The mass (of the magnet in the electromagnetic case) should be as large as possible within the available volume of the device [8, 13, 15, 17]
4. Maximum power output will be limited by the maximum allowable displacement (often referred to as 'rattle space') of the device [13, 14, 15, 17]

The first point is fairly intuitive but highlights one of the main issues with linear resonant energy harvester solutions: such devices will only perform well over a narrow bandwidth close to their natural frequency thus leaving them vulnerable to changes in excitation frequency. This is problematic as the majority of ambient vibration sources are relatively broadband or have time dependent dominant frequencies (a description of some different potential ambient energy sources can be found in [18]). A possible solution to this problem would be to use a large ensemble of resonant devices, each tuned to a different frequency [19] although the number of devices required to cover a small bandwidth of frequencies would likely be impractical. Additionally, PZT cantilever beam devices with multiple proof masses have been proposed [20] which are designed such that energy can be harvested simultaneously from several of the beam's resonant frequencies simultaneously[1]. Staying with cantilever beam devices, it has also been shown that the addition of a mass and spring to the beam can, when tuned properly, extend the useful bandwidth of

---

[1] This is an interesting problem as, when above the fundamental mode of vibration, the polarity of the induced strain will change at points along the length of the beam. Consequently, careful design is needed to avoid the charge developed by the PZT elements cancelling.

the device [21, 22].

As well as this, several devices have been proposed featuring tuning mechanisms [23, 24, 25, 26] which allow their natural frequency to be altered in response to changes in excitation frequency (more examples of such devices are reviewed in [27] and [28]). A problem with tuneable energy harvesters is that the apparatus needed to monitor the excitation frequency content and produce the appropriate changes in device natural frequency will inevitably require a power source of its own. An interesting solution to this problem was proposed in [26] in which the potential for placing an energy harvester inside a rotating car tyre was investigated (such that it can power a pressure sensor). In this work a weighted swing disk mechanism was proposed and shown to have a natural frequency proportional to the rotation frequency of the tyre thus allowing it too 'self tune' to changes in excitation condition.

This brings one to the second issue with linear resonant energy harvesters: from basic linear vibration theory it is known that by increasing the damping in a linear mass-spring-damper system one extends the bandwidth over which it oscillates at relatively large amplitudes [29]. Clearly, for an energy harvester this increase in damping will have to be realised by increasing the electromechanical coupling of the device and not though parasitic losses. However, this will reduce the maximum amplitude that can be achieved when the device is excited at resonance. Consequently, increasing the useful bandwidth of operation of the device by this method will reduce the its maximum possible power output.

The third and fourth points are concerned with the *size* limitations of energy harvesting devices. Given that one of the main motivations for the last 10 years of research into energy harvesting is that advances in MEMS technology have allowed the development of very small devices, these size limitations to power output are important. Again, this is an issue which is addressed in this thesis (Chapter 6).

As a result of the issues highlighted in this section, a large body of work has been, and still is being, devoted to investigating whether energy harvester performance can be improved by deliberately introducing dynamic nonlinearities into such devices - this forms the main focus of this thesis.

At this point it is worth noting that the majority of the works that are discussed in this chapter are concerned with energy harvester dynamics. With regards to electronics, it is often assumed that the device is simply delivering charge to a load resistor - a topic which is discussed extensively for the linear resonant case in [14] and [15]. While, in practical terms, it would likely be more useful for an energy harvesting device to deliver charge to an energy storage mechanism rather than directly to a load, such issues are considered beyond the scope of the current work.

2.5 Nonlinear energy harvesting

In general, nonlinear energy harvesters can be separated into two classes: monostable and bistable (in other words, devices with either one or two equilibrium points). The difference between the two types is discussed in detail in the following sections, beginning with the monostable class.

2.5.1 Monostable nonlinear energy harvesting

Sinusoidal Excitation

As stated in section 2.4, linear resonant energy harvesters only work effectively over a small bandwidth. Among the first to consider the possibility of resolving this issue via the deliberate introduction of nonlinearities into the device was Mann and Sims [30]. A schematic of the *Mann and Sims device* is shown in Figure 2.3.

Rather than being held in place by linear springs, the permanent magnet of the device proposed by Mann and Sims was held in suspension by two outer magnets which were orientated such that their poles were repelling that of the ‘centre magnet’. In their work it was shown that the resulting magnetic restoring force could be accurately modelled as a spring with a cubic nonlinearity. This gave the system similar properties to that of the monostable hardening spring Duffing oscillator (Figure 2.4) which has a governing equation of the form:

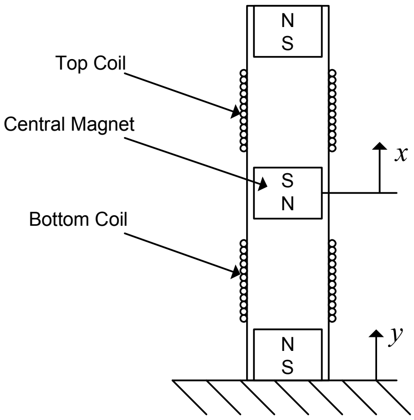

Figure 2.3: Schematic diagram of device proposed by Mann and Sims [30].

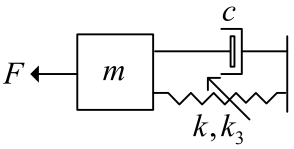

Figure 2.4: Schematic of forced Duffing oscillator.

$$m\ddot{x} + c\dot{x} + kx + k_3x^3 = F \tag{2.7}$$

where m is mass, c is viscous damping, F is force and k and k_3 represent linear and cubic stiffnesses respectively.

The Duffing oscillator or, more specifically, Duffing's equation has long been the focus of much attention from those with an interest in nonlinear dynamics. Much of this stems from the fact that, despite its simple appearance, the equation is difficult to solve (both in the context of forced and free vibration). Indeed, many nonlinear dynamics text books devote large sections to the approximation of Duffing's equation via a variety of methods (these are discussed in Chapter 4). For an extensive discussion of Duffing's equation references [31, 32, 33, 34] are recommended.

The nonlinearity present in the Duffing oscillator is known to produce several interesting phenomena including regions of multiple solutions and chaotic behavior [35]. Of particular interest to Mann and Sims [30] was the 'skewing' effect that the nonlinear spring term can have on the frequency response of the device. An example of this effect is shown in Figure 2.5 where one can see that the frequency response has become so skewed that a region of multiple solutions has been created - termed

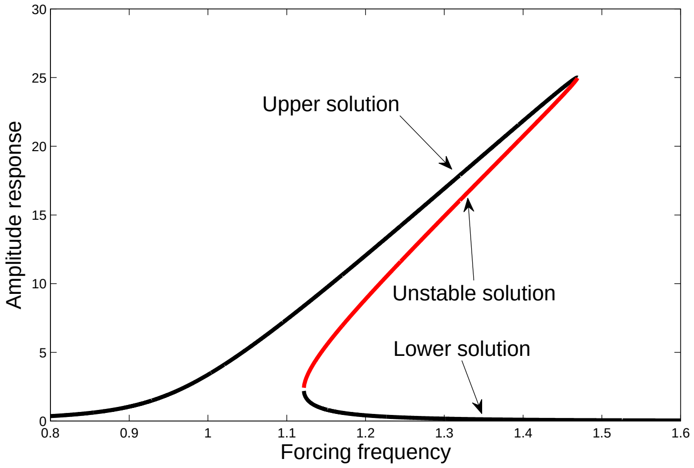

Figure 2.5: Example frequency response of forced Duffing oscillator demonstrating area of multiple solutions.

‘upper’ and ‘lower’ (sometimes referred to as high and low) energy solutions. In fact there is also a third solution between the upper and lower (marked in red on Figure 2.5) which is unstable such that, under steady state conditions, the Duffing oscillator will converge to either the upper or lower solutions only.

In [30] it was suggested that if one were to create an energy harvesting device which was able to stick to the upper solution then one would have a device which was capable of maintaining high amplitude oscillations over a larger bandwidth than in the linear resonant case thus making it less susceptible to changes in excitation frequency. As well as this it was proposed that the natural frequency of the device could be tuned by changing the distance between the magnets - an idea also suggested in [36]. Analysis of the Mann and Sims device forms a large part of the work in this thesis.

Other monostable devices with Duffing-type nonlinearities have also been analysed in [36, 37, 38, 39, 40]. In [39, 41] a device was proposed which consisted of a proof mass attached to a vibrating frame by four peizoelectric tethers. While this device was found to exhibit stiffening characteristics similar to the Duffing oscillator, the work did not focus on the possible benefits of the high energy periodic solutions associated with the nonlinearity. Instead, it was shown that utilising fixed-fixed thin piezoelectric beams allowed the device to function effectively away from resonance (when compared to the standard cantilever beam design). Another interesting device of this sort was proposed in [40]. The operating principle of this device was similar to that of the Mann and Sims device except that outer magnets were fixed to two prestressed piezoelectric beams (see Figure 2.6) such that, as the centre magnet approached the ends of the device, the beams could flex away thus reducing the chance of the magnet colliding with the beams.

In [38] a cantilever beam energy harvester was developed which also used magnetic restoration forces to create behavior similar to that of the monostable Duffing oscillator. In this work it was also concluded that the high energy solution created by the nonlinear restoring force could be used to extend the useful bandwidth of the device. It was also suggested that the subharmonics which can be created as a result of the nonlinearity could be manipulated in such a way as to allow the device to harvest energy from very low frequency vibrations. Potentially, this finding could prove very useful as many of the vibration sources considered for energy harvesting are low frequency - an issue which will be discussed in detail in Chapter 8. The second part of this paper focused on the response of the device to random excitations. In fact, the stochastic nature of ambient vibrations soon led to a large body of literature which focused on the random excitation of nonlinear devices - this will be discussed in the next section.

Thus far, the literature focused upon in this section has been concerned with the use of Duffing-type nonlinearities in monostable energy harvesters (as this is also one of the main focuses of the work undertaken by the author). However, it is worth noting that this is not the only type of nonlinearity which has been implemented in energy harvester designs. For example, in [42] a cantilever piezoelectric device was shown whose maximum displacement was constrained by a mechanical stopper. Using the hypothesis that connecting with the stopper increases the equivalent stiffness of the system (and therefore changes its natural frequency) a combination of analytical and experimental investigations were used to show that this stopper-type nonlinearity can improve the useful bandwidth of the device. Of course, the main limitation of such a device is that, by limiting its maximum possible displacement, the maximum possible achievable power output is reduced.

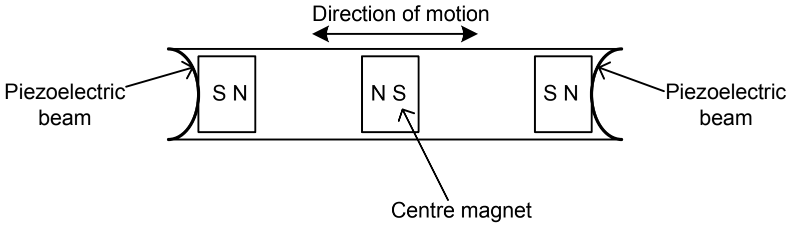

Figure 2.6: Schematic of piezoelectric based magnetic levitation device proposed in [40].

Random excitation

As mentioned previously, the stochastic nature of many ambient vibration sources led to several authors focusing on the response of nonlinear energy harvesters to random excitations. Barton et al [38] conducted an experimental investigation into the response of a monostable energy harvester with Duffing-type nonlinearities to narrow-bandwidth (≈ 2 Hz) random excitations. In this paper it was concluded that subjecting the device to random excitations seemed to 'average out' the difference between the high and low energy solutions present in the system thus eliminating the benefit of the nonlinear stiffness (at least with respect to power output, other benefits are discussed in Chapter 6 of this work).

Subsequently, in [43] the response of a similar device to a Gaussian white noise excitation was analysed using the Fokker-Planck-Kolmogorov (FPK) equation (the FPK equation is one of the main tools used in this work and will also be discussed in Chapter 6). Solving the FPK equation it was shown that, when under the afore mentioned excitation conditions, the nonlinear spring term has no effect on the relative velocity probability density function (PDF) of the system and therefore did not aid power output. The response of the device to coloured noise excitations was then analysed by approximating a solution for the corresponding FPK equation. It was concluded that, in the majority of cases, the nonlinear spring term is not beneficial to device performance. Again, this is discussed in more detail in Chapter 6.

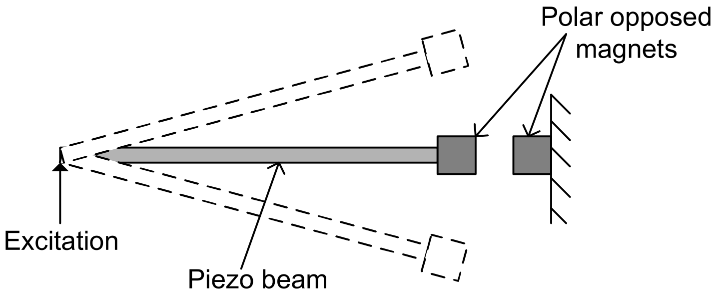

Figure 2.7: Example of bistable energy harvester where dotted lines represent equilibrium positions.

2.5.2 Bistable nonlinear energy harvesting

Sinusoidal excitation

The devices that were proposed in [30] and [38] were of the monostable variety. In [44] a device with two equilibrium points (hence bistable) was developed. An example of a bistable cantilevered beam energy harvester is shown in Figure 2.7. A permanent magnet has been placed at the beam tip such that its pole opposes that of an external magnet thus creating two potential equilibrium positions. The motivation behind such a device is that, if under the appropriate excitation conditions, the tip of the beam will behave chaotically as it jumps between the two energy wells - thus creating larger velocities than can be achieved in a monostable device.

In [45] work was undertaken with the specific aim of comparing the response of mono- and bi-stable devices to chirp excitations. In this work it was concluded that the bistable device was only effective if the inter-well chaotic response could be activated. Furthermore, it was found that the shape of the potential energy well required for such behavior to occur was very sensitive to the amplitude of excitation.

An alternative form of bistable device was proposed in [46] - a schematic of which is shown in Figure 2.8. Essentially this is the same device as was proposed by Mann and Sims [30] (Figure 2.3) except for the addition of outer magnets which are positioned such that the center magnet now had two possible equilibrium positions (see Figure 2.8 (a)). In [46] the response of the device to single frequency excitations of either varying frequency or amplitude was analysed using experimentally validated digital simulations. It was concluded that the power output of the device could be improved significantly if it was tuned such that the centre magnet was able to regularly jump between its two equilibrium positions.

Different conclusions were reached in [47] where a bistable cantilevered beam device was analysed. In this work it was shown that, as well as the chaotic solution, the system possessed high and low energy periodic solutions (just like the monostable Duffing oscillator discussed previously). It was concluded that greater power output could be achieved if one could always ensure that the device converged on the high energy solution rather than the chaotic solution (this is the same conclusion that was reached with regards to the monostable devices discussed previously). An interesting point raised in this paper was that, even if the activation of chaotic behavior allowed the device to function over a larger bandwidth, a periodic response is preferable with regards to the device power electronics.

It should be noted that the examples of bistable devices given in Figures 2.7 and 2.8 are only a sample of a variety of proposed bistable energy harvesters. For example, [48] details the optimisation of a device which makes use of the properties of composite laminates to achieve bistability.

Aside from the potential benefits that bistable devices can bring with respect to broadband performance, in [49] it was suggested that, when excited below its natural frequency, such a device could be used to convert low frequency mechanical vibrations into faster oscillator motions (frequency up-conversion) as a result of the subharmonics present in its response. This could prove to be useful as many of the excitation sources for energy harvesters are typically low frequency. A similar result was also found in [50] for a ‘buckling beam’ type energy harvester (Figure 2.9). Such a device consists of a beam which is subjected to a preload compressive force. Variation of this gives one the ability to determine whether the device will be bi- or mono-stable (depending on whether the preload is larger than the buckling load of the beam)[2]. In [50] it was shown that it was easier to exploit the subharmonics of a bistable device than those of the monostable variety and concluded that this would allow one to harvest energy from low frequency vibrations. The low frequency nature of ambient vibration sources and an evaluation of the application of the afore

---

[2] It has also been proposed that, by altering the axial load, such a device could be used a tuneable energy harvester [25]

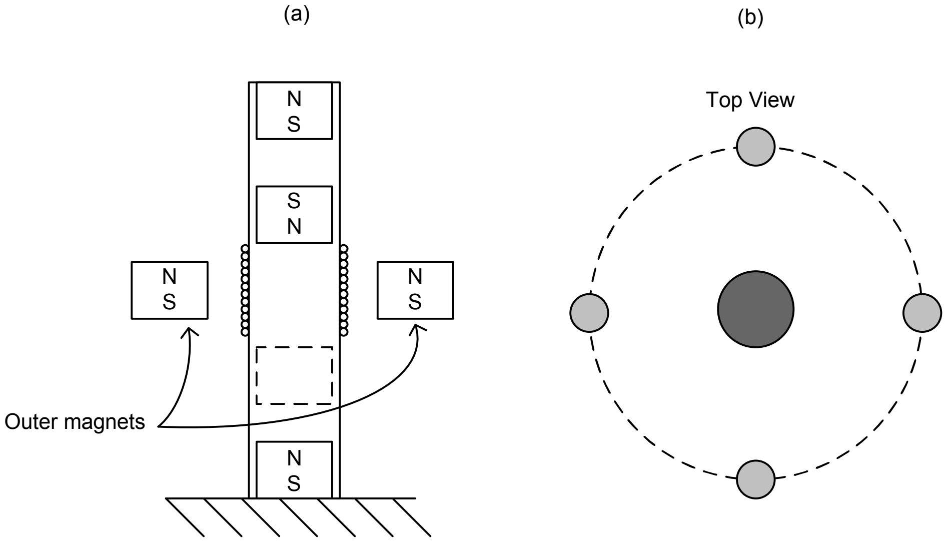

Figure 2.8: Schematic of device proposed in [46] showing (a) possible equilibrium position of the centre magnet and (b) positioning of outer magnets.

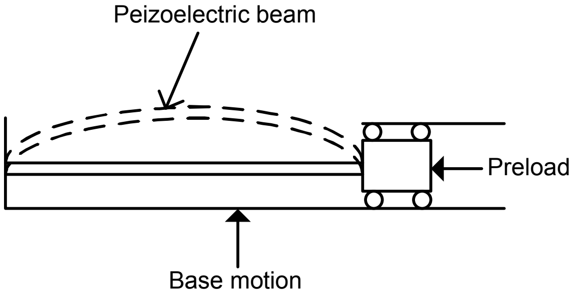

Figure 2.9: Buckling beam type energy harvester.

mentioned nonlinear energy harvesting techniques is discussed further in Chapter 8.

Random excitation

As in the monostable case, several works have focused on the response of bistable devices to random excitations. The response of a bistable device to Gaussian white noise excitations was investigated using digital simulations in [51]. In this work it was noted that the bistable device contained a high and a low energy solution and that the high energy solution was preferable to the activation of chaotic interwell dynamics (the same conclusion as was reached in [47] with regards to sinusoidal excitations). This work concluded by asking why a bistable device is necessary at all when it is known that monostable devices also posses similar high and low energy solutions.

In [52] the response of a bistable device to two different types of stochastic vibration was analysed using the FPK equation. For the case of a Gaussian white noise excitation a closed form solution to the FPK equation was found which showed that the shape of the potential energy function of the device (i.e. whether it is mono- or bi-stable) did not effect its power output. However, by approximating the solution of the FPK equation for the case of exponentially correlated noise it was shown that maximum power could be extracted from a bistable device if interwell dynamics were activated.

Ambient excitation

Moving away from computer generated random excitations, Vocca et al [53] used digital simulations to analyse the response of a bistable energy harvester to ambient vibration sources. More specifically, the response of the device shown in Figure 2.7 to three types of ambient excitation was analysed: that from the bonnet of a car, the floor of a train and the vibration of a microwave oven. In all three cases it is reported that, relative to the linear case, the activation of interwell dynamics led to an large increase in power. It was unclear however, whether the linear device was tuned to the dominant frequency of excitation or not.

2.6 Summary

In this chapter, an up to date review of energy harvesting literature relevant to this work has been given - specifically focusing on research into nonlinear devices. Clearly, there is some disagreement in the research community about whether any benefits can be gained via the deliberate introduction of Duffing-type nonlinearities into energy harvesting devices. Additionally, much of the work conducted is focused on either sinusoidal or Gaussian white noise excitations, rather than real ambient vibrations. In the following chapters the concept of nonlinear energy harvesting is evaluated for all three excitation types.

Chapter 3

Experimental Investigation

3.1 Introduction

In the previous chapter the magnetic levitation device proposed by Mann and Sims was discussed (see section 2.5.1 and Figure 2.3). This chapter describes the development and validation of a mathematical model of the device. Initially, the equation of the motion of the system is derived. The parameters of the model are then found using a differential evolution algorithm in conjunction with experimental test data. It is shown that, if one wants to model the device accurately, one needs to account for the effect of friction on its response (as well as viscous damping). With friction being a complicated nonlinear phenomenon for which many models are available, an investigation was undertaken to find the model most suitable to this particular problem. Subsequently, the electromechanical coupling of the device was modelled and, using experimental data, it is shown that the model accurately describes the transfer of energy from the mechanical to the electrical domain.

3.2 Mechanical System

The following sections are concerned with the modelling of the mechanical portion of the Mann and Sims device described in the previous chapter.

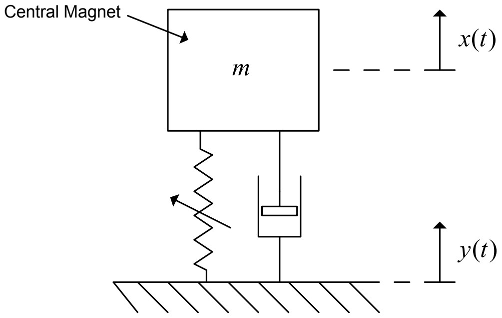

Figure 3.1: Schematic of energy harvester mechanical component.

3.2.1 Model Development

A lumped parameter model of the mechanical component of the Mann and Sims device [30] is shown in Figure 3.1 where the spring represents the nonlinear magnetic restoring force, the dashpot represents a viscous damper, and x and y represent the centre magnet and base displacements respectively. The equation of motion for this system is:

$$m\ddot{x} = -c(\dot{x} - \dot{y}) - k(x - y) - k_3(x - y)^3 - mg, \tag{3.1}$$

where m represents the mass of the centre magnet, k is the linear stiffness, k_3 the cubic stiffness, c the viscous damping and g gravity. This can then be rewritten in terms of relative displacement as:

$$m\ddot{z} + c\dot{z} + kz + k_3z^3 = -m\ddot{y} - mg, \tag{3.2}$$

where $z = x - y$.

To run a digital simulation, the solution to equation (3.2) was approximated using a 4th order Runge-Kutta numerical integration technique in Matlab's Simulink environment.

It should be noted here that the magnetic restoring forces have been modelled as a third order polynomial (following the work of [30]). In practice, dipole, distributed or point charge magnet models are available (see [54]). However, it will be shown in the following sections that a high fidelity model was obtained via the use of the cubic nonlinearity spring force.

3.2.2 Experiment

To begin with, the mechanical parameters of the system were identified using the apparatus shown in Figure 3.2. The device was attached to an electromagnetic shaker using an aluminium extension piece while the centre magnet was allowed to run along an aluminium rod via two sets of linear bearings. A linear variable differential transducer (LVDT) was used to measure the displacement of the shaker table. This signal was then fed through a proportional integral differential (PID) controller to allow control of the shaker table displacement. It should be noted at this stage that the device coils (and therefore the electromagnetic coupling) were not included in the experimental apparatus as the aim was to investigate the mechanical portion of the energy harvester only - the electrical portion is investigated in section 3.3 of this chapter.

Using the controller, the shaker was excited with a displacement signal that resulted in a white noise acceleration with a flat power spectral density between 4 and 20 Hz, as shown in Figure 3.3. As the device had a natural frequency of approximately 8 Hz, it was thought that the bandwidth of the acceleration spectrum was sufficiently large to capture the dynamics of the system. During each test, the displacement of the centre magnet was recorded using a laser triangulation sensor.

Using the shaker table time histories as an input to digital simulations of the energy harvester in question allowed comparison between the response of the model compared with the experiment centre magnet time histories. This forms an essential part of the system parameter identification - as discussed in the next section.

3.2.3 Parameter Identification

Having developed the model and successfully conducted a series of experiments the next task was to identify the parameters (m, c, k, k_3) which allowed the model to

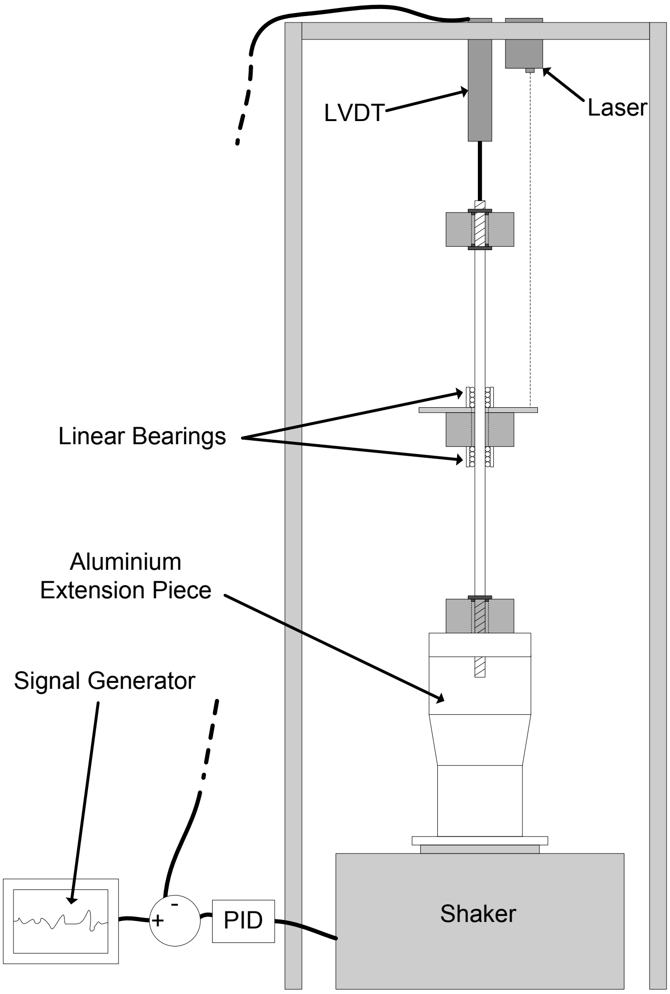

Figure 3.2: Schematic of experimental apparatus used to investigate the mechanical properties of the device.

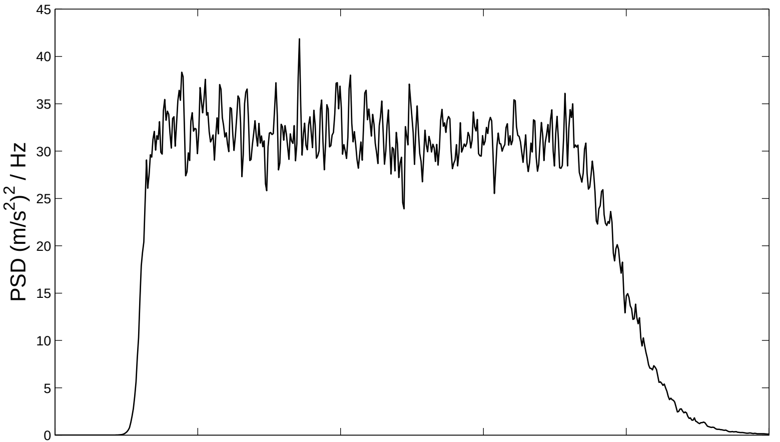

Figure 3.3: Example of base acceleration power spectral density.

accurately replicate the behavior of the experiment. The mass of the centre magnet was easily measured while the other terms, which were difficult to measure directly, were found using a differential evolution algorithm. However, before this algorithm is discussed, one must define the 'cost function'.

Cost Function

Having excited the model with the same base displacement signal as was used experimentally, a cost function was used to describe the level of similarity between the time response of the model compared with that of the experiment. This is shown in equation (3.3):

$$J(c,k,k_3) = \frac{100}{N\sigma_z^2}\sum_{i=1}^{N}(z_i - \hat{z}_i(c,k,k_3))^2 \tag{3.3}$$

where i represents the point in the time history vector, z_i and σ_z^2 represent the time history and variance of the experimentally obtained relative displacement, $\hat{z}_i$ represents the relative displacement according to the simulation and c, k and k_3 are the parameters that need to be identified. The cost function is chosen so that if the model simply produced the mean of the experimental result (denoted $\bar{z}$) then the function will return a value of 100:

$$J(c,k,k_3) = \frac{100}{N\sigma_z^2}\sum_{i=1}^{N}(z_i - \bar{z})^2 = 100 \tag{3.4}$$

It is stated in [55] that a cost function of less than 5 represents a reasonably good correlation, and that less than 1 can be considered excellent. The aim at this stage then, is to identify the model parameters which will minimise J (equation (3.3)).

Self-Adaptive Differential Evolution

A differential evolution (DE) algorithm was used to identify the device parameters. A brief description of the algorithm is given here.

A schematic diagram of a DE algorithm is shown in Figure 3.4. Initially, values of

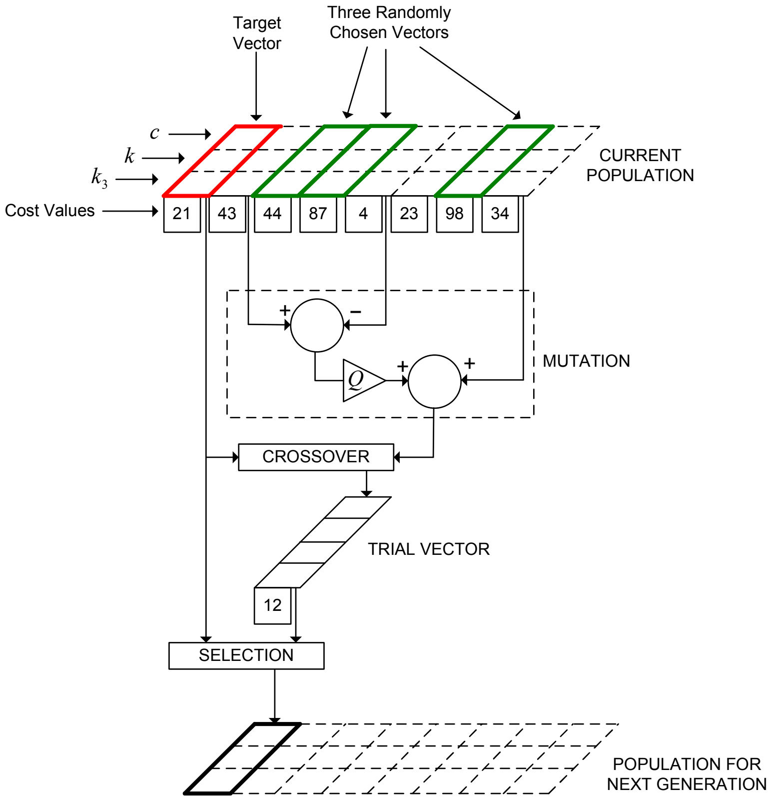

Figure 3.4: Schematic of a typical differential evolution algorithm where red represents the target vector and green represents 3 randomly chosen vectors.

c, k and k_3 are chosen from a uniform random distribution whose limits have been predefined, and are utilised in a simulation. The time history of the simulation is then compared with that of the experiment using the cost function (equation (3.3)). This process is repeated a set number of times until a population of parameters with corresponding cost functions is formed. This matrix of parameters is shown in Figure 3.4 as the *current population*.

Following this, the algorithm chooses the first set of parameter values in the current population and uses it as the *target vector* (this parameter vector is shown in red in Figure 3.4). It then takes two random parameter vectors from the population, subtracts one from the other, multiplies it by some constant (Q in this case) and finally adds it to a third randomly chosen vector thus creating what is termed the *mutated vector*.

The *trial vector* is the ‘child’ of the target vector and the mutated vector. It is formed using a crossover process, whereby a predefined hyperparameter (C_r) determines whether the trial vector takes a parameter value from either the target vector or the mutated vector. The cost functions of the trial vector and the target vector are then compared so that only the set of parameters with the lowest cost function will survive to the next generation. The algorithm then chooses the next set of parameters in the current population as the target vector and repeats the process until a population of next generation parameter values has been created. This is repeated for numerous generations until a set of parameters are found which result in a sufficiently low cost function. While computationally expensive, the advantage of using this population based approach to the parameter estimation problem is that one should converge on the global minimum cost value (rather than a local minimum).

In this work a variation of DE was used: self-adaptive differential evolution (SADE). This algorithm performs a similar procedure except that it also 'learns' which values of Q and C_r are most likely to result in a trial vector that will survive to the next generation and, as a result, is capable of faster convergence relative to a standard DE algorithm. In the initial stage of this adaptive algorithm the hyperparameters Q and C_r are sampled from normal distributions:

$$Q \sim \mathcal{N}(\bar{Q}, \sigma_Q) \tag{3.5}$$

$$C_r \sim \mathcal{N}(\bar{C}_r, \sigma_{C_r}) \tag{3.6}$$

whose moments ($\bar{Q}$, σ_Q, $\bar{C}_r$ and σ_{C_r}) have been defined by the user. In the runs that follow the values of the hyperparameters are re-sampled after a set number of generations. During this process the values of Q and C_r which lead the survival of a target vector to the next generation are recorded such that, after a time, the mean of these 'successful' hyperparameters can be calculated and adopted as the next values of $\bar{Q}$ and $\bar{C}_r$. This allows the algorithm to adapt in such a way that the probability of a target vector surviving to the next generation is higher relative to a non-adaptive differential evolutionary scheme. For more discussion of the SADE algorithm the reader is directed towards references [55] and [56].

In each of the following analyses a population of 30 parameter vectors was allowed to evolve for 200 generations. The algorithm was judged to have converged if the mean cost across the final generation was close to the cost of the best parameter vector.

3.2.4 Friction Modelling

After initial testing it became clear that the response of the experimental device was very sensitive to the effects of friction. This was despite the use of linear bearings to reduce the friction between the centre magnet and aluminium rod (as shown in Figure 3.2). Consequently, the equation of motion for the device was rewritten as:

$$m\ddot{z} + c\dot{z} + kz + k_3 z^3 + F = -mg - m\ddot{y} \tag{3.7}$$

where F was chosen to represent the force on the centre magnet due to friction. As mentioned previously, there are many different friction models available. Of these, three were investigated in this work: Coulomb, hyperbolic tangent and LuGre [57]. The properties of each model are briefly discussed in the following sections.

Coulomb

Initially, the Coulomb damping model was used to replicate friction present in the system. Among the earliest and best known friction models, the restoring force due to friction is given by:

$$F = F_c \operatorname{sgn}(\dot{z}) \tag{3.8}$$

where F_c is a parameter to be identified and sgn represents the signum function:

$$\operatorname{sgn}(\dot{z}) = \begin{cases} 1, & \dot{z} > 0 \\ 0, & \dot{z} = 0 \\ -1, & \dot{z} < 0 \end{cases} \tag{3.9}$$

With only one parameter, the obvious advantage of the Coulomb damping model is its simplicity although it is unable to model some of the phenomena which are typ-

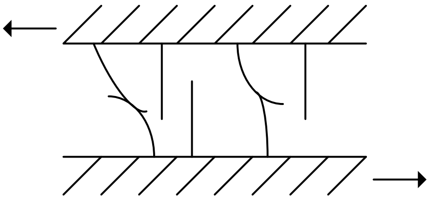

Figure 3.5: In the LuGre model, friction is represented by the interaction of randomly distributed elastic bristles.

ically associated with friction-affected systems (this is discussed more with regards to the LuGre model). Additionally, the discontinuity of the signum function at zero can make analytical analysis difficult.

Hyperbolic tangent

The second model that was investigated was the hyperbolic tangent friction model:

$$F = F_c \tanh(\beta \dot{z}). \tag{3.10}$$

This has the property that, while requiring an extra parameter compared to the Coulomb damping model (β in this case), the model is able to accurately represent the Coulomb damping model without being discontinuous. Also, as β approaches infinity, it reduces to the signum function:

$$\lim_{\beta \to \infty} \tanh(\beta \dot{z}) = \operatorname{sgn}(\dot{z}). \tag{3.11}$$

LuGre

The LuGre model (proposed in [57]) is based on the hypothesis that the interaction between two surfaces can be modelled as rigid bodies which make contact via a set of randomly distributed 'bristles' (see Figure 3.5).

The average displacement of the bristles is modelled using:

$$\dot{\Theta} = \dot{z} - \frac{|\dot{z}|}{g(\dot{z})}\Theta \tag{3.12}$$

where Θ is the average bristle displacement and $g(\dot{z})$ is a function which is chosen depending on the material properties of the system. Equation (3.12) is in state-space form (in other words, $\dot{\Theta}$ is expressed as a function of Θ) thus allowing it to be evaluated using the same numerical integration techniques used in the energy harvester simulations (see section 3.2.1). The friction force exerted on the mass is given by:

$$F = \sigma_0 \Theta + \sigma_1 \dot{\Theta}. \tag{3.13}$$

where σ_0 and σ_1 are parameters to be found. One of the advantages of the LuGre model is its ability to account for the Stribeck effect (the phenomenon that, at low velocities, friction force decreases with increasing velocity). To account for the Stribeck effect the function $g(\dot{z})$ will be defined using:

$$\sigma_0 g(\dot{z}) = F_c + (F_s - F_c) e^{-(\dot{z}/\dot{z}_s)^2} \tag{3.14}$$

where F_s represents stiction force, F_c is the Coulomb friction level and $\dot{z}_s$ is the Stribeck velocity. While this model requires the identification of five parameters (σ_0, σ_1, F_c, F_s and $\dot{z}_s$) it accounts for the majority of phenomenon associated with friction (friction lag, spring-like behavior in stiction and varying break-away force). This is discussed more in [57].

3.2.5 Performance of friction models

Using the SADE algorithm, the parameters which led to the best match between the response of the model and experiment were identified.

Nine different experiments were conducted - each using a different intensity of white noise. The root mean square (RMS) value of each excitation signal is shown in Table 3.1. Initially, test number 3 was used as the training data for SADE (shown as ‘training data 1’ in Table 3.1). The parameter values identified are shown in Table 3.2 (column ‘training data 1’). The identified parameter values were then used to compare the model response with that of the experiment for all the other test conditions. Again, the ability of the model to replicate the response of the experiment was quantified using the cost function (equation (3.3)).

	Test number	RMS($\ddot{y}$) (m/s^2)
	1	1.07
	2	1.21
Training data 1:	3	1.34
	4	1.54
	5	1.67
	6	1.84
	7	1.96
Training data 2:	8	2.12
	9	2.22

Table 3.1: RMS base acceleration for each excitation condition.

Figure 3.6 (a) compares the performance of each friction model using the parameters identified when test 3 was used as training data. It is immediately obvious that the inclusion of a friction model has greatly improved the ability of the simulations to replicate the response of the experiment. It can also be seen that very similar cost values are realised for the Coulomb and hyperbolic tangent models over the entire range of tests. Recalling the governing equations of both friction models:

$$F = F_c \operatorname{sgn}(\dot{z}) \tag{3.15}$$

$$F = F_c \tanh(\beta \dot{z}) \tag{3.16}$$

after consulting the identified parameters in Table 3.2 (training data 1), it is clear that these two models will behave in a very similar manner. This is because the same value of F_c was identified in each case and, as a result of a very high value for β, the hyperbolic tangent model is forming a very close approximation to the signum function used in the Coulomb damping model. Perhaps one of the most interesting results from this investigation is that the Coulomb and hyperbolic tangent models have consistently outperformed the LuGre model for all of the test conditions except for test 8. Coincidentally, this also happens to be the test case where friction seemed to have the most significant effect on device response (as this is where the simulations without a friction model performed the worst). The test that was used as training data (test 3) also happened to be the test where friction appeared to be the least significant. This raises the possibility that the dynamics of the system were

Model	Parameter	Value (training data 1)	Value (training data 2)	Units
No Friction	c	0.116	0.079	Ns/m
	k	54.8	54.2	N/m
	k_3	112620	119210	N/m^3
Coulomb	c	0.049	0.047	Ns/m
	k	57.4	56.1	N/m
	k_3	70742	91894	N/m^3
	F_c	0.0058	0.0065	N
Hyperbolic tangent	c	0.049	0.047	Ns/m
	k	57.5	56.1	N/m
	k_3	68956	91798	N/m^3
	F_c	0.0058	0.0065	N
	β	4.8×10^8	8.3×10^8	s/m
LuGre	c	0.055	0.051	Ns/m
	k	59.7	58.1	N/m
	k_3	64926	79788	N/m ^{3}
	σ_0	1.98	4.9	N/m
	σ_1	0.18	0.19	Ns/m
	F_c	0.0008	0.0007	N
	F_s	0.008	0.0006	N
	$\dot{z}_s$	0.007	0.0006	m/s

Table 3.2: Identified Parameters for each friction model using test 3 and test 8 as training data.

not sufficiently friction-affected to allow proper identification of the parameters in the LuGre model. For this reason, the identification process was repeated using the most friction affected test (test 8) as the training data (shown as ‘training data 2’ in Table 3.1). The resulting parameters are shown in Table 3.2 (training data 2).

Once again, the hyperbolic tangent model formed a close approximation to the Coulomb damping model. For both models, a higher value of F_c was identified when test 8 was used as training data - this confirms the hypothesis that friction affected this test more than test 3. That being said, the use of test 8 has not led to an increase in viscous damping for the model with no friction. This indicates that the friction effects present in the system cannot be accounted for simply by increasing the viscous damping parameter.

Figure 3.6 (b) compares the performance of each friction model using the parameters identified with test 8 as training data. Once again, there is a significant difference between the performance of the friction models relative to the model with no friction effects. While the use of a different test as the training data has improved the performance of the viscous model in some cases it has also dramatically impaired it in others. This confirms that such a model is poorly suited to model the dynamics of the device over the full range of operating conditions used experimentally.

3.2.6 Validation

The Coulomb damping model was chosen to model friction in the device as a consequence of its simplicity and good performance. Using the parameter values identified in the previous section (training data 2) the quality of the match between simulation and experimental results was analysed graphically. Figures 3.7, 3.8 and 3.9 show the displacement time history, histogram, frequency content and power output (given by $p = c\dot{z}^2$) of experiment and simulation for conditions 2, 5 and 8 respectively. There is an excellent match between simulation and experiment. It should be noted that, at this point, the term ‘power output’ is referring to the maximum power available if all of the viscous damping in the device was due to the electromechanical coupling.

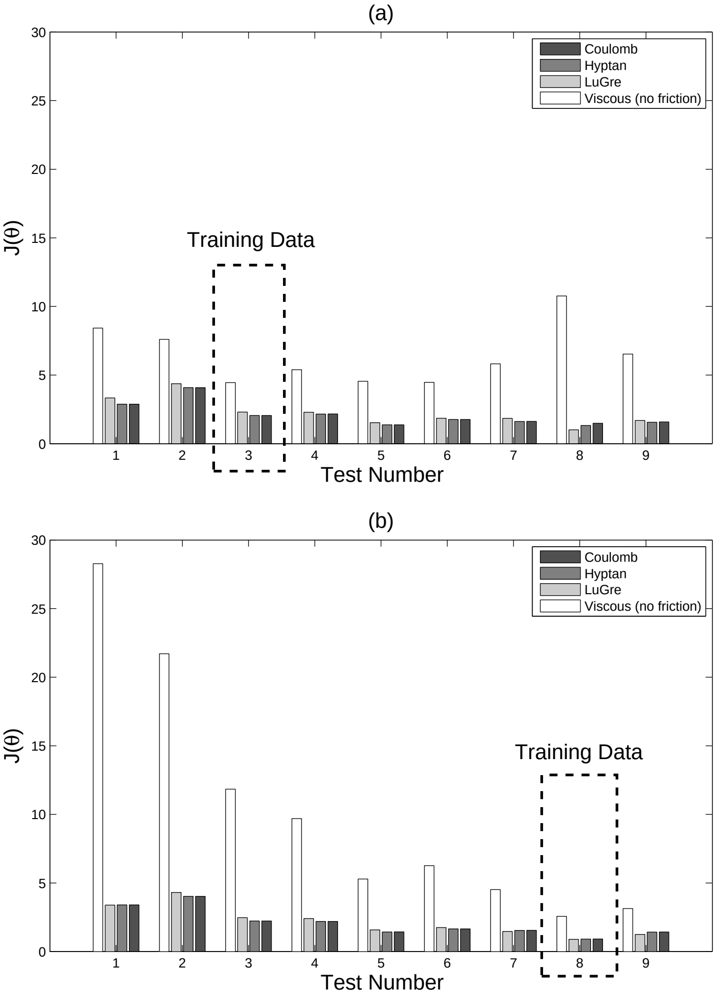

Figure 3.6: Cost between experiment and simulation time histories for different tests having used (a) test 3 and (b) test 8 as training data.

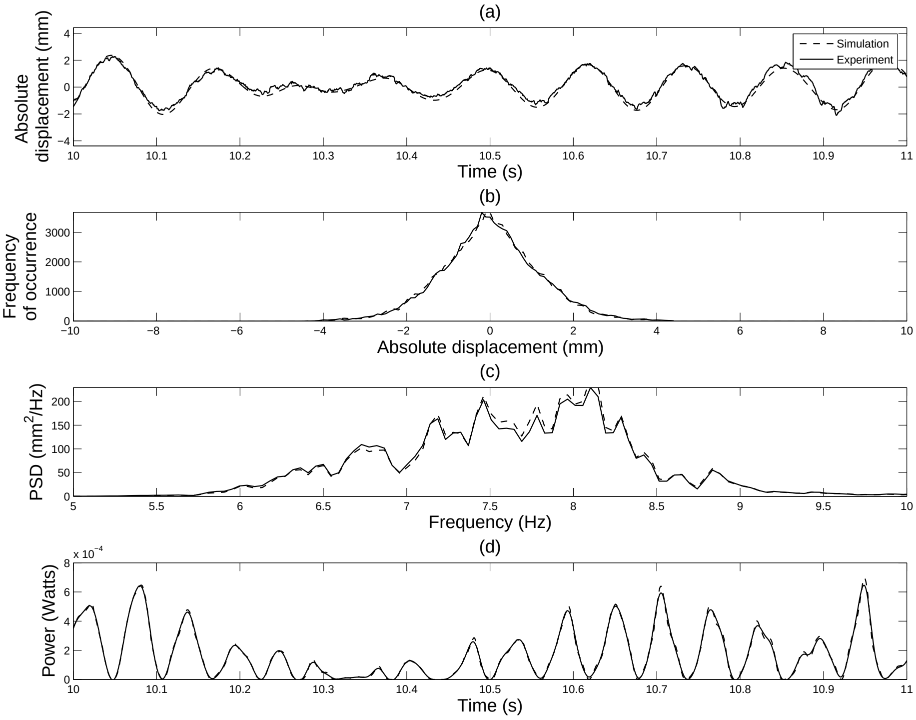

Figure 3.7: Comparison of simulation and experimental results for test number 2. Shown is centre magnet displacement (a) time history portion, (b) histogram,(c) frequency content and (d) device power output. Dashed lines and solid lines represent the simulation and experiment respectively.

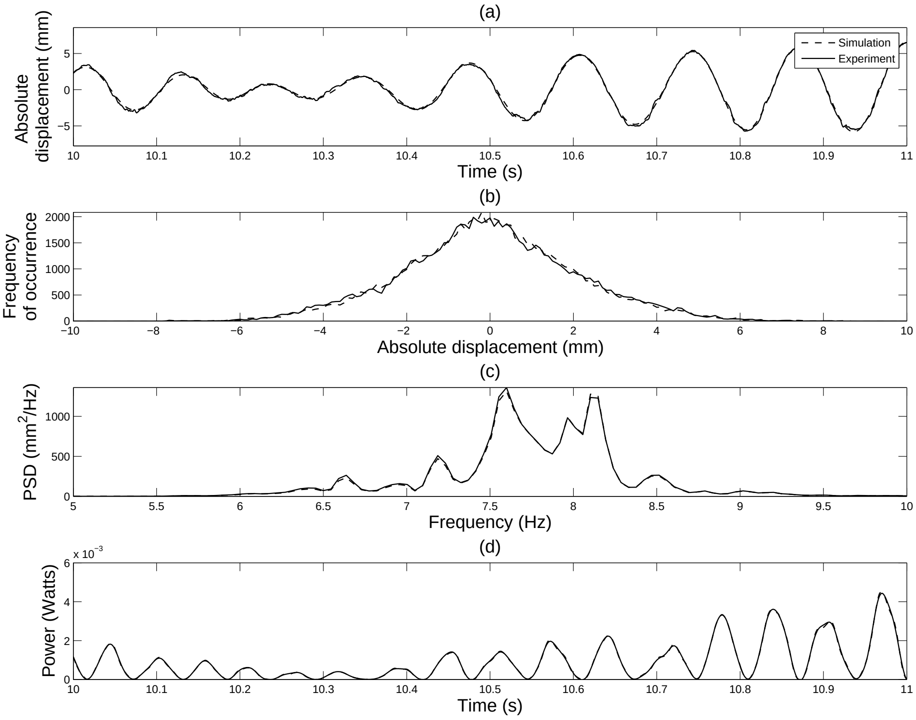

Figure 3.8: Comparison of simulation and experimental results for test number 5. Shown is centre magnet displacement (a) time history portion, (b) histogram,(c) frequency content and (d) device power output. Dashed lines and solid lines represent the simulation and experiment respectively.

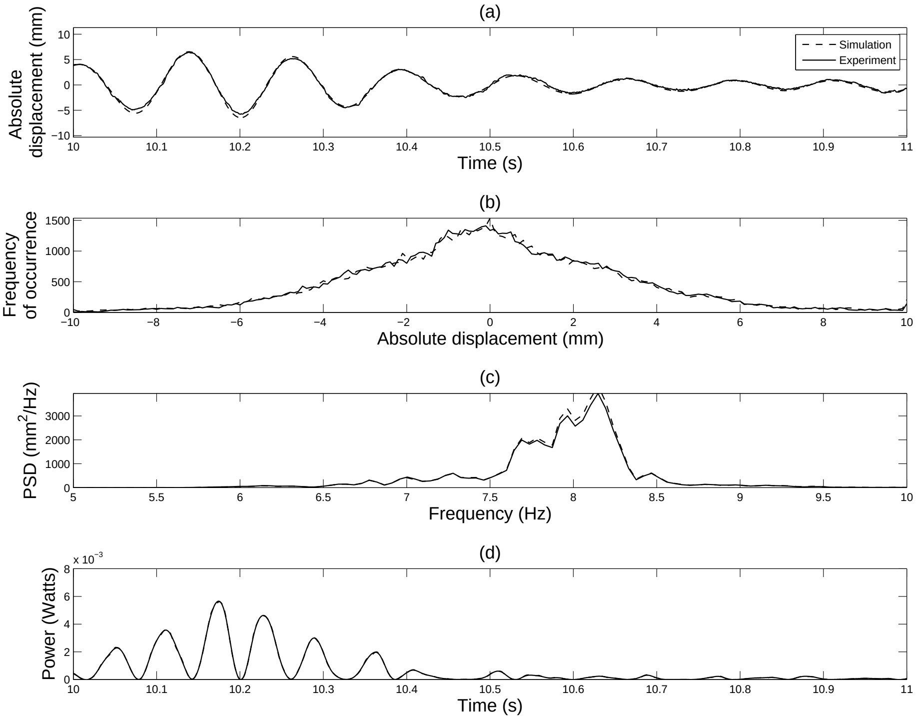

Figure 3.9: Comparison of simulation and experimental results for test number 8. Shown is centre magnet displacement (a) time history portion, (b) histogram,(c) frequency content and (d) device power output. Dashed lines and solid lines represent the simulation and experiment respectively.

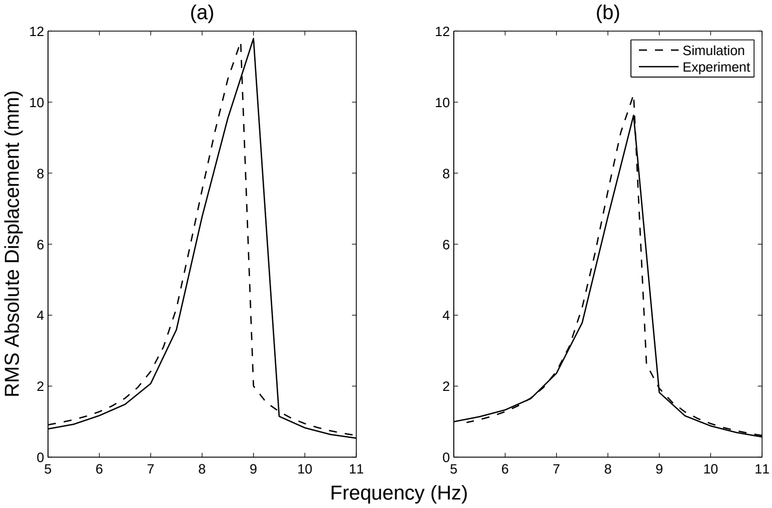

Figure 3.10: Comparison of (a) stepped up and (b) stepped down frequency response with an input amplitude of 0.8mm. Dashed lines and solid lines represent the simulation and experiment respectively.

To ensure that the estimated parameter values were sensible, the stepped up and stepped down frequency response of the simulation was compared with that of the experiment. This was obtained using a stepped sine technique, where the root-mean-square (RMS) of the response amplitude was measured at each frequency. Figure 3.10 shows that there is good match between the frequency response of the real device and that of the model. It also shows that the model is able to demonstrate the jump phenomenon that is associated with the hardening spring Duffing oscillator (as described in Chapter 2).

3.3 Electrical System

In this section the electrical component of the device is considered and coupled to the mechanical portion of the model.

3.3.1 Model Development

Using an electromagnetic coupling to transfer kinetic energy into the electrical domain (Faraday's law) and connecting the device to a load resistance realises the circuit diagram shown in Figure 3.11 where L represents the inductance created by

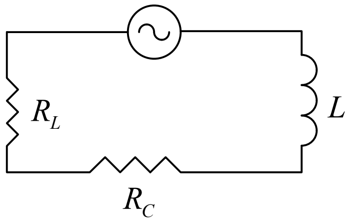

Figure 3.11: Energy harvester circuit diagram.

the coil and R_L and R_C represent the load and coil resistances respectively.

Taking account of the electrical portion of the device, one now has to introduce an additional term into the equation of motion:

$$m\ddot{z} + c\dot{z} + kz + k_3z^3 + F_c\,\mathrm{sgn}(\dot{z}) + F_e = -m\ddot{y} - mg, \tag{3.17}$$

where F_e represents the force on the centre magnet as a result of the electromagnetic coupling. From Faraday's law, one can write:

$$E_{ind} = -\frac{d\Phi}{dt} = -\frac{d\Phi}{dz}\dot{z}, \tag{3.18}$$

where E_{ind} is the induced electromotive force and Φ represents magnetic flux. Equating the instantaneous power between the mechanical and electrical domains gives:

$$F_e\dot{z} = iE_{ind}, \tag{3.19}$$

where i is the current flowing within the coil. Combining equations (3.18) and (3.19) one finds that:

$$F_e = -i\frac{d\Phi}{dz}. \tag{3.20}$$

Applying Kirchoff's voltage law to the circuit yields:

$$i(R_L + R_C) + L\frac{di}{dt} = -\frac{d\Phi}{dz}\dot{z}. \tag{3.21}$$

For low frequency applications it is assumed that L is negligible so that:

$$F_e = \alpha^2 \frac{1}{R_L + R_C} \dot{z}, \tag{3.22}$$

where $\alpha = \frac{d\Phi}{dz}$. Assuming α is constant over the region of interest, the governing equation of the device can be written as:

$$m\ddot{z} + c\dot{z} + kz + k_3 z^3 + F_c \operatorname{sgn}(\dot{z}) + \alpha^2 \frac{1}{R_L + R_C} \dot{z} = -m\ddot{y} - mg. \tag{3.23}$$

Finally then, dividing by mass, the governing equation becomes:

$$\ddot{z} + (2\omega_n \zeta + \gamma/m)\, \dot{z} + \frac{F_c}{m} \operatorname{sgn}(\dot{z}) + \omega_n^2 z + \beta z^3 = -\ddot{y} - g, \tag{3.24}$$

where ζ is the damping ratio, ω_n is the natural frequency, $\beta = k_3/m$ and $\gamma = \frac{\alpha^2}{(R_L + R_C)}$. One can see that, using this model, the effect of the electromagnetic coupling is modelled as an extra viscous damping term, γ.

3.3.2 Power through Load Resistor

Electrical power can be calculated from the instantaneous power given in equation (3.19):

$$iE_{ind} = F_e \dot{z} = \frac{\alpha^2 \dot{z}^2}{R_L + R_C} = \frac{R_L \alpha^2 z_2^2}{(R_L + R_C)^2} + \frac{R_C \alpha^2 z_2^2}{(R_L + R_C)^2}, \tag{3.25}$$

such that the power delivered to the load is given by:

$$p_{load} = \frac{R_L \alpha^2 \dot{z}^2}{(R_L + R_C)^2} = \frac{R_L \dot{z}^2 \gamma}{(R_L + R_C)}. \tag{3.26}$$

3.3.3 Experiment

With the mechanical parameters of the device already identified, 83 turns of 0.5 mm diameter copper coil was wrapped around a PTFE tube which was subsequently attached to the shaker base - as shown in Figure 3.12. The output from the coil was then fed through a load resistor. The resistance of the coil was found to be 0.48 Ohms and the inductance was found to be negligible (the effects of inductance will be discussed more in section 3.3.6).

3.3.4 Parameter Identification

The relationship between the magnetic flux and the relative displacement of the centre magnet for a single turn of coil was found using the finite element package FEMM. Following a presumption made in the previous section, a linear approximation of the flux-displacement relationship was made. Figure 3.13 shows that the approximation was chosen under the assumption that only relatively small centre magnet displacements would take place. From the finite element simulations it was found that $\alpha_1 = 0.0024$ Wb/m (where α_1 represents the flux displacement relationship for one turn of coil). Multiplying by the number of turns on the device it was found that $\alpha = 0.1992$ Wb/m.

3.3.5 Validation

The voltage across the load resistor of the device was compared with that of the model for different intensities of white noise base excitation. Again, there was an excellent match between model and simulation. Figure 3.14 shows a comparison between the time history and histogram of the voltage output from simulation and experiment with a load resistance of 3 Ohms. It can be seen that the voltage output of the model has matched the experiment well for all conditions, thus validating the assumption that the inductance can be ignored and that the flux displacement relationship can be approximated as linear. Upon consulting Figure 3.14 (b) it is interesting to note that the voltage histograms have a definite ‘spike’ in the centre. This is a result of friction preventing the centre magnet of the device from moving relative to the coils thus preventing any voltage generation. This was confirmed in subsequent simulation runs where it was found this spike disappeared and the histogram appeared smoother if the Coulomb damping nonlinearity was removed.

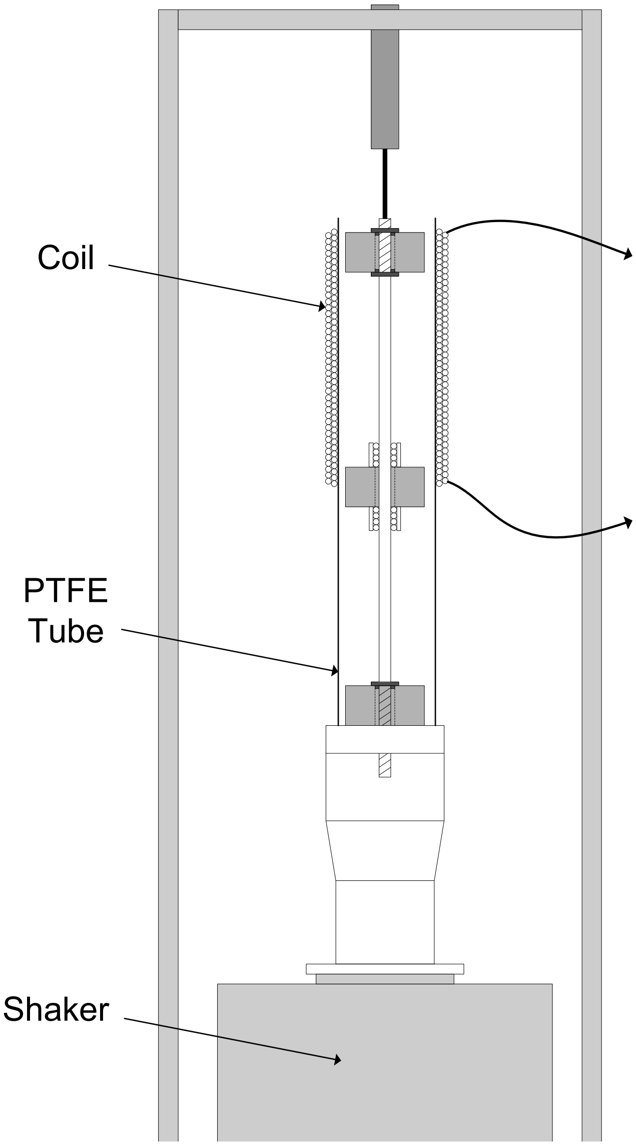

Figure 3.12: Schematic of experimental apparatus used to identify the electrical parameters of the device.

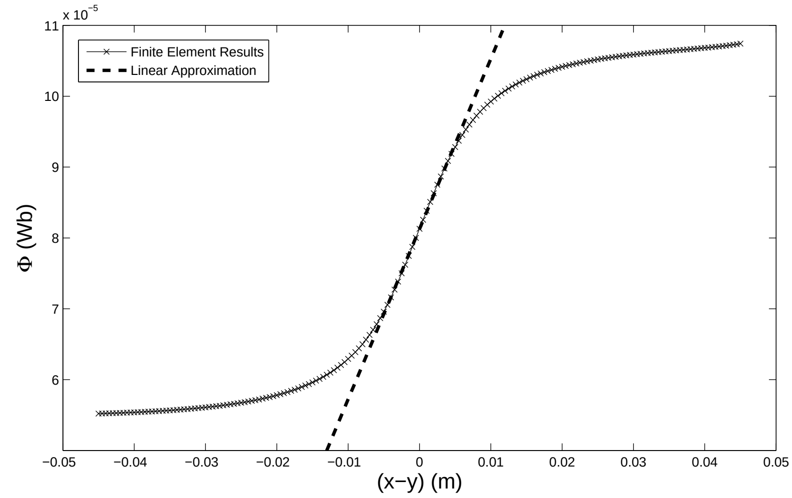

Figure 3.13: Finite Element simulation of flux displacement relationship. Dashed and solid lines represent simulation results and the linear approximation respectively.

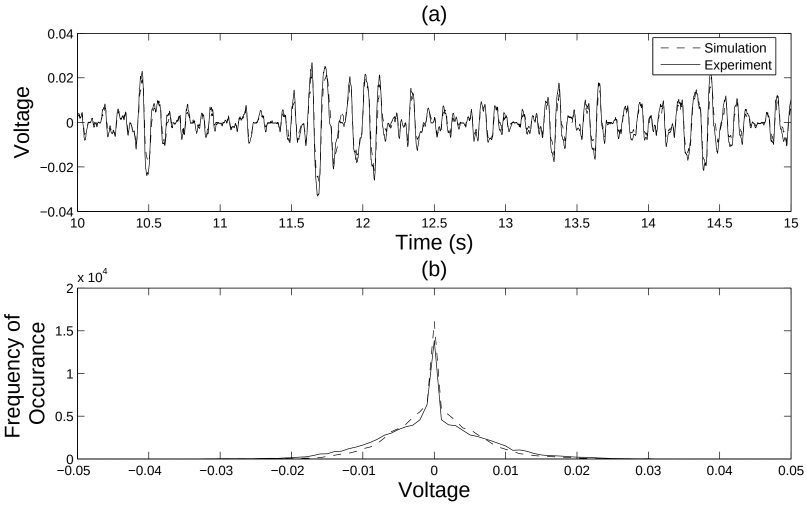

Figure 3.14: Comparison of voltage (a) time history and (b) histogram for condition 8. Dashed and solid lines represent the simulation and experimental results respectively.

3.3.6 Inductance

In the development of the electrical portion of the model it was assumed that the effects of inductance were negligible. As it is well known that a series combination of resistor and inductor acts as a low-pass filter then one would expect the importance of inductance to increase as the frequency of excitation increases. Typically, for low frequency signal filtering applications, inductances of several hundred henries are required - this is usually obtained by winding hundreds of turns of coil around a ferromagnetic material [58]. When measured, the inductance of the coil used in this work was found to be 4×10^{-8} henries - a value so small that one can safely assume that its effect can be considered negligible, especially when the majority of energy sources being considered for use with energy harvesters are of a relatively low frequency (bridge motion for example). However, although negligible in this case, the author recognises that it may not be possible to apply this assumption universally to all electromagnetic energy harvesters. Recently, an analytical analysis in [59] showed that when the electrical time constant of an energy harvesting device is close to its mechanical time constant (a consequence of large inductance values), Duffing-type nonlinearities can have a detrimental effect on its performance.

3.4 Summary

The purpose of the work in this chapter was to develop a test rig such that, by comparing with experimental data, a reliable and extensively validated mathematical model of the Mann and Sims energy device could be developed. With regards to device dynamics the first important contribution from this investigation was the discovery that one must include friction effects to accurately model the system dynamics. This is an important finding as the majority of works on SDOF energy harvesters use viscous damping only to model mechanical losses. After an extensive investigation using several different friction models it was found that the relatively simple Coulomb damping model could be used to accurately model friction in the device. Consequently, the effects of Coulomb damping on device response forms a large portion of the work in the following chapters.

With the mechanical part of the model validated, attention was then focused on the modelling of the electrical portion of the energy harvester. A model was created which could accurately replicate the voltage output of the experimental device and, by doing so, validated several assumptions which were made in its development (negligible inductance and linear flux displacement relationship).

Chapter 4

HARMONIC EXCITATIONS

4.1 Introduction

In the previous chapter an experimentally validated model of a monostable energy harvesting device with Duffing-type and Coulomb damping nonlinearities was developed. In this chapter the response of the device to sinusoidal excitations is approximated analytically using the method of harmonic balance. While it was stated in the introduction to this thesis that many ambient vibration sources need to be treated as being stochastic (chapters 5, 6 and 7 of this work are concerned with randomly excited energy harvesters for this reason) it is worth noting that this is not true of *all* ambient excitations. Indeed, there are also many vibration sources whose forms can be closely approximated by sine waves (the resulting vibration of an unbalanced rotating machine for example). Consequently, the purpose of the work in this chapter is to gain more insight into the behavior of the system to sinusoidal excitations - specifically the effect that friction on device performance.

4.2 Approximation methods

Recalling the equation of motion of the magnetic levitation device described in the previous chapter and, having neglected DC components (as the gravity term does not affect power output), one is left with the following nonlinear ordinary differential equation:

$$m\ddot{z} + c\dot{z} + F_d\,\mathrm{sgn}(\dot{z}) + kz + k_3z^3 = -m\ddot{y}. \tag{4.1}$$

As was touched on briefly in Chapter 2, even if one were to ignore the Coulomb damping term, the presence of the nonlinear spring term makes this equation difficult to solve. Consequently, different methods have been developed to approximate the solutions to equations of this type (perturbation methods, the method of averaging and the method of harmonic balance for example). With perturbation methods being one of the most commonly used, the aim of the following sections is to give a brief overview of this method alongside an explanation as to why the author elected to use the method of harmonic balance in this scenario.

4.2.1 Perturbation Method

To demonstrate perturbation methods a somewhat simpler differential equation with nonlinear spring term under a sinusoidal excitation will be considered:

$$\ddot{z} + \epsilon c\dot{z} + z + \epsilon z^3 = Y\sin(\omega t + \phi). \tag{4.2}$$

where, the parameter ϵ has been introduced as a book keeping parameter. The key to the perturbation method is the fact that, if ϵ is small, the solution to equation (4.2) can be closely approximated by:

$$z = z_0 + \epsilon z_1 + \epsilon^2 z_2 + \epsilon^3 z_3 + ... \tag{4.3}$$

For the sake of simplicity, only terms up to order ϵ will be considered here such that the approximation is written:

$$z = z_0 + \epsilon z_1 + O(\epsilon^2). \tag{4.4}$$

Substituting this into equation (4.2) one can write:

$$\ddot{z}_0 + \epsilon\ddot{z}_1 + \epsilon c\dot{z}_0 + z_0 + \epsilon z_1 = Y\sin(\omega t + \phi) - \epsilon z_0^3. \tag{4.5}$$

Equating the coefficients of ϵ^0 and ϵ^1 one can then construct two differential equations:

$$\ddot{z}_0 + z_0 = Y \sin(\omega t + \phi) \tag{4.6}$$

$$\ddot{z}_1 + z_1 = -c\dot{z}_0 - z_0^3 \tag{4.7}$$

the idea being that, having solved equation (4.6), one can substitute the obtained expression for z_0 into equation (4.7) to find z_1 and so on (depending on the order of ϵ one is approximating to).

During this procedure it is often the case that the solutions of some of these differential equations contain secular terms (terms which tend to infinity with time). Consequently, with the aim of removing these terms, one can introduce the variable Z which is a function of a slow time variable $\tau = \epsilon t$ as well as the original time scale t:

$$z(t) = Z(t, \tau). \tag{4.8}$$

The original nonlinear differential equation can then be written in terms of Z using the relations:

$$\frac{dz}{dt} = \frac{\partial Z}{\partial t} + \epsilon \frac{\partial Z}{\partial \tau} + ... \tag{4.9}$$

and

$$\frac{d^2 z}{dt^2} = \frac{\partial^2 Z}{\partial t^2} + 2\epsilon \frac{\partial^2 Z}{\partial t \partial \tau} + ... \tag{4.10}$$

The addition of the slow time variable then allows one to remove the secular terms when seeking an approximate solution of the form:

$$Z = Z_0 + \epsilon Z_1 + \epsilon^2 Z_2 + ... \tag{4.11}$$

This method of approximating the solutions to nonlinear differential equations is commonly referred to as the method of multiple scales. While perturbation methods are very powerful, solutions using these methods are often fairly complex (for a detailed description see [31, 32, 33]). An alternative and, in the author's opinion, simpler method for the problem at hand is that of harmonic balance.

4.2.2 Harmonic balance

Again, to demonstrate this method a simple nonlinear equation will be used as an example:

$$\ddot{z} + c\dot{z} + z + z^3 = Y\sin(\omega t + \phi). \tag{4.12}$$

Using one's prior knowledge of the system it is assumed that the system response will be of the form:

$$z = Z\sin(\omega t) \tag{4.13}$$

such that the equation of motion becomes:

$$-\omega^2 Z\sin(\omega t) + \omega Zc\cos(\omega t) + Z\sin(\omega t) + Z^3\sin^3(\omega t) = Y\sin(\omega t + \phi). \tag{4.14}$$

The aim at this point is to write all of equation (4.14) as coefficients of $\sin(\omega t)$ and $\cos(\omega t)$ such that, by equating coefficients of each, one obtains two equations which can then be solved simultaneously. While the forcing term on the right hand side $Y\sin(\omega t + \phi)$ can easily be expanded into coefficients of $\sin(\omega t)$ and $\cos(\omega t)$ using elementary trigonometry relations, expansion of the term $\sin^3(\omega t)$ will reveal higher order harmonics ($\sin(3\omega t)$ for example). However, one can simply choose to ignore these super harmonics (such that one is solving for the first harmonic only) and proceed with equating coefficients of $\sin(\omega t)$ and $\cos(\omega t)$. Indeed, one does not necessarily have to use elementary trigonometry relations at all but can simply expand the nonlinear term using the Fourier series.

With harmonic balance appearing more straightforward compared to the perturbation method, the following section details the application of harmonic balance to approximate the frequency response of the Mann and Sims energy harvester.

Examples of this method being applied to a variety of problems can be found in [34].

4.3 Energy harvester frequency response by harmonic balance

Recalling the equation of motion of the device:

$$m\ddot{z} + c\dot{z} + F_c \operatorname{sgn}(\dot{z}) + kz + k_3 z^3 = -m\ddot{y}. \tag{4.15}$$

(where for simplicity, c represents a combination of mechanical and electrical damping) then, the aim of the following analysis is to analyse the response of the system to a sinusoidal excitation of different frequencies (such that its frequency response is obtained). Consequently, a sinusoidal base displacement is defined:

$$y = Y \sin(\omega t + \phi) \tag{4.16}$$

where Y is the displacement amplitude, ω is the frequency of excitation and ϕ represents the phase difference between the excitation and the response. It is well known that, although excited at a single frequency, the response of a nonlinear system may also contain other harmonics above and/or below that of the excitation frequency (see [31, 32, 33] for a detailed discussion). For the purpose of this analysis it is assumed that the response of the device is dominated by the first harmonic. Consequently, it is assumed that the solution to equation (4.15) is of the form:

$$z = Z \sin(\omega t), \tag{4.17}$$

(noting that the phase term (ϕ) has been transferred to the input y as it helps to simplify matters later). Taking equation (4.16), differentiating twice and rewriting using elementary trigonometric relations allows one to write:

$$\ddot{y} = -\omega^2 Y(\sin(\omega t)\cos(\phi) + \cos(\omega t)\sin(\phi)). \tag{4.18}$$

Inserting equations (4.16) and (4.17) into equation (4.15) one obtains:

$$-m\omega^2 Z\sin(\omega t)+c\omega Z\cos(\omega t)+kZ\sin(\omega t)+k_3Z^3\sin^3(\omega t)+F_c\,\mathrm{sgn}(\cos(\omega t))$$

$$=-m\omega^2 Y(\sin(\omega t)\cos(\phi)+\cos(\omega t)\sin(\phi)). \tag{4.19}$$

The coefficient of F_c was then expanded up to the first harmonic using the Fourier series (this takes the form of the well known Fourier series expansion of a square wave):

$$\mathrm{sgn}(\cos(\omega t))=\frac{4}{\pi}\cos(\omega t)-\frac{4}{3\pi}\cos(3\omega t)+\frac{4}{5\pi}\cos(5\omega t)-... \tag{4.20}$$

such that, if one only considers the first harmonic:

$$\mathrm{sgn}(\cos(\omega t))\approx\frac{4}{\pi}\cos(\omega t). \tag{4.21}$$

The coefficient of k_3 was then expanded using elementary trigonometric relations (again, ignoring superharmonics) to find that:

$$Z^3\sin^3(\omega t)=Z^3\left(-\frac{1}{4}\sin(3\omega t)+\frac{3}{4}\sin(\omega t)\right)\approx Z^3\frac{3}{4}\sin(\omega t). \tag{4.22}$$

Substituting these approximations into equation (4.19):

$$-m\omega^2 Z\sin(\omega t)+c\omega Z\cos(\omega t)+kZ\sin(\omega t)+k_3Z^3\left(\frac{3}{4}\sin(\omega t)\right)+\frac{4F_c}{\pi}\cos(\omega t) \tag{4.23}$$

$$=-m\omega^2 Y(\sin(\omega t)\cos(\phi)+\cos(\omega t)\sin(\phi)). \tag{4.24}$$

One can now perform the harmonic balance procedure. Equating coefficients of $\sin(\omega t)$ and $\cos(\omega t)$ one obtains two equations:

$$-m\omega^2 Z+kZ+\frac{3}{4}k_3Z^3=-m\omega^2 Y\cos(\phi), \tag{4.25}$$

$$c\omega Z+\frac{4}{\pi}F_c=-m\omega^2 Y\sin(\phi). \tag{4.26}$$

Squaring and summing equations (4.25) and (4.26) one can make use of the fact that $\cos^2(\phi)+\sin^2(\phi)=1$ to obtain:

$$\left(-m\omega^2 Z + kZ + \frac{3k_3 Z^3}{4}\right)^2 + \left(c\omega Z + \frac{4F_c}{\pi}\right)^2 = m^2\omega^4 Y^2. \tag{4.27}$$

After manipulation, if was found that Z could be obtained by finding the roots of a sixth order polynomial:

$$Z^6\left(\frac{9k_3^2}{16}\right) + Z^4\left(-\frac{3}{2}m\omega^2 k_3 + \frac{3}{2}kk_3\right) + Z^2(m^2\omega^4 - 2m\omega^2 k + k^2 + c^2\omega^2)$$
$$+Z\left(\frac{8c\omega F_c}{\pi}\right) + \left(\frac{16F_c^2}{\pi^2} - m^2\omega^4 Y^2\right) = 0. \tag{4.28}$$

The solutions to equation (4.28) were found using the Matlab *roots* command [60]. Once Z was obtained the negative and imaginary solutions were neglected as being unphysical. Having shown that the electromagnetic coupling essentially acts as an additional viscous damping term (Chapter 3) then, for the purpose of this section, the output power of the device was found using the relation:

$$p = (\omega Z)^2 c. \tag{4.29}$$

To validate the analytical result, the model detailed in Chapter 3 was used to analyse the frequency response of the device. To achieve this, the model was subjected to a sinusoidal excitation and the resulting power output was monitored as the excitation frequency was stepped up or down. Figure 4.1 shows that there was a reasonably good match between the analytical and simulation results. It should be noted that gravity was included in the simulation runs, while in the harmonic balance analysis, gravity was ignored. This confirms that the DC component does not effect the power output of the device.

4.4 Friction Effects

The analysis shown above is based on the assumption that there is relative motion between the centre magnet and base of the device. Consequently, this approach is only valid if:

$$|c\dot{z} + kz + k_3 z^3 + m\ddot{y}| > |F_c\,\mathrm{sgn}(\dot{z})|, \tag{4.30}$$

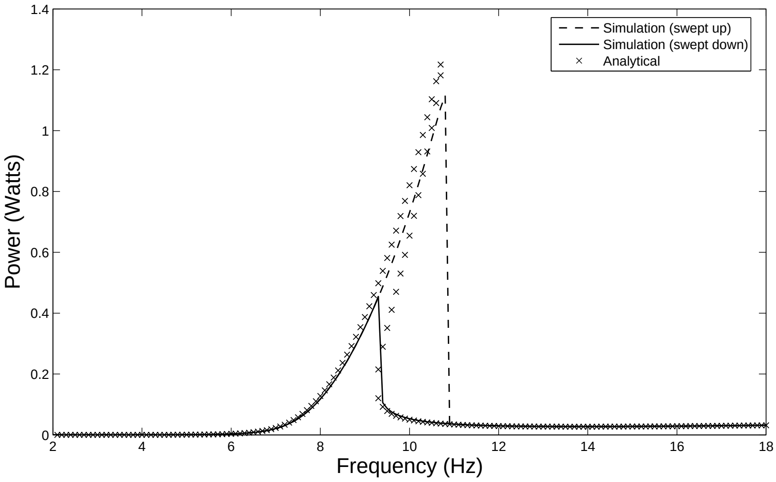

Figure 4.1: Power output of device at different frequencies where $m = 0.02$ kg, $k = 50$ N/m, $k_3 = 20000$ N/m^3, $c = 0.1$ Ns/m, $F_c = 0.01$ N, $Y = 4$mm and $g = 9.81$m/s^2. Crosses represent the analytical solutions (equation (4.28)) while dashed and solid lines represent stepped up and stepped down simulation results respectively.

such that the forces acting on the mass are large enough to overcome the friction in the system. As a result, the frequency where the device starts to move relative to the base (which will be termed the slipping frequency) is when:

$$|c\dot{z} + kz + k_3 z^3 + m\ddot{y}| = |F_c \, \mathrm{sgn}(\dot{z})|. \tag{4.31}$$

Applying the same harmonic balance procedure as shown in the previous section allows this to be written as:

$$\left(kZ + \frac{3}{4}k_3 Z^3\right)^2 \left(\omega Z c + \frac{4}{\pi}F_c\right)^2 = m^2\omega^4 Y^2, \tag{4.32}$$

where Z changes with ω according to equation (4.28). The value of ω that satisfies equation (4.32) will be the slipping frequency. Figure 4.2 shows the stepped up frequency response of the model (using the same techniques as the previous section) and shows that, when excited sinusoidally, equations (4.28) and (4.32) can be used to predict the frequency where the device moves from stick to slip behavior with a reasonable degree of accuracy. In Figure 4.2 (c) one can see that the increase in friction has lessened the effect of the nonlinear spring to the point where the jump phenomenon has been removed from the frequency response of the device.

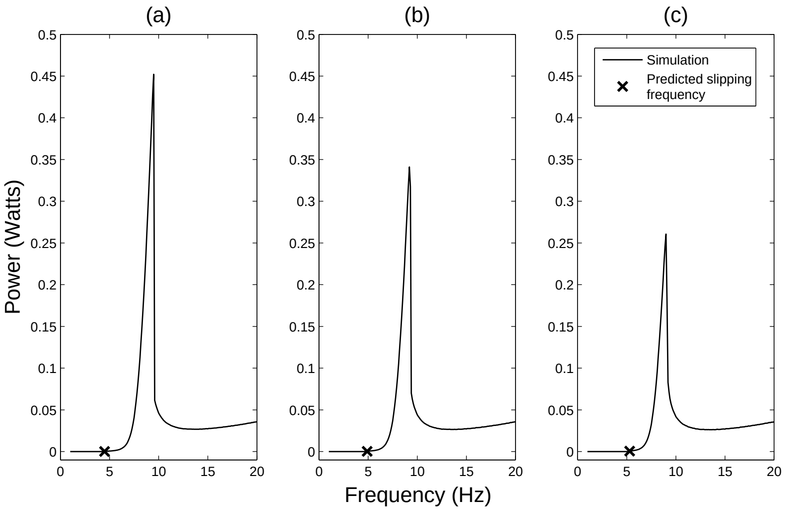

Figure 4.2: Power output of device at different frequencies where $m = 0.02$ kg, $c = 0.1$ N/s, $k = 50$ N/m, $k_3 =$ N/m^3, $Y = 0.004$ m and $F_c =$ (a) 0.05, (b) 0.06, (c) 0.07 N.

The same effect would occur if one was to increase the viscous damping present in the system. It remains to be seen how friction and Duffing-type nonlinearities influence the behavior of the device when it is under a random excitation. This will be discussed further in Chapter 7.

4.5 Summary

The aim of this chapter was to analyse the response of the Mann and Sims energy harvester to sinusoidal excitations. The analysis shown here differs from those which have been conducted before (Mann and Sims analysed the frequency response of this device using the method of multiple scales [30]) as the effects of friction are considered as well as the Duffing-type nonlinearity. This is as a consequence of the experimental investigation shown in Chapter 3 in which it was shown that friction effects must be considered if one is the accurately model the response of the device.

Using the method of harmonic balance, an expression for the frequency response of the friction affected Mann and Sims energy harvester is derived before being validated alongside digital simulations. It is then shown that the derived expressions can be used to accurately predict when the centre magnet will ‘stick’ (in other words, when the forces on the centre magnet are unable to overcome friction present in the system). The effect that friction can have on the frequency response of the device is then demonstrated.

Chapter 5

RANDOM EXCITATIONS: MONTE CARLO SIMULATION

5.1 Introduction

As mentioned in Chapter 2, one of the largest difficulties that one can encounter with regards to energy harvester design is the fact that the majority of ambient vibration sources are of a stochastic nature. This realisation was the main motivation for several works which focused on the response of energy harvesters to random excitations [38, 43, 51, 52] (these are discussed in more detail in Chapter 2). Consequently, the purpose of the next three chapters is to analyse the response of the Mann and Sims energy harvesting device [30] to random excitations. The analysis shown in the present chapter makes use of Monte Carlo simulations. However, before a discussion of this analysis is undertaken some key theoretical background is outlined in the following section.

5.2 Theoretical background

5.2.1 Randomness

Consider the following definition of the covariance function for two variables $x(t)$ and $y(t)$ [61]:

$$\mathrm{Cov}(x(t), y(t)) = E\left[(x(t) - E[x(t)])(y(t) - E[y(t)])\right] \tag{5.1}$$

where E represents the expected value. Upon studying equation (5.1) one can see that, if the variable x tends to be increasing with t when the variable y is also increasing with t then the covariance will be positive and likewise if both variables tend to be decreasing at the same time. Clearly then, if x tends to be increasing when y is decreasing of visa versa then the covariance will be negative. The covariance then, is a measure of how much the two signals x and y look like each other, or in other words, it is measure of their *correlation*. In fact, most probability text books ([61] for example) will recommend using the correlation coefficient for this measure:

$$\rho_{xy} = \frac{\mathrm{Cov}(x(t), y(t))}{\sigma_x \sigma_y}, \tag{5.2}$$

where σ_x and σ_y represent the standard deviation of x and y respectively. This is because the correlation coefficient will return a value of 1 if the signals are perfectly correlated and 0 if they are uncorrelated. For now though, we will only consider the non-normalised version (equation (5.1)). What then, if one wanted to know how much a signal looked like a *time shifted version of itself*? In such a case one would use:

$$\phi_{xx}(\tau) = E[x(t)x(t+\tau)] \tag{5.3}$$

which is termed the autocorrelation of the signal x. Clearly, at $\tau = 0$ the autocorrelation will be large as one has evaluated how much the signal looks like an exact replica of itself. However, if x is perfectly random, then there should be no correlation whatsoever between $x(t)$ and $x(t+\tau)$ when $\tau \neq 0$ and, consequently, the autocorrelation should be zero. This is used as a definition of randomness throughout this thesis. It should be noted however that such a signal cannot be created using digital simulations (which by definition can only produce pseudo-random numbers) although it is possible to achieve a close approximation of a random signal.

5.2.2 Stationarity

In the context of this work, a random variable is said to be stationary if its statistical moments do not change with time. As an example, consider the random variable x with stationary probability density function (PDF) $P(x)$. Consequently, by sampling x from $P(x)$ at consecutive time intervals to realise the vector $\{x(t_1), x(t_2), x(t_3), ..., x(T)\}$ then the expected value of x can be approximated by:

$$E[x] \approx \frac{1}{T} \sum_{i=1}^{T} x(t_i). \tag{5.4}$$

Likewise, if one were to take continues samples of x then:

$$E[x] \approx \frac{1}{T} \int_{0}^{T} x(t)dt. \tag{5.5}$$

5.2.3 Properties of Autocorrelation

The autocorrelation possesses several properties which are utilised in this chapter. Defining x as a stationary random variable (using the definitions provided in the previous sections) with an expected value of zero then, by setting $\tau = 0$, the autocorrelation of x (equation (5.3)) becomes the variance of x:

$$\phi_{xx}(0) = E[x(t)^2] = \sigma_x^2 \tag{5.6}$$

(as $\text{Var}(x) = E[x^2] - (E[x])^2$ and $E[x] = 0$ in this case). Additionally, the autocorrelation is related to the power spectral density (PSD) of x (denoted $P_{xx}(\omega)$) by the relation:

$$\phi_{xx} = \mathcal{F}^{-1}[P_{xx}(\omega)] \tag{5.7}$$

where $\mathcal{F}^{-1}$ represents the inverse Fourier transform - this result is proved in Appendix B.2. The importance of these properties with regards to the digital simulation of white noise is discussed in the next section.

5.2.4 Gaussian White Noise

In much of this chapter Gaussian white noise signals are used as the ambient vibration source for the energy harvester in question. What follows in the subsequent two sections is an analytical definition of such a signal as well as a discussion on how it can be generated within digital simulations.

Analytical

An analytical Gaussian white noise process is a random signal which has zero mean and a flat PSD over an infinite bandwidth of frequencies. Defining $S/2$ as the height of the PSD over a frequency range from zero to infinity then, recalling equation (5.7), one can write:

$$\phi_{xx}(\tau) = \frac{1}{2\pi}\int_0^\infty \frac{S}{2}\exp(i\omega\tau)d\omega = \frac{S}{2}\delta(\tau), \tag{5.8}$$

where δ is the Dirac delta function. This then agrees with the definition of randomness that was given in section 5.2.1 as the autocorrelation is equal to infinity when $\tau = 0$ but is zero when $\tau \neq 0$. Consequently, the analytical Gaussian white noise signal also has infinite variance:

$$\sigma_x^2 = \phi_{xx}(0) = \frac{1}{2\pi}\frac{S}{2}\int_0^\infty d\omega = \infty. \tag{5.9}$$

Finite Bandwidth

Although white noise is a useful mathematical concept, it is impossible to achieve in reality as it has infinite power (as shown in equation (5.9)). If one were to digitally simulate white noise then the bandwidth over which it has a flat PSD will be limited by the sample frequency of the simulation. As a result, the variance of the digitally simulated signal is given by:

$$\sigma_x^2 = \phi_{xx}(0) = \frac{1}{2\pi}\frac{S}{2}\int_0^{2\pi f_s} d\omega = \frac{S}{2}f_s, \tag{5.10}$$

where f_s is the sampling frequency (in Hertz). Consequently, for a bandwidth limited simulation to replicate an analytical white noise signal with PSD height equal to $S/2$, its variance must be scaled according to equation (5.10). Similarly, if one wanted to create a flat PSD over a bandwidth between the frequencies f_1 and f_2 then the required variance would be given by:

$$\sigma_x^2 = \frac{1}{2\pi}\frac{S}{2}\int_{2\pi f_1}^{2\pi f_2} d\omega = \frac{S}{2}(f_2 - f_1). \tag{5.11}$$

This then, is how analytical white noise was digitally approximated in the simulations detailed within this chapter.

5.2.5 Monte-Carlo simulation

One of the issues associated with investigating the response of systems to random excitations is that, even if one can confidently model the physics of the system, it will never be possible to *exactly* predict its behavior as the excitation is likely to be different for each simulation. For example, consider the digital simulation of a simple mass-spring-damper arrangement:

$$m\ddot{x} + c\dot{x} + kx = w(t) \tag{5.12}$$

where $w(t)$ is a Gaussian white noise process as described earlier in this chapter. Figure 5.1 shows the response from 100 different simulations of this system (in grey). Clearly, the response of each simulation is different. However, if one were to take the mean of all 100 simulation results at each moment in time then one can plot the 'ensemble average' response of the system (the thick black line in Figure 5.1). This is not only restricted to the first statistical moment (the dashed line on Figure 5.1 represents the ensemble standard deviation). This method of approximating the statistical properties of the system is referred to as Monte Carlo simulations. Clearly, the more simulations used in the ensemble leads to closer approximations of its average behavior - the obvious disadvantage of Monte Carlo simulations being their computational cost. For a more detailed discussion of Monte Carlo methods

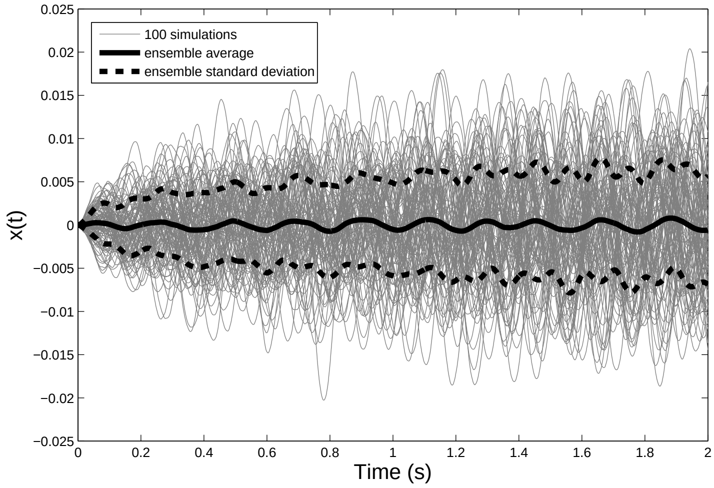

Figure 5.1: Monte Carlo simulation of a mass spring damper under white Gaussian excitation conditions.

the following texts are recommended: [62, 63].

5.3 Monte Carlo Analysis

The aim of the work in this section was to use Monte Carlo simulations to analyse the response of the Mann and Sims energy harvester to different types of random excitation when different levels of spring nonlinearity, viscous damping and friction were present. The hazard with this method of analysis comes from the fact that, in Chapter 3, the model was only validated at one set of parameter values. Consequently, by running simulations using parameter values different from those that were used experimentally, one may inadvertently move into a region of parameter space where the model does not replicate reality well.

To alleviate this issue, recall that the model was validated using different intensities of excitation acceleration. Given that the effects of Duffing-type nonlinearities are known to be more significant when larger amplitude excitations are used (see [33]) then, by altering the amplitude of excitation, one can hypothesise that the *effect* of the nonlinear term was altered in each test (even though the nonlinear term itself was kept constant). In a similar manner it is fairly intuitive to suggest that the effects of friction on device performance will be more severe when the excitation amplitude is low thus, by validating the model using different amplitudes of excitation, one has investigated different levels of friction importance.

As a result, as part of the following work, a dimensional analysis of the energy harvester model is conducted. This is a technique which involves arranging all of the parameters of interest into dimensionless groups - it is based on the fact that the physical phenomenon one witnesses must be independent of the dimensions they were observed in. Using this analysis it is shown that the effect of varying nonlinear spring and friction terms was analysed through a variation in excitation amplitude.

In the following section, for the sake of simplicity, it is assumed that all of the viscous damping is due to the device electromagnetic coupling. This approach therefore predicts the maximum theoretical power that could be harvested from the device if all of the viscous damping present was due to the electromechanical coupling.

5.3.1 Broadband White Noise

Initially, the response of the device to a Gaussian white noise base acceleration was analysed, such that the equation of motion being simulated was:

$$m\ddot{z} + c\dot{z} + kz + k_3 z^3 + F_c \dot{z} = -mw(t) \tag{5.13}$$

where

$$E[w(t)] = 0 \tag{5.14}$$

and

$$\phi_{ww}(\tau) \approx \frac{S}{2}\delta(\tau) \tag{5.15}$$

(as discussed in section 5.2.4).

Dimensional Analysis

As stated earlier, dimensionless groups corresponding to the power output, viscous damping, nonlinear stiffness and Coulomb damping of the device were formed such that the simulation results acquired were independent of device dimensions. Firstly, it was assumed that the power output of the device was a function of the following variables:

$$\sigma_P = f(\sigma_{\ddot{y}}, m, c, k, k_3, F_c), \tag{5.16}$$

where σ_P is the root mean square (RMS) power available from the device, $\sigma_{\ddot{y}}$ is the RMS acceleration of the base, m is the mass of the central magnet, c represents the damping in the system due to electromagnetic coupling, k and k_3 are the linear and nonlinear stiffness terms respectively and F_c is the coulomb damping coefficient. The primary variables chosen were base acceleration, mass and linear stiffness where

$$[\sigma_{\ddot{y}}] = LT^{-2}, \tag{5.17}$$

$$[m] = M, \tag{5.18}$$

$$[k] = MT^{-2}. \tag{5.19}$$

(throughout M, L and T are used to represent the dimensions mass, length and time respectively). The first dimensionless group was found using the power term:

$$\pi_P = \sigma_P \sigma_{\ddot{y}}^{a_1} m^{a_2} k^{a_3} \tag{5.20}$$

therefore:

$$[\pi_P] = M^{1+a_2+a_3} L^{2+a_1} T^{-3-2a_1-2a_3} = 1, \tag{5.21}$$

such that, solving for a_1, a_2 and a_3:

$$\pi_P = \frac{\sigma_P \omega_n}{\sigma_{\ddot{y}}^2 m}. \tag{5.22}$$

The second dimensionless group was found using the damping term:

$$\pi_c = c\sigma_{\ddot{y}}^{a_1} m^{a_2} k^{a_3} \tag{5.23}$$

therefore:

$$[\pi_c] = M^{1+a_2+a_3} L^{a_1} T^{-1-2a_1-2a_3} = 1 \tag{5.24}$$

which leads to the relationship:

$$\pi_c = \frac{c}{\sqrt{km}}. \tag{5.25}$$

It is noted here that this group is the same as double the damping ratio that one finds in a linear mass-spring-damper system. The third dimensionless group was found using the nonlinear stiffness term:

$$\pi_{k_3} = k_3\sigma_{\ddot{y}}^{a_1} m^{a_2} k^{a_3} \tag{5.26}$$

therefore:

$$[\pi_{k_3}] = M^{1+a_2+a_3} L^{-2+a_1} T^{-2-2a_1-2a_3} = 1, \tag{5.27}$$

which leads to the relationship:

$$\pi_{k_3} = \frac{k_3\sigma_{\ddot{y}}^2 m^2}{k^3}. \tag{5.28}$$

The final dimensionless group was found using the coulomb damping term:

$$\pi_{F_d} = F_d\sigma_{\ddot{y}}^{a_1} m^{a_2} k^{a_3} \tag{5.29}$$

therefore:

$$[\pi_{F_d}] = M^{1+a_2+a_3} L^{1+a_1} T^{-2-2a_1-2a_3} = 1, \tag{5.30}$$

which leads to the relationship:

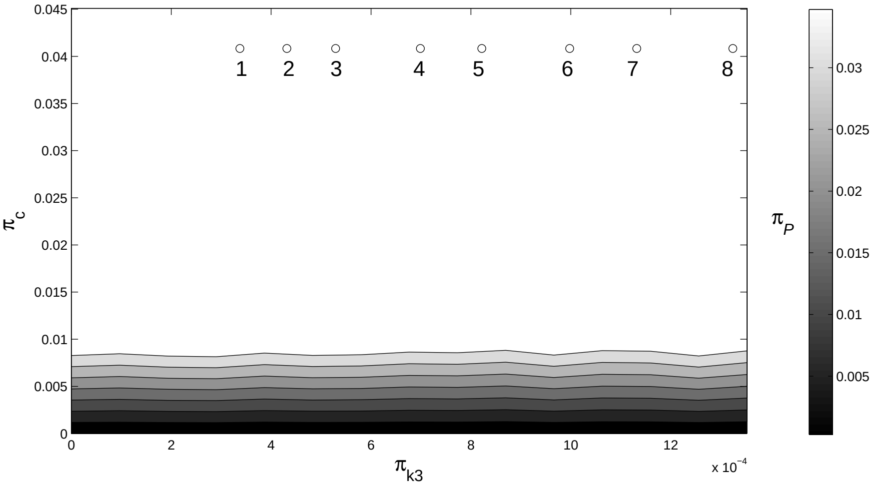

Figure 5.2: The variation of dimensionless power output as k_3 and c are varied according to simulation results. Circles represent points where the model was validated while the values next to them represent the corresponding excitation condition.

$$\pi_{F_d} = \frac{F_d}{\sigma_{\ddot{y}} m}. \tag{5.31}$$

As a result, one is left with four dimensionless groups, each one containing one of the parameters being investigated.

Results

Initially, it was assumed that there was no friction present in the simulated system. Monte Carlo simulations were run using different values of nonlinear stiffness and linear damping. It was ensured that the simulation results were independent of the simulation run time and sampling frequency. The dimensionless form of the results are shown in Figure 5.2 where the circles represent excitation conditions where the model was experimentally validated (Table 3.1 of Chapter 3). The simulation results suggest that the introduction of the spring nonlinearity into the system has no effect on its power output - a result which will be proved analytically in Chapter 6. It also seems to indicate a threshold value of damping ratio, above which, the dimensionless power output of the system does not increase.

Having established that the nonlinear spring term does not affect the power output of the system, k_3 was set to zero and Monte Carlo simulations were used to investigate

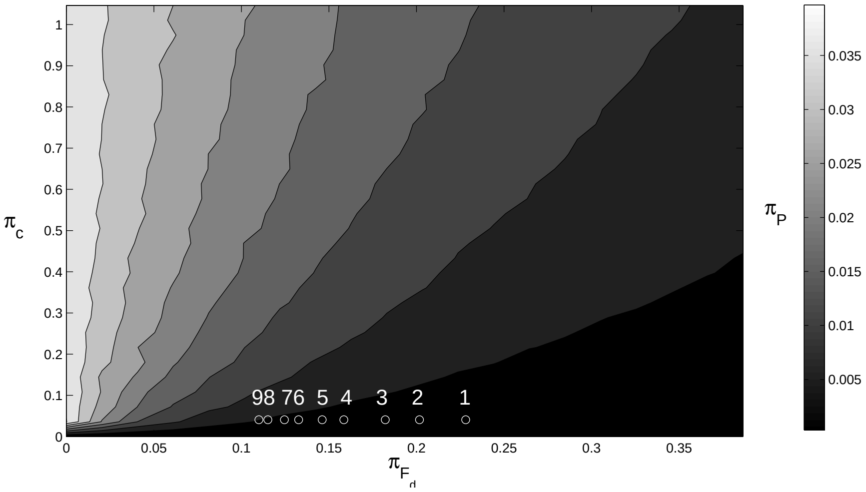

Figure 5.3: The variation of power output as F_d and c are varied according to simulation results where circles represent points where the model was validated.

the relation between friction, viscous damping and power output. The resulting contour plot is shown in Figure 5.3. It can clearly be seen that increased Coulomb damping has a detrimental effect on the dimensionless power output of the device. It is also clear that the device is less sensitive to the harmful effect of friction when a relatively large electromechanical coupling is present. This is because the system's energy dissipation is dominated by the coupling and, consequently, is not greatly effected by changes in friction. For the purposes of validation, it was ensured that the results demonstrated in Figure 5.3 were independent of values of k_3.

5.3.2 Coloured Noise

Having used Monte Carlo simulations to analyse the response of the device to Gaussian white noise excitations, the subsequent aim was to perform a similar investigation using coloured noise excitations.

Signal Generation

To generate the coloured noise base acceleration, a white noise signal was passed through a second order filter such that:

$$\ddot{y} + 2\omega_c\Theta\dot{y} + \omega_c^2 y = w(t), \tag{5.32}$$

where $w(t)$ is a Gaussian white noise signal, ω_c is the natural frequency and Θ is the damping ratio of the filter. An example of the resulting base acceleration spectrums is shown in Figure 5.4.

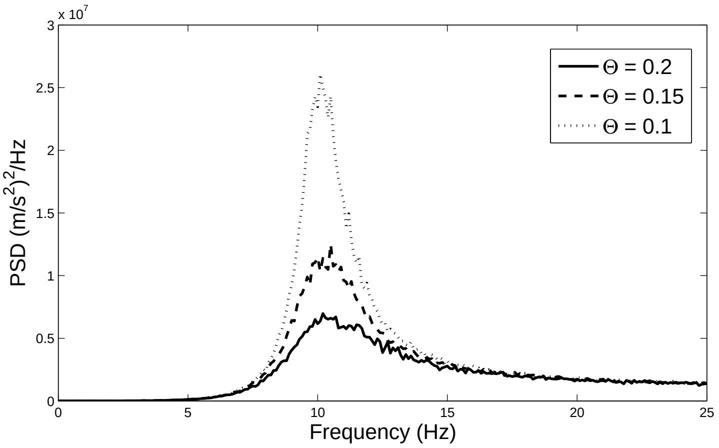

Figure 5.4: Example base accelerations power spectral densities created with second order filter where $\omega_c = 2\pi 10$ rad/s. Solid, dashed and dot-dashed lines represent power spectral densities where $\Theta = 0.2$, 0.15 and 0.1 respectively.

Dimensional Analysis

It is now assumed that the RMS power output of the device is a function of the following variables:

$$\sigma_P = f(\sigma_{\ddot{y}}, m, c, k, k_3, F_d, \omega_c, \Theta) \tag{5.33}$$

Once again, the primary variables were chosen as $\sigma_{\ddot{y}}$, m and k. As a result, all the derived groups were the same as those shown in the previous section except for the addition of two additional groups:

$$\pi_{\omega_c} = \frac{\omega_c m^{1/2}}{k^{1/2}}, \tag{5.34}$$

$$\pi_\Theta = \Theta \tag{5.35}$$

(noting that π_{ω_c} is the ratio of the filter and device natural frequencies and that, $\pi_\Theta = \Theta$ as Θ was already a dimensionless quantity).

Results

For the first set of Monte-Carlo simulations, π_c was held constant and π_{F_c} was set to zero. As a result, the value of π_P was monitored as the π_{k_3}, π_{ω_c} and π_Θ groups were varied. Figure 5.5 shows how π_P varies with π_{k_3} when the natural frequency of the device is equal to that of the filter ($\pi_{\omega_c} = 1$). It can be seen that an increase in k_3 is detrimental to the power output of the device but that this detrimental effect reduces as π_Θ is increased.

To explain this one must recall that the introduction of such a nonlinearity shifts the natural frequency of the device to higher frequencies (as demonstrated in Chapter 2). As π_{ω_c} was set to 1 then the linear natural frequency of the device had been chosen to match the dominant frequency of the excitation. Consequently, by increasing k_3 the natural frequency of the device was being shifted away from the dominant frequency of the excitation and the power output was being reduced as a result. However, as π_Θ is increased then the relative importance of the excitation dominant frequencies reduces (as was shown in Figure 5.4) and so the detrimental effect of increasing k_3 is less significant. If one were to increase Θ to the point where there were no dominant frequencies present in the excitation then the signal would become broadband white noise and k_3 would have no effect on power output (as was shown previously).

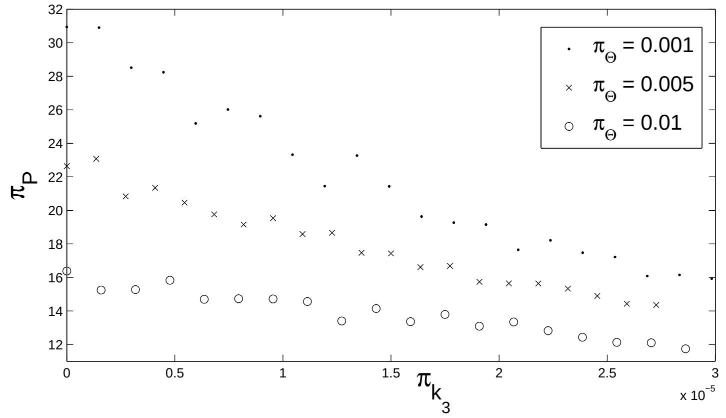

Figure 5.5: Variation of π_P as π_{k3} is varied where $\pi_c = 0.03$, $\pi_{\omega_c} = 1$ and $\pi_{F_d} = 0$. Dots, crosses and circles represent results where $\pi_\Theta = 0.001$, 0.005 and 0.01 respectively.

Figure 5.6 shows a scenario where the natural frequency of the device is less than that of the dominant frequencies in the excitation ($\pi_{\omega_c} = 1.2$). In this case it can be seen that by increasing k_3 the natural frequency of the device has been shifted closer to the dominant frequency of the device and power output has increased as a result.

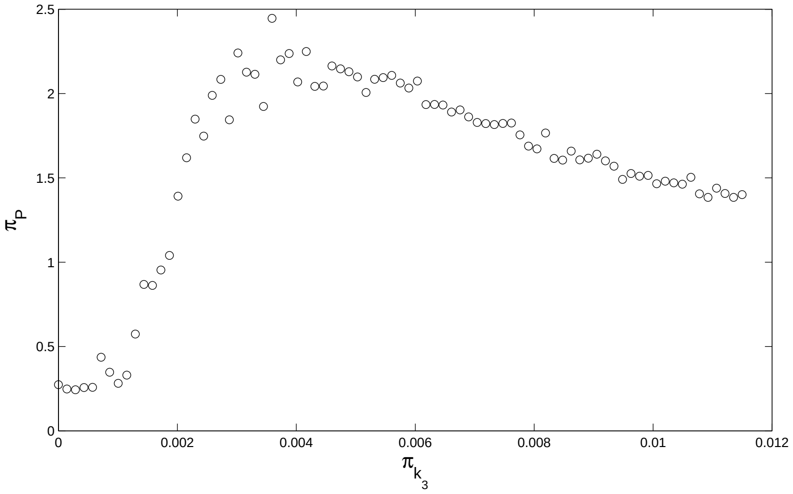

Figure 5.6: Variation of π_P as π_{k3} and π_Θ is varied where $\pi_c = 0.03$, $\pi_{\omega_c} = 1.2$ and $\pi_{F_d} = 0$.

For the second set of simulations, the effect of π_{F_c} on the power output of the device for different values of π_Θ was investigated. Figure 5.7 shows that increased friction is detrimental to device performance (an one would expect). It also shows that as the excitation approaches broadband noise then the relative effect of friction on power output is reduced.

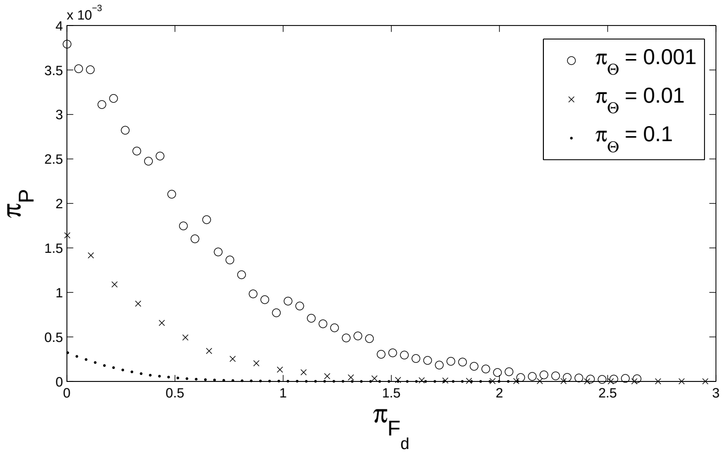

Figure 5.7: Variation of π_P as π_{F_d} and π_Θ are varied where $\pi_{\omega_c} = 1$, $\pi_c = 0.15$ and $\pi_{k_3} = 0$. Circles, crosses and dots represents results where $\pi_\Theta = 0.001$, 0.01 and 0.1 respectively.

Finally, the relationship between π_P, π_c and π_{F_d} was analysed. Figure 5.8 shows an optimum level of damping where the useful bandwidth of the energy harvester is wide enough to capture the energy in the coloured noise signal. This differs from the white noise simulations were no optimum level of damping was present.

Furthermore, it is shown that the introduction of friction into the system doesn't have a great effect on the optimum damping level. It can also be seen that, as with the white noise case, the sensitivity of the system's power output to changes in friction decreases when relatively large levels of electromechanical coupling are used.

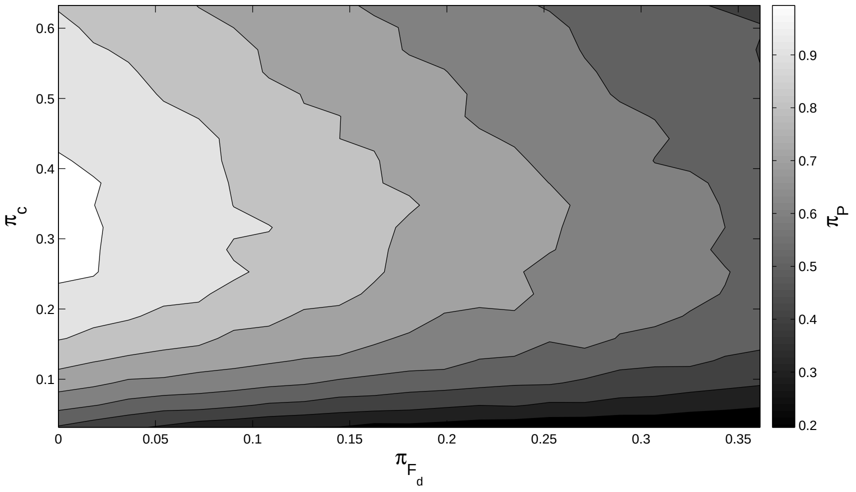

Figure 5.8: Variation of π_P as π_{F_d} and π_c is varied where $\pi_{\omega_c} = 1$, $\pi_{k_3} = 0$ and $\pi_\Theta = 0.05$.

5.4 Summary

In this chapter, the response of the Mann and Sims energy harvester to random excitations was analysed using Monte Carlo simulations. A key finding from these simulation results is that, over the parameter space that was investigated, Duffing-type nonlinearities cannot be used to improve the power output of the Mann and Sims energy harvester when it is subject to a white noise excitation (this is proved over the entire parameter space in Chapter 6). With regards to coloured noise excitations, it was shown that Duffing-type nonlinearities (of the hardening variety) may only prove useful if one needed to tune the natural frequency of the device to a higher value without changing the mass or linear stiffness terms. It should also be noted that if the kinetic energy losses present in the device were too high or the excitation level too low then the level of nonlinearity required to shift the natural frequency may be too large to be achieved practically. Finally, for all the excitation types investigated, it was shown that the sensitivity of such an energy harvester to friction effects can be reduced via an increase in electromechanical coupling. The investigation of friction is likely to be significant for many practical applications where energy capture involves electromagnetic, rather than piezoelectric phenomenon, since electrical machines will generally require mechanical bearings.

Chapter 6

RANDOM EXCITATIONS: FOKKER-PLANCK-KOLMOGOROV EQUATION

6.1 Introduction

In the previous chapter the response of the Mann and Sims energy harvester to random excitations was investigated using Monte-Carlo simulations. While a useful tool, Monte Carlo simulations are computationally expensive and can only be carried out over a finite region of parameter space. Consequently, in this chapter an analytical expression describing the response of the device in question to a Gaussian white noise excitation is developed using the Fokker-Planck-Kolmogorov (FPK) equation. This expression is then used to analyse the effect of Duffing-type nonlinearities on the response of the device over the entire parameter space. The FPK equation is the main tool used in this chapter and, as a result, it is derived in the following section.

6.2 Fokker-Planck-Kolmogorov equation

In the previous chapter it was shown that, when studying a randomly excited system, one should consider the average response of an ensemble of experiments as opposed to the response of a single experiment (Figure 5.1). Upon studying Figure 5.1 one can suppose that, for each moment in time, one could fit a probability density function (PDF) for the system. The Fokker-Planck-Kolmogorov (FPK) equation can be used to derive an expression detailing how this PDF changes with time. Full derivations of the FPK equation tend to be fairly lengthy and so a relatively brief derivation is shown in the subsequent sections. For more detailed derivations of the FPK equation and examples of its applications to some dynamic systems, references [64] and [65] are suggested.

Markov Processes

Before deriving the FPK equation one must first consider the definition of a Markov process. Essentially, a Markov process is one whose current state only depends on the state immediately preceding it. For example, consider a random process $x(t)$ which has been sampled at times $\{t_1, t_2, t_3, ...\}$. If not a Markov process then the probability of x at time t_n (denoted $P(x_n, t_n)$) could be conditional on all the past values of x:

$$P(x_n, t_n) = P(x_n, t_n | x_{n-1}, t_{n-1}; x_{n-2}, t_{n-2} ...; x_1, t_1; x_0, t_0). \tag{6.1}$$

A Markov process is defined as a process where the PDF of x at time t_n is only dependent on the preceding value of x such that:

$$P(x_n, t_n) = P(x_n, t_n | x_{n-1}, t_{n-1}). \tag{6.2}$$

Analytical white noise is, by definition, a Markov process. The white noise excited dynamic systems addressed in this chapter can all be considered Markov processes as, when modelled discretely in state space form, calculation of the next state depends only on the current state.

Chapman-Kolmogorov equation

Consider a Markov process where a variable x transfers from the value x_1 to x_2 between times t_1 and t_2, as shown in Figure 6.1, where z is defined as the difference between x at time t_1 and x at time t_2 (so $z = x_2 - x_1$ in Figure 6.1)[1].

Given that $x = x_1$ at time t_1 then the probability that it reaches the value x_2 and time t_2 is given by $P(x_2, t_2|x_1, t_1)$. Consequently, the probability of seeing $x = x_2$ at time t_2 is given by the law of total probability [61]:

$$P(x_2, t_2) = \int_{-\infty}^{\infty} P(x_2, t_2|x_1, t_1)P(x_1, t_1)dx_1. \tag{6.3}$$

which is the Chapman-Kolmogorov equation for a Markov process. Now, if one defines $Q(z, t_2 - t_1)$ as a *transition density* which represents the probability that x changes by the value z between times t_1 and t_2 then the probability of seeing $x = x_2$ at time t_2 can also be written as:

$$P(x_2, t_2) = \int_{-\infty}^{\infty} P(x_2 - z, t_1)Q(z, t_2 - t_1)dz. \tag{6.4}$$

This has an intuitive quality: it states that the probability that $x = x_2$ at time t_2 is equal to the probability that, at time t_1, x differs from x_2 by the amount $-z$ multiplied by the probability that, between t_1 and t_2, x changes by the amount z (thus becoming x_2 at time t_2). In a more general notation this can be written:

$$P(x, t + \delta t) = \int_{-\infty}^{\infty} P(x - z, t)Q(z, \delta t)dz \tag{6.5}$$

where $Q(z, \delta t)$ represents the probability that x changes by the value z over the time increment δt. This form of the Chapman-Kolomogorov equation is used throughout this chapter.

Recalling that this chapter will be concerned with the response of a SDOF system whose state is defined by two state space variables (displacement and velocity) then the Chapman-Kolmogorov equation for two variables will be defined here. In a slight change of notation then, we choose x_1 and x_2 such that they now represent two different variables (rather than the values of x at different times). The Chapman-Kolmogorov equation for two variables is:

---

[1] In other parts of this thesis z is used to represent relative displacement but this will be clearly indicated to avoid confusion.

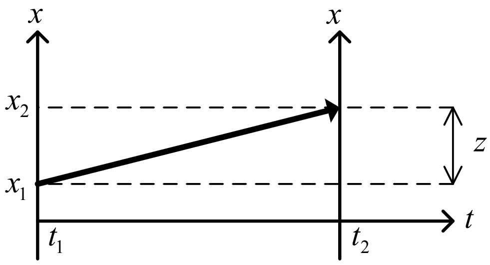

Figure 6.1: Example Markov process.

$$P(x_1, x_2, t + \delta t) = \int_{-\infty}^{\infty} \int_{-\infty}^{\infty} P(x_1 - z_1, x_2 - z_2, t) Q(z_1, z_2, \delta t) dz_1 dz_2 \tag{6.6}$$

where z_1 and z_2 now represent changes in x_1 and x_2 respectively.

FPK derivation

Having defined a Markov process and the Chapman-Kolmogorov equation, one can then derive the FPK equation. Expanding equation (6.6) using the multivariate Taylor series[2] then, after a little manipulation, one can write:

$$\frac{\partial P(x_1, x_2, t + \delta t)}{\partial t} = -\sum_{i=1}^{2} \left[\frac{\partial P(x_1, x_2, t)}{\partial x_i} \frac{\bar{z}_i}{\delta t} \right] + \frac{1}{2} \sum_{i=1}^{2} \sum_{j=1}^{2} \left[\frac{\partial^2 P(x_1, x_2, t)}{\partial x_i \partial x_j} \frac{\bar{z}_i \bar{z}_j}{\delta t} \right] \tag{6.7}$$

where

$$\bar{z}_i = \int_{-\infty}^{\infty} \int_{-\infty}^{\infty} z_i Q(z_1, z_2 \delta t) dz_1 dz_2 \tag{6.8}$$

and

$$\bar{z}_i \bar{z}_j = \int_{-\infty}^{\infty} \int_{-\infty}^{\infty} z_i z_j Q(z_1, z_2, \delta t) dz_1 dz_2. \tag{6.9}$$

The algebra behind these steps is shown in more detail in [64]. If one now considers a SDOF system (with a nonlinear stiffness function):

$$\ddot{x} + c\dot{x} + \Phi(x) = w(t) \tag{6.10}$$

---

[2] For a derivation of the multivariate Taylor series the author recommends consulting Stroud [66].

where $w(t)$ is Gaussian white noise as defined previously, then, defining the state space variables:

$$x_1 = x \tag{6.11}$$

$$x_2 = \dot{x}, \tag{6.12}$$

the FPK equation for this system is given by:

$$\begin{aligned}\frac{\partial P(x_1, x_2, \delta t)}{\partial t} &= -x_2 \frac{\partial P(x_1, x_2, t)}{\partial x_1} + \frac{\partial}{\partial x_2}\left[(cx_2 + \Phi(x_1))P(x_1, x_2, t)\right] \\ &\quad + \frac{S}{4}\frac{\partial^2 P(x_1, x_2, t)}{\partial x_2^2}. \end{aligned} \tag{6.13}$$

This is proved in Appendix B.3. In such a case one can solve for the stationary PDF of the system by setting $\partial P(x_1, x_2, \delta t)/\partial t$ equal to zero:

$$0 = -x_2 \frac{\partial P(x_1, x_2, t)}{\partial x_1} + \frac{\partial}{\partial x_2}\left[(cx_2 + \Phi(x_1))P(x_1, x_2, t)\right] + \frac{S}{4}\frac{\partial^2 P(x_1, x_2, t)}{\partial x_2^2}. \tag{6.14}$$

6.3 Analysis via the FPK equation

6.3.1 Formation

In this section, the response of the device to Gaussian white noise base accelerations is analysed using the FPK equation. The equation of motion of the Mann and Sims device is now normalised by the mass and written as:

$$\ddot{z} + (2\omega_n\zeta + \gamma/m)\dot{z} + \omega_n^2 z + \beta z^3 = -w(t) \tag{6.15}$$

where z now represents relative displacement, ω_n is the natural frequency, ζ is the damping ratio, $\beta = k_3/m$, $\gamma = \alpha^2/(R_L + R_C)$ and $w(t)$ is zero mean Gaussian white noise with autocorrelation $\phi_{ww}(\tau) = \frac{S}{2}\delta(\tau)$. Allowing $z_1 = z$ and $z_2 = \dot{z}$ then the FPK equation needed to find the stationary probability density function (PDF) of the device is given by:

$$0 = -\frac{\partial}{\partial z_1}(z_2 P) + \frac{\partial}{\partial z_2}\left(\left((2\omega_n\zeta + \gamma/m)\, z_2 + \omega_n^2 z_1 + \beta z_1^3\right) P\right) + \frac{S}{4}\frac{\partial^2}{\partial z_2^2}P, \tag{6.16}$$

where $P(z_1, z_2, t)$ is simply written as P. Using the relation $\eta = 2\omega_n\zeta + \gamma/m$ for the sake of readability, equation (6.16) can then be written as:

$$0 = \left[-z_2\frac{\partial P}{\partial z_1} + \frac{\partial P}{\partial z_2}(\omega_n^2 z_1 + \beta z_1^3)\right] + \left[\eta P + \eta z_2\frac{\partial P}{\partial z_2} + \frac{S}{4}\frac{\partial^2 P}{\partial z_2^2}\right] \tag{6.17}$$

where the term $\frac{\partial}{\partial z_2}(\eta z_2 P)$ has been expanded using the product rule (recalling that P is a function of z_2). The reader may observe that the equation of motion used in this analysis does not include the effects of friction while, in Chapter 3, it was shown that one must account for friction effects when modelling this device. Attempts to include Coulomb damping in a FPK analysis of the system proved to be difficult due to the presence of the Signum function and, as a result, an exact solution which dictates the effect of friction on the PDFs of the system could not be obtained. Although examples of the FPK equation being applied to systems with nonlinear damping can be found in the literature ([67, 68] for example) the author is unaware of an exact solution for a Coulomb damped oscillator. While not included in the FPK analysis, the issues associated with ignoring this nonlinearity are addressed in Chapter 7 via the method of equivalent linearisation.

6.3.2 Solution

This section details the solution of equation (6.17) - this was originally solved (in the context of energy harvesting) in [43] but is shown here for the sake of completeness. Assuming that the displacement and velocity probability densities are independent then:

$$P = P_1(z_1) \times P_2(z_2). \tag{6.18}$$

Writing $P_1(z_1)$ and $P_2(z_2)$ as P_1 and P_2 respectively then, after some manipulation the FPK equation of the system becomes:

$$0 = \left[-\frac{z_2}{P_1}\frac{\partial P_1}{\partial z_1} + \frac{1}{P_2}\frac{\partial P_2}{\partial z_2}(\omega_n^2 z_1 + \beta z_1^3) \right] + \left[\eta + \eta \frac{z_2}{P_2}\frac{\partial P_2}{\partial z_2} + \frac{S}{4P_2}\frac{\partial^2 P_2}{\partial z_2^2} \right]. \tag{6.19}$$

As observed in [69], P is a solution of equation (6.19) if it satisfies:

$$\left[-\frac{z_2}{P_1}\frac{\partial P_1}{\partial z_1} + \frac{1}{P_2}\frac{\partial P_2}{\partial z_2}(\omega_n^2 z_1 + \beta z_1^3) \right] = 0, \tag{6.20}$$

$$\left[\eta + \eta \frac{z_2}{P_2}\frac{\partial P_2}{\partial z_2} + \frac{S}{4P_2}\frac{\partial^2 p_2}{\partial z_2^2} \right] = 0. \tag{6.21}$$

Using the product rule, equation (6.21) can be written as:

$$\frac{d}{dz_2}\left(\eta P_2 z_2 + \frac{S}{4}\frac{dP_2}{dz_2} \right) = 0. \tag{6.22}$$

Integrating with respect to z_2:

$$\eta P_2 z_2 + \frac{S}{4}\frac{dP_2}{dz_2} = C, \tag{6.23}$$

where C is a constant. Knowing that P_2 is a probability density function then, as z_2 approaches infinity, P_2 and all of its derivatives will approach zero. Therefore, C must be equal to zero:

$$\eta P_2 z_2 + \frac{S}{4}\frac{dP_2}{dz_2} = 0. \tag{6.24}$$

After some manipulation and integrating with respect to z_2 one finds that:

$$P_2 = A_2 \exp\left(-\frac{2\eta z_2^2}{S} \right), \tag{6.25}$$

where, to satisfy the condition that the area under any PDF must be unity:

$$A_2^{-1} = \int_{-\infty}^{\infty} \exp\left(-\frac{2\eta z_2^2}{S} \right) dz_2. \tag{6.26}$$

Once P_2 is known it can be substituted back into equation (6.20) allowing one to write:

$$\frac{1}{P_1}\frac{dP_1}{dz_1} = -\frac{4\eta}{S}(\omega_n^2 z_1 + \beta z_1^3). \tag{6.27}$$

Integrating with respect to z_1 one finds that:

$$P_1 = A_1 \exp\left(-\frac{4\eta}{S}\left(\frac{\omega_n^2}{2}z_1^2 + \frac{\beta z_1^4}{4}\right)\right), \tag{6.28}$$

where, again, to satisfy the normalisation condition:

$$A_1^{-1} = \int_{-\infty}^{\infty} \exp\left(-\frac{4\eta}{S}\left(\frac{\omega_n^2}{2}z_1^2 + \frac{\beta z_1^4}{4}\right)\right) dz_1. \tag{6.29}$$

As a result, the stationary probability density function of the system is:

$$\begin{aligned} P = A_1 \exp&\left(-\frac{4(2\omega_n\zeta + \gamma/m)}{S}\left(\frac{\omega_n^2}{2}z_1^2 + \frac{\beta z_1^4}{4}\right)\right) \\ &\times A_2 \exp\left(-\frac{2(2\omega_n\zeta + \gamma/m)z_2^2}{S}\right). \end{aligned} \tag{6.30}$$

Upon studying equation (6.30) one can see that the joint PDF of the system has been expressed in the form:

$$P(z_1, z_2) = P_1(z_1)P_2(z_2), \tag{6.31}$$

where:

$$P_1(z_1) = A_1 \exp\left(-\frac{4(2\omega_n\zeta + \gamma/m)}{S}\left(\frac{\omega_n^2}{2}z_1^2 + \frac{\beta z_1^4}{4}\right)\right), \tag{6.32}$$

and

$$P_2(z_2) = A_2 \exp\left(-\frac{2(2\omega_n\zeta + \gamma/m)z_2^2}{S}\right). \tag{6.33}$$

By being able to separate the joint PDF into the form $P_1(z_1)P_2(z_2)$ one can conclude that the stationary relative displacement and relative velocity PDFs of the system are independent of each other. Consequently, changing a variable which is present in $P_1(z_1)$ but not in $P_2(z_2)$ (β in this case) allows one to alter the relative displacement PDF without affecting that of the relative velocity. This result is important with regards to some of the conclusions drawn in this chapter.

6.3.3 Benefits of Duffing-type nonlinearities

From equation (6.30) it can be seen that β has no influence on the relative velocity PDF and therefore cannot effect the power output of the device (as stated in [52] and confirming the Monte Carlo simulations of Chapter 5). However, the nonlinearity does affect the relative displacement PDF and can therefore be used to reduce the maximum displacement of the centre magnet without affecting the power output. In [14] the maximum possible amplitude of the centre magnet was identified as one of the limiting factors with respect to device performance and equation (6.30) shows that the nonlinear spring term is beneficial in this respect.

To quantify the effect of the nonlinearity, the variance of the relative displacement PDF can be found using:

$$\sigma_{z_1}^2 = \int_{-\infty}^{\infty} z_1^2 P_1(z_1) P_2(z_2) dz_1 dz_2, \tag{6.34}$$

the solution of which is beyond the scope of the present work. For the full solution to equation (6.34) the reader is directed towards reference [67] where the displacement variance is shown to be:

$$\sigma_{z_1}^2 = \sqrt{\frac{S}{8\beta(2\omega_n\zeta + \gamma/m)}} U\left(1, \frac{1}{\sqrt{2\rho}}\right) U\left(0, \frac{1}{\sqrt{2\rho}}\right)^{-1}, \tag{6.35}$$

where U is the parabolic cylindrical function (as defined in [70]) and

$$\rho = \frac{\beta S}{4\omega_n^4(2\omega_n\zeta + \gamma/m)}. \tag{6.36}$$

From a design perspective, if the parameters of the device are known then equation (6.35) can be used to estimate the maximum relative displacement of the centre magnet to within a desired level of confidence for different levels of nonlinearity. Defining the maximum relative displacement of the centre magnet as its value three standard deviations from the mean, Figure 6.2 shows how the maximum amplitude decreases as the nonlinear spring term is increased. Following this, Monte-Carlo simulations were run to validate the results according to equation (6.35). This is also shown in Figure 6.2. It should be noted that, by measuring the relative displacement three standard deviations from the mean one is estimating the maximum possible relative displacement to within a 99.7 % confidence interval.

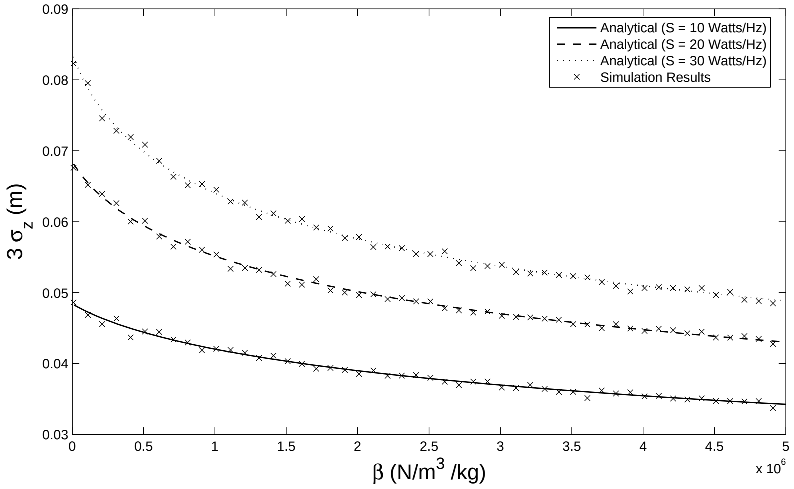

Figure 6.2: Variation of maximum centre magnet relative displacement amplitude with β, estimated to within a 99.7 % confidence interval where $m = 0.02$ kg, $\alpha = 0.2$ Henry/m, $R_L = 0.5$ Ohms, $R_C = 0.5$ Ohms, $\zeta = 0.05$ $\omega_n = 40$ rad/s and S=10 Watts/Hz. The line and crosses represent analytical (from equation (6.35)) and simulation results respectively.

6.3.4 Electrical optimisation

In Chapter 3 it was shown that the power delivered to a load resistor by an electromagnetic device is given by:

$$p_{load} = \frac{R_L \alpha^2 \dot{z}^2}{(R_L + R_C)^2} = \frac{R_L \dot{z}^2 \gamma}{(R_L + R_C)}, \tag{6.37}$$

which demonstrates that the power through the load resistor is proportional to the square of the relative velocity of the centre magnet of the device. From the FPK solution obtained earlier in the chapter (equation (6.30)), the expected value of relative velocity squared was be found to be:

$$E[z_2^2] = \int_{-\infty}^{\infty} z_2^2 A_2^{-1} \exp\left(-\frac{z_2^2\,(4\zeta\omega_n + 2\gamma/m)}{S}\right) dz_2 = \frac{S}{2(4\zeta\omega_n + 2\gamma/m)}. \tag{6.38}$$

Substituting into equation (6.37), the expected power across the load resistor can be written as:

$$E[p_{load}] = \frac{SR_L\alpha^2}{2(4\zeta\omega_n + 2\gamma/m)(R_L + R_C)^2}. \tag{6.39}$$

With the aim of finding the optimum value of load resistance, equation (6.39) was differentiated with respect to R_L and set equal to zero. By setting:

$$E[p_{load}] = \frac{f(R_L)}{g(R_L)} = 0, \tag{6.40}$$

then, using the quotient rule:

$$\frac{dE[p_{load}]}{dR_L} = g(R_L)\frac{df(R_L)}{dR_L} - f(R_L)\frac{dg(R_L)}{dR_L}. \tag{6.41}$$

By assigning

$$f(R_L) = SR_L\alpha^2, \tag{6.42}$$

and

$$g(R_L) = 2(4\zeta\omega_n + 2\gamma/m)(R_L + R_C)^2, \tag{6.43}$$

one finds that:

$$\begin{aligned}\frac{dE[p_{load}]}{dR_L} &= \left(8\zeta\omega_n(R_L + R_C)^2 + \frac{4\gamma(R_L + R_C)^2}{m}\right) S\alpha^2 \\ &-SR_L\alpha^2\left(16\zeta\omega_n + \frac{8\gamma}{m}\right)(R_L + R_C) = 0.\end{aligned} \tag{6.44}$$

After manipulation, the optimum load resistance ($R_{L(opt)}$) can be expressed as a quadratic:

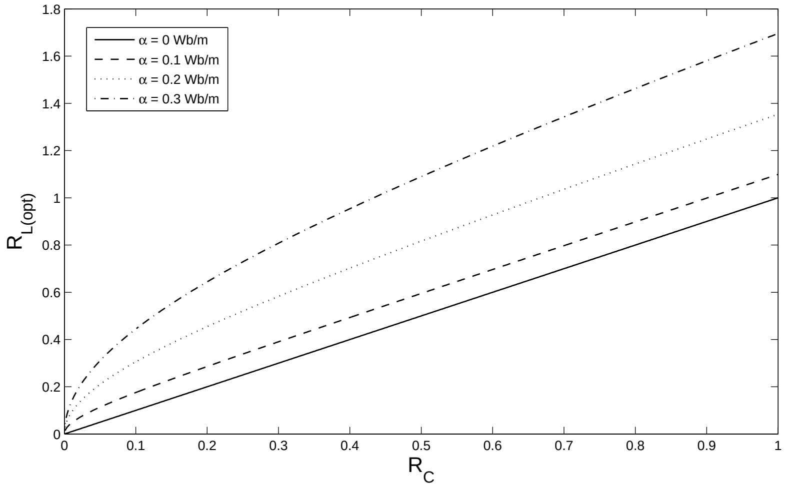

Figure 6.3: Variation of optimum load resistance with coil resistance for different values of α with $m = 0.02458$, $k = 56.2$, $k_3 = 86579$ and $c = 0.048$

$$(-2\zeta\omega_n m)R^2_{L(opt)} + (2\zeta\omega_n m R^2_C + \alpha^2 R_C) = 0, \tag{6.45}$$

whose solution is easily obtained with the formula:

$$R_{L(opt)} = \pm\frac{\sqrt{(2\zeta\omega_n R_C m)^2 + 2\zeta\omega_n R_C m\alpha^2}}{2\zeta\omega_n m}, \tag{6.46}$$

where the (unfeasible) negative values of load resistance are neglected. Upon studying equation (6.46) one can see that if $\alpha = 0$ then the optimum amount of power will be extracted when $R_L = R_C$. This is expected as it follows the fundamental principle of impedance matching [71]. However, when $\alpha \neq 0$ then the optimum load resistance is not equal to the coil resistance - this is illustrated by Figure 6.3.

Physically, this means that if the variation of magnetic flux with relative displacement is large then it will increase the value of optimum load resistance required. This may prove beneficial in situations where it is difficult to achieve a load resistance low enough to match that of the coil.

Experimental validation

The purpose of the work detailed here is to show an experimental validation of the findings detailed by equation (6.46). The following tests were undertaken using the test rig detailed in Chapter 3 (Figure 3.12 specifically).

Exciting the energy harvester with white noise over the relevant bandwidth of the device the voltage output was recorded for different values of load resistance. The experimental results were then compared with that obtained via Monte-Carlo simulations.

With a coil resistance of 0.48 Ohms, the optimum load resistance predicted by equation (6.46) was found to be 0.67 Ohms. As a result, it was necessary to vary the load resistance by as little as 0.1 Ohms between tests - this was achieved using combinations of discrete resistors, each with a resistance of 0.1 Ohms. For larger changes in resistance a decade box was found to be sufficiently accurate.

In section 6.3.1 it was briefly mentioned that the Coulomb damping model identified in Chapter 3 was not used in the FPK analysis. To give an idea of the effects of friction on the ability of the Monte-Carlo simulations to replicate the experimental data, the output of the device was compared with two different simulations - one including and one neglecting the effects of friction. These comparisons are shown in Figure 6.4 where, as expected, the neglecting of friction effects leads to a poor match between experiment and model while, with friction included, the simulation matches the experiment well. The optimum load resistance in both simulations as well as the experimental test was larger than that of the coil resistance thus confirming the findings shown in section 6.3.4.

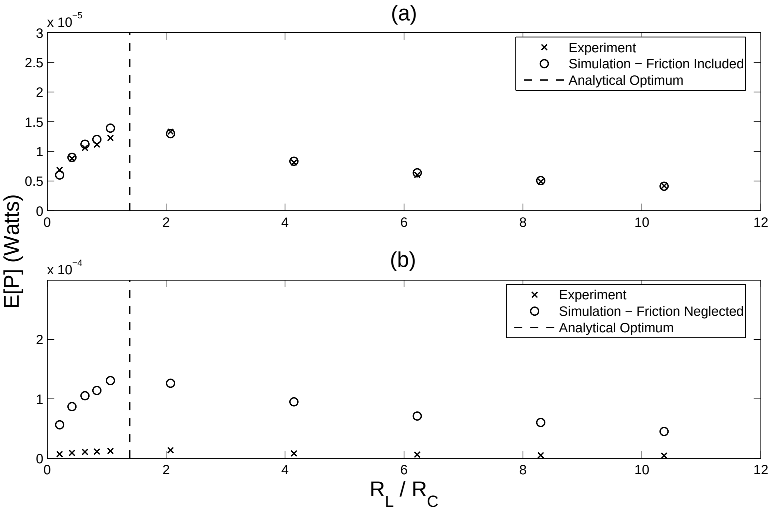

Figure 6.4: Expected power output for different values of load resistance where crosses represent experimentally identified values, dots and circles represent simulation results and the dashed lines represent the analytical optimum load resistance. Plots (a) and (b) represent simulation results where $F_d = 0.025$ and $F_d = 0$ Newtons respectively.

6.4 Summary

In this chapter, the response of the Mann and Sims energy harvester to random excitations was analysed via the FPK equation. Using this approach an analytical expression was developed which proved much more informative than the Monte Carlo simulations shown in the previous chapter. The first important result to note is that, when excited by Gaussian white noise, the addition of the nonlinear spring term has no benefits with regards to the power output of the device. From an energy harvesting point of view this is a disappointing result as, when the device was originally proposed in [30], it was hoped that the addition of the nonlinearity would improve the bandwidth over which it could harvest energy (and therefore make it more suitable to harvest energy from Gaussian white noise). However, as shown in this chapter, the fact that the nonlinearity has *no effect at all* on the power output of the device is beneficial as it can therefore be used to reduce the size of the device without effecting its performance. This is important as one of the main motivations behind energy harvesting research is the idea that the development of small devices will allow them to be placed in a large variety of environments.

Finally, important findings were found with regards to the maximisation of electrical power being delivered to a load resistor. It was shown that, contrary to the principle of impedance matching, the optimum power output will not necessarily be realised if one tunes the load resistance such that it equal to the coil resistance of the device. In fact, the optimum load resistance is also a function of the magnetic flux present in the system: a result which was also validated experimentally.

The effects of friction were ignored throughout this chapter as the inclusion of Coulomb damping made the corresponding FPK equation very difficult to solve. However, the following chapter details how the effects of Coulomb damping on the response of the randomly excited energy harvester can be approximated using the method of equivalent linearisation.

Chapter 7

RANDOM EXCITATIONS: EQUIVALENT LINEARISATION

7.1 Introduction

In the previous chapter the FPK equation for a system with a nonlinear stiffness term subjected to a Gaussian white noise excitation was derived. Unfortunately, being a second order partial differential equation, closed form solutions of the FPK equation are often very difficult, if not impossible to obtain. This is often the case when nonlinear damping terms (such as Coulomb damping) are included[1]. In such a case, one may consider using the method of equivalent linerisation to derive an expression which approximates the effect of the nonlinear damping term on the system. This chapter begins by discussing the theoretical background of this method.

7.1.1 Theoretical Background

The technique of equivalent linearisation is concerned with the development of a linear system which is able to match the behavior of a nonlinear system as closely as possible. For example, consider the system:

---

[1] Examples of systems with known solutions to their corresponding FPK equations are given in[67] and [68].

$$m\ddot{z} + f(\dot{z}) + kz = mw(t), \tag{7.1}$$

where $f(\dot{z})$ is some nonlinear function of $\dot{z}$ and $w(t)$ is zero mean Gaussian white noise with:

$$\phi_{ww}(\tau) = \frac{S}{2}\delta(\tau). \tag{7.2}$$

Assuming that the PDF of the system could not be obtained using the FPK equation then equivalent linearisation can be used to develop a linear system of the form:

$$m\ddot{z} + c_{eq}\dot{z} + kz = mw(t), \tag{7.3}$$

where the equivalent damping level (c_{eq}) is chosen such that the behavior of the linear system matches that of the nonlinear (equation (7.3)) as closely as possible. In other words, one needs to minimise quantity:

$$J = E[(f(\dot{z}) - c_{eq}\dot{z})^2], \tag{7.4}$$

which expands to:

$$J = E[f(\dot{z})^2 - 2c_{eq}\dot{z}f(\dot{z}) + c_{eq}^2\dot{z}^2]. \tag{7.5}$$

This minimum value can be found by differentiating J with respect to c_{eq} and setting it equal to zero:

$$\frac{\partial J}{\partial c_{eq}} = E[-2\dot{z}f(\dot{z}) + 2c_{eq}\dot{z}^2] = 0, \tag{7.6}$$

which leads to:

$$c_{eq}E[\dot{z}^2] = E[\dot{z}f(\dot{z})]. \tag{7.7}$$

Assuming that $f(\dot{z})$ can be separated into linear and nonlinear components:

$$f(\dot{z}) = c\dot{z} + \Phi(\dot{z}), \tag{7.8}$$

(where $\Phi(\dot{z})$ is the nonlinear function) allows one to write:

$$\begin{aligned} c_{eq}E[\dot{z}^2] &= E[(c\dot{z}+\Phi(\dot{z}))\dot{z}] \\ &= cE[\dot{z}^2]+E[\Phi(\dot{z})\dot{z}], \end{aligned} \tag{7.9}$$

therefore:

$$c_{eq} = c + \frac{E[\Phi(\dot{z})\dot{z}]}{E[\dot{z}^2]}. \tag{7.10}$$

Upon studying equation (7.10) one can see that the expression $E[\Phi(\dot{z})\dot{z}]$ needs to be evaluated if one is to find c_{eq}. Expanding using the definition of the expected value gives:

$$E[\Phi(\dot{z})\dot{z}] = \int_{-\infty}^{\infty} P(\dot{z})(\Phi(\dot{z})\dot{z})d\dot{z}, \tag{7.11}$$

which cannot be solved as the PDF of the nonlinear system ($P(\dot{z})$) is not known. To overcome this issue, the velocity PDF of the nonlinear system is approximated with the velocity PDF of the equivalent linear system:

$$P(\dot{z}) \approx P_{eq}(\dot{z}) = \frac{1}{\sqrt{2\pi}\sigma_{\dot{z}eq}} \exp\left(-\frac{2\dot{z}^2 c_{eq}}{Sm}\right), \tag{7.12}$$

(the velocity PDF of a linear SDOF system is derived in Appendix B.4). Additionally, recalling that $E[\dot{z}^2] \approx \sigma^2_{\dot{z}eq}$ (so long as $E[\dot{z}]=0$) then equation (7.10) can be written:

$$c_{eq} = c + \frac{1}{\sqrt{2\pi}\sigma^3_{\dot{z}eq}} \int_{-\infty}^{\infty} \exp\left(-\frac{2\dot{z}^2 c_{eq}}{Sm}\right) \Phi(\dot{z})\dot{z}d\dot{z}. \tag{7.13}$$

As a result, equation (7.13) can be used to find the value of c_{eq} that is required to approximate the nonlinear system as closely as possible. Similarly, if one were to repeat a similar process for a system with a nonlinear spring term:

$$m\ddot{z} + c\dot{z} + kz + \Phi(z) = mw(t), \tag{7.14}$$

the stiffness (k_{eq}) of the equivalent linear system is given by:

$$k_{eq} = k + \frac{1}{\sqrt{2\pi}\sigma^3_{z(eq)}} \int_{-\infty}^{\infty} \exp\left(-\frac{2k_{eq}z^2c}{Sm^2}\right) \Phi(z) z dz. \tag{7.15}$$

With all of the appropriate tools defined, it is now possible to proceed with an investigation into the response of the Mann and Sims energy harvesting device to random excitations through equivalent linearisation.

7.2 Analysis via Equivalent Linerisation

The aim of the work shown here was to develop simple expressions which approximated the effects of Duffing-type nonlinearities on displacement variance as well as the effects of friction (Coulomb damping specifically) on the power output of the randomly excited Mann and Sims energy harvester.

7.2.1 Duffing-type nonlinearities

In Chapter 6 it was shown that Duffing-type nonlinearities (of the hardening variety) can be used to reduce the rattle space of the energy harvester without affecting power output (when under a Gaussian white noise excitation). Although equation (6.35) of the previous chapter was able to demonstrate the effect of Duffing-type nonlinearities on the relative displacement variance of the device it is not an equation which can be easily interpreted. Consequently, the purpose of this section was to use the technique of equivalent linearisation to develop an expression for the relative displacement variance which, although less accurate, is easier to understand and interpret than equation (6.35).

Recalling the equation of motion of the device (neglecting friction effects):

$$\ddot{z} + \frac{\theta}{m}\dot{z} + \frac{k}{m}z + \frac{k_3}{m}z^3 + = -w(t), \tag{7.16}$$

where for simplicity θ represents a combination of electrical and parasitic damping:

$$\theta = c + \frac{\alpha^2}{R_L + R_C} \tag{7.17}$$

then the purpose of the following analysis is to find a system of the form:

$$\ddot{z} + \frac{\theta}{m}\dot{z} + \frac{k_{eq}}{m}z = -w(t), \tag{7.18}$$

which can replicate the response of the nonlinear system as accurately as possible. As was demonstrated in section 7.1.1, the equivalent linear stiffness is given by:

$$k_{eq} = k + \frac{E[\Phi(z)z]}{E[z^2]}, \tag{7.19}$$

where $\Phi(z)$ is the nonlinear stiffness function to be analysed and

$$E[\Phi(z)z] = \int_{-\infty}^{\infty} P(z)(\Phi(z)z)dz. \tag{7.20}$$

As stated previously, the PDF of the nonlinear system ($P(z)$) is approximated by that of a linear system, so that one can make use of the fact that a linear system excited with a zero mean Gaussian excitation will have a zero mean Gaussian response [34]. Using the knowledge that the PDF of the linear equivalent system is Gaussian allows one to write:

$$P(z)_{eq} = \frac{1}{\sqrt{2\pi}\sigma_{z(eq)}} \exp\left(-\frac{2k_{eq}z^2\theta}{Sm^2}\right), \tag{7.21}$$

such that, after setting $\Phi(z) = k_3 z^3$, equation (7.20) becomes:

$$k_{eq} = k + \frac{k_3}{\sqrt{2\pi}\sigma_{z(eq)}^3} \int_{-\infty}^{\infty} \exp\left(-\frac{2k_{eq}z^2\theta}{Sm^2}\right) z^4 dz. \tag{7.22}$$

The relative displacement variance of the equivalent linear system is found from:

$$\sigma_{z(eq)}^2 = \int_{-\infty}^{\infty} \exp\left(-\frac{2k_{eq}z^2\theta}{Sm^2}\right) z^2 dz, \tag{7.23}$$

which leads to:

$$\sigma_{z(eq)}^2 = \frac{Sm^2}{4k_{eq}\theta} \tag{7.24}$$

(proved in Appendix B.4). Solving equation (7.22) (the solution to integrals of

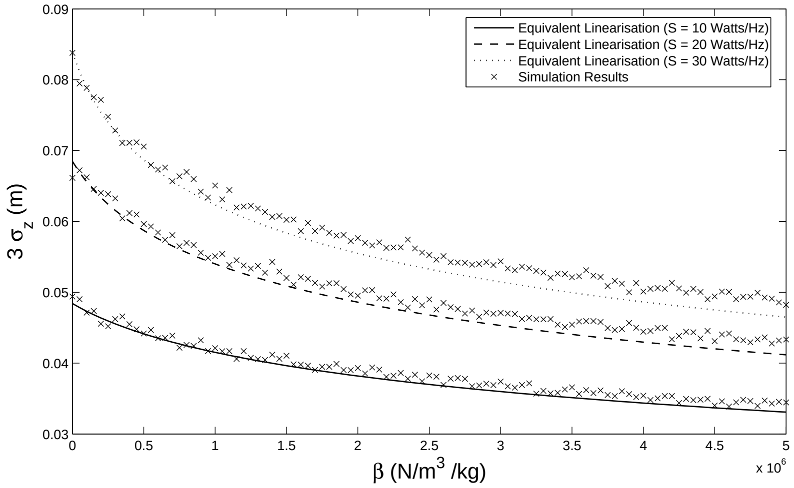

Figure 7.1: Comparison of $3\sigma_z$ as β is varied where $\omega_n = 40$ rad/s , $m = 0.02$ kg, $\theta = 0.12$ Ns/m. Solid and dashed lines represent results according to equivalent linearisation where crosses and dots represent results according to Monte-Carlo simulations and equivalent linearisation respectively. These are the same parameter values as was used in Figure 6.2.

this type is shown in [34]) and neglecting negative values of k_{eq} one finds that the equivalent linear stiffness is given by:

$$k_{eq} = \frac{1}{2}\frac{\theta k + \sqrt{\theta^2 k^2 + 3k_3 S m^2 \theta}}{\theta}. \tag{7.25}$$

Having found the equivalent stiffness, equation (7.24) was used to find the variance of the linear equivalent system. Figure 7.1 shows the relative displacement variance according to equation (7.24) compared with that obtained using Monte-Carlo simulations (note that, as in the previous chapter, $\beta = k_3/m$). It can be seen that the equivalent linearisation technique can provide a good estimate of the relative displacement variance as k_3 is altered. It is interesting to note that the quality of the match between the equivalent linear model and the simulated results decreases as the amplitude of the excitation is increased - this is because the nonlinear spring term is having a greater effect on the system dynamics.

7.2.2 Coulomb damping

The aim of this section is create an equivalent linear system which allows one to approximate the effect of friction on the power output of the randomly excited device. Having selected the Coulomb damping friction model (as described in Chapter 3) then the equation of motion to be approximated is:

$$m\ddot{z} + F_c \operatorname{sgn}(\dot{z}) + cz + kz + k_3 z^3 = -mw(t) \tag{7.26}$$

where $w(t)$ is a zero mean Gaussian white noise excitation with the same properties as previously stated in this chapter (equation 7.2). As has already been shown, when excited by Gaussian white noise, the nonlinear spring term (k_3) has no effect on power output of the device and can therefore be neglected in the following analysis. However, the studies shown previously did not include friction. In the present study it is assumed that the nonlinear stiffness still has no effect on power output even when friction is present (this will be confirmed later in the current chapter). The equation of motion then is written as:

$$m\ddot{z} + F_c \operatorname{sgn}(\dot{z}) + c\dot{z} + kz = -mw(t). \tag{7.27}$$

In a similar manner to the previous section, the aim is to find an equivalent linear system of the form:

$$m\ddot{z} + c_{eq}\dot{z} + kz = -mw(t) \tag{7.28}$$

where c_{eq} is chosen such that the linear response is able to match the response of the nonlinear system as closely as possible. In this case, the equivalent damping term in equation (7.28) is given by the following integral:

$$c_{eq} = c + \frac{F_c}{\sqrt{2\pi}\sigma_{\dot{z}eq}^3} \int_{-\infty}^{\infty} \exp\left(-\frac{\dot{z}^2}{2\sigma_{\dot{z}eq}}\right) \dot{z} \operatorname{sgn}(\dot{z}) d\dot{z} \tag{7.29}$$

where $\sigma_{\dot{z}eq}^2$ is the variance of the linear equivalent system's velocity probability density function which is known to be:

$$\sigma^2_{\dot{z}eq} = \frac{Sm}{4c_{eq}}, \tag{7.30}$$

(proved in Appendix B.4). By writing:

$$\operatorname{sgn}(\dot{z}) = \frac{|\dot{z}|}{\dot{z}} \tag{7.31}$$

one obtains:

$$\begin{aligned} c_{eq} &= c + \frac{F_c}{\sqrt{2\pi}\sigma^3_{\dot{z}eq}} \int_{-\infty}^{\infty} \exp\left(-\frac{\dot{z}^2}{2\sigma_{\dot{z}eq}}\right) |\dot{z}| d\dot{z} \\ &= c + \frac{F_c}{\sqrt{2\pi}\sigma^3_{\dot{z}eq}} 2 \int_0^{\infty} \exp\left(-\frac{\dot{z}^2}{2\sigma_{\dot{z}eq}}\right) \dot{z} d\dot{z}. \end{aligned} \tag{7.32}$$

Recalling that,

$$\frac{d}{d\dot{z}}\left(\exp\left(-\frac{\dot{z}^2}{2\sigma_{\dot{z}eq}}\right)\right) = -\frac{\dot{z}}{\sigma^2_{\dot{z}eq}} \exp\left(-\frac{\dot{z}^2}{2\sigma_{\dot{z}eq}}\right) \tag{7.33}$$

then,

$$-\sigma^2_{\dot{z}eq} \exp\left(-\frac{\dot{z}^2}{2\sigma_{\dot{z}eq}}\right) = \int \exp\left(-\frac{\dot{z}^2}{2\sigma_{\dot{z}eq}}\right) \dot{z} d\dot{z}. \tag{7.34}$$

Substituting this result into equation (7.32) yields:

$$c_{eq} = c + \frac{F_c}{\sqrt{2\pi}\sigma^3_{\dot{z}eq}} (-\sigma^2_{\dot{z}eq}) \left[\exp\left(-\frac{\dot{z}^2}{2\sigma_{\dot{z}eq}}\right)\right]_0^{\infty} \tag{7.35}$$

therefore:

$$c_{eq} = c + \frac{F_c}{\sqrt{2\pi}\sigma_{\dot{z}eq}}. \tag{7.36}$$

Using the equivalent linear velocity variance (equation (7.30)) this may be written:

$$c_{eq} = c + \frac{4F_c}{\sqrt{2\pi}} \sqrt{\frac{c_{eq}}{Sm}}, \tag{7.37}$$

therefore:

$$(c_{eq} - c)^2 = \left(\frac{4F_c}{\sqrt{2\pi}}\right)^2 \frac{c_{eq}}{Sm}, \tag{7.38}$$

which, after a little manipulation, can be written:

$$c_{eq}^2 + c_{eq}\left[-2c - \frac{8F_c^2}{\pi Sm}\right] + c^2 = 0. \tag{7.39}$$

After solving with the quadratic formula and neglecting negative values of damping as being unphysical, the equivalent damping term is given by:

$$c_{eq} = c + \frac{4F_c^2}{\pi Sm} + \frac{1}{2}\sqrt{\left(-2c - \frac{8F_c^2}{\pi Sm}\right) - 4c^2}. \tag{7.40}$$

The expected power delivered to the electrical domain is given by:

$$E[p_e] = E[c_e\dot{z}^2] = c_e E[\dot{z}^2] \tag{7.41}$$

which, as $E[\dot{z}] = 0$, can be written:

$$E[p_e] = c_e\sigma_{\dot{z}}^2 = c_e\frac{Sm}{4c_{eq}} \tag{7.42}$$

where c_{eq} is given by equation (7.40). Consequently, through equivalent linearisation the effect of friction on the power output of the randomly excited device can be approximated.

Figure 7.2 shows a comparison between the equivalent linearisation approach and the results of numerical simulations of equation (7.26) for 3 different values of power spectral density height (S) for the cases where (a) $k_3 = 0$ and (b) $k_3 = 500000$ N/m^3. In all of the cases shown it is clear that the equivalent linearisation approach has accurately modelled the effect of friction on power delivered to the electrical domain. What is perhaps most interesting about this result is that the ability of the equivalent linear system to replicate the response of the digital simulation does not appear to be affected by the presence of the Duffing-type nonlinearity (k_3). With regards to energy harvester design this is a useful result as it demonstrates that the intentionally introduced Duffing-type nonlinearity is not interacting with the unavoidable friction nonlinearity in a way which can be detrimental to the device

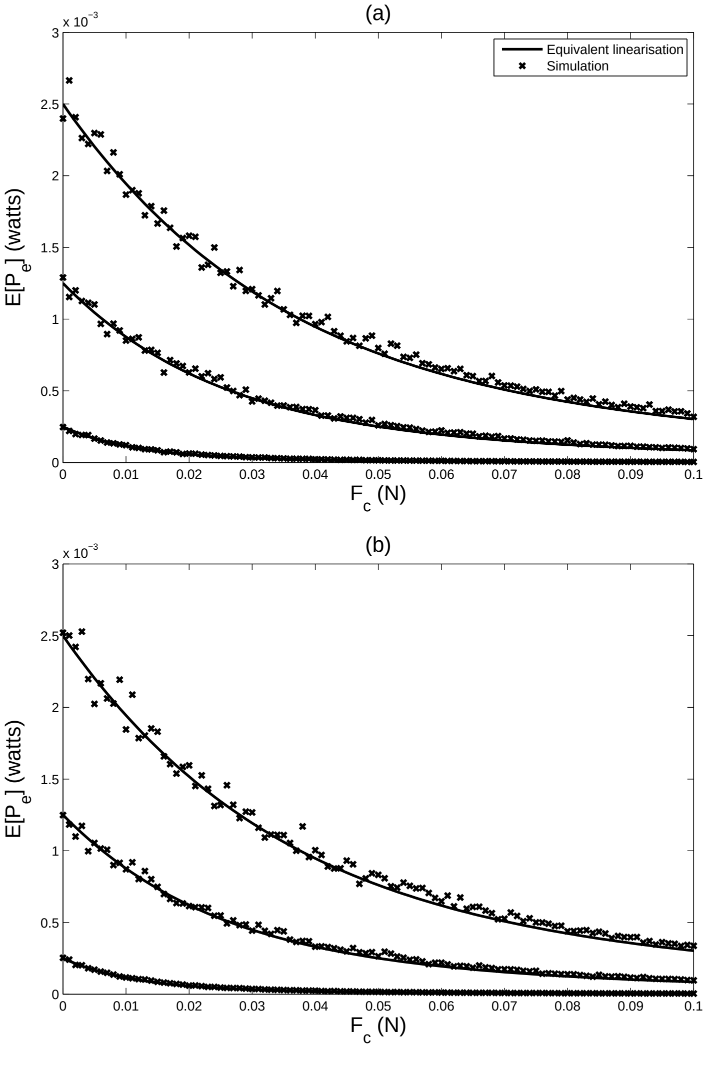

Figure 7.2: The effect of Coulomb damping on expected power output where $c_m = c_e = 0.1$ Ns/m and, from top to bottom, $S = 1$, 0.5 and 0.1 (m/s^2)/Hz respectively. Figures (a) and (b) represent cases where $k_3 = 0$ and 500000 N/m^3 respectively while all other parameters are the same as those shown in Table 3.2 (Coulomb model). Crosses and solid lines represent results according to simulation and equivalent linearisation respectively.

performance. Consequently, one can conclude that the benefits one can achieve via the addition of the hardening-spring nonlinearity with regards to rattle space are still possible despite the presence of friction.

7.3 Summary

While it is difficult to include friction effects in an FPK analysis of the energy harvester in question the work in this chapter shows that one can accurately approximate the effects of friction on the response of the randomly excited device using equivalent linearisation methods. This is important because, as shown throughout this work, the response of the device is sensitive to the effects of friction. Additionally, a relatively simple expression approximating the benefits of Duffing-type nonlinearities with regards to device rattle-space was derived. Crucially, it was shown that the afore mentioned benefits of Duffing-type nonlinearities can be employed despite the presence of friction in the device.

Chapter 8

AMBIENT EXCITATIONS

8.1 Introduction

Before discussing the content of the present chapter it is worth briefly recalling the main goals of this thesis. Essentially, the main aim of this work is to investigate whether dynamic nonlinearities can be used to improve the performance of devices which are designed to harvest electrical energy from ambient vibrations. The understanding that most ambient vibration sources are stochastic has led to investigations into how energy harvesters respond to random excitations. This was very much the focus of the previous chapters in which the case of a Gaussian white noise excitation was examined - a scenario which has also been considered by many other authors (as discussed in Chapter 2). With this in mind, the main question that is addressed in the present chapter is: how well can energy harvesting solutions that are developed using Gaussian white noise excitations be extended to real energy harvesting scenarios?

Consequently, in this chapter, acceleration data obtained from the walking motion of 3 individuals and the vibrations of the Humber bridge are used as inputs to digital simulations of different types of nonlinear energy harvester. As well as investigating the nonlinear solutions which were developed in this thesis (Chapter 6), attention is also focused on those which have been developed by other authors.

The first part of this chapter focuses on the response of a monostable nonlinear[1] energy harvesting device. Of specific interest is the work shown in Chapter 6 in which the Fokker-Planck-Kolmogorov (FPK) equation was used to show that, when excited by Gaussian white noise, Duffing-type nonlinearities can be used to reduce the stroke of an energy harvesting device without affecting its power output. The second part of this chapter focuses on the response of the bistable nonlinear device - specifically the idea that the useful bandwidth of such a device can be extended by having the system 'escape' from its potential energy well into a high energy solution [46, 47, 51] or by activating interwell dynamics [45].

At this point the author would like to thank Dr Evangelos Papatheou from the Centre for Engineering Dynamics at the University of Liverpool and Professor James M.W. Brownjohn from the Civil and Structural Engineering Department at the University of Sheffield for providing acceleration data from walking motion and bridge vibrations respectively. While the data was not directly acquired by the author all of the signal processing shown henceforth in the present chapter can be considered the author's own work.

8.2 Model

Before proceeding with the analysis it is worth restating the equation of motion of the Mann and Sims energy harvester:

$$m\ddot{z} + (c_m + c_e)\dot{z} + kz + k_3 z^3 = -m y_a(t) \tag{8.1}$$

where z is the relative displacement between the magnet and the shell of the device and y_a is now used to represent the acceleration of the ambient excitation. While in Chapter 3 it was found that the inclusion of friction improved model performance, the aim of this investigation was to examine the proposed benefits of Duffing-type nonlinearities specifically and so, for the sake of simplicity, friction effects are ignored throughout.

---

[1] Throughout this chapter the term nonlinear will be used to refer to Duffing-type nonlinearities specifically.

Again, the power delivered to the electrical domain is defined as:

$$p = c_e \dot{z}^2. \tag{8.2}$$

8.3 Ambient vibration sources

8.3.1 Walking motion

The harvesting of energy from human walking motion is often cited as one of the potential applications of energy harvesters. For example, in [7] it was proposed that small scale energy harvesters could be used to form part of a wearable network of autonomous sensor systems which monitor the health and comfort of an individual. In [72] an energy harvesting backpack was developed which, it was suggested, could give freedom to disaster-relief workers who would otherwise need to carry heavy battery packs. This led to an investigation into the effect that such a backpack would have on the human gait [73]. In [74], an investigation into the feasibility of harvesting energy from walking motion using piezoelectric film-bending beams placed inside shoes was examined. Furthermore, in reference [75] an electromagnetic device was detailed which was designed to supply energy to body worn sensors. With these potential uses in mind it was decided to investigate the feasibility of applying nonlinear energy harvesting solutions to the scenario of harvesting energy from walking motion.

To acquire a time history of the acceleration due to walking motion, a DC accelerometer was placed on several participants who were then asked to walk on a tread mill. This data was gathered as part of the work shown in [73, 76]. Consequently, for information about the test procedure the reader is directed towards [73].

In this case the data from 3 participants walking at 3.6 km/h was analysed. Once 60 seconds of acceleration data had been gathered from each participant, the data was passed through a low pass filter to remove measurement noise (see Figure 8.1).

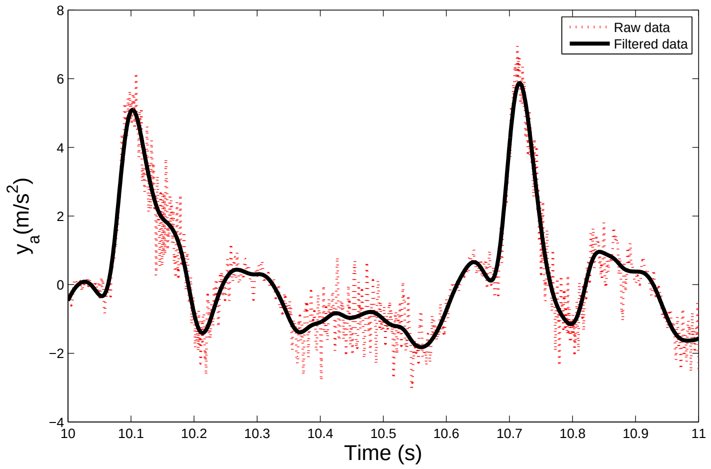

Figure 8.1: Comparison of raw and filtered acceleration time histories where the dotted and solid lines represent the raw and filtered data respectively.

The frequency content and histograms of the resulting excitation signals are shown in Figures 8.2 and 8.3. With regards to Figure 8.2 it is interesting to note that, even though all the participants were walking at the same speed, the frequency content of the signals are dependent on the individual. Additionally, the spectrum contains definite ‘spikes’ where power is concentrated while the Gaussian white noise studied in the previous chapters has equal power in each frequency. Additionally, upon studying Figure 8.3 (a), it is clear that the acceleration time history does not have a Gaussian distribution (confirmed by the quantile plot in Figure 8.3 (b)).

The response of a linear device to such an excitation was analysed by using the walking excitation as an input to equation (8.1) (with $k_3 = 0$) and solving using numerical integration techniques (4th order Runge-Kutta). Figure 8.4 shows a near periodic relative displacement response (z) has been induced from the walking motion of all three participants.

8.3.2 Bridge motion

Alleviating the need for battery replacement, the successful implementation of energy harvesters would offer the opportunity for low powered sensors to be placed in hostile or difficult to access environments. Clearly this will be advantageous in

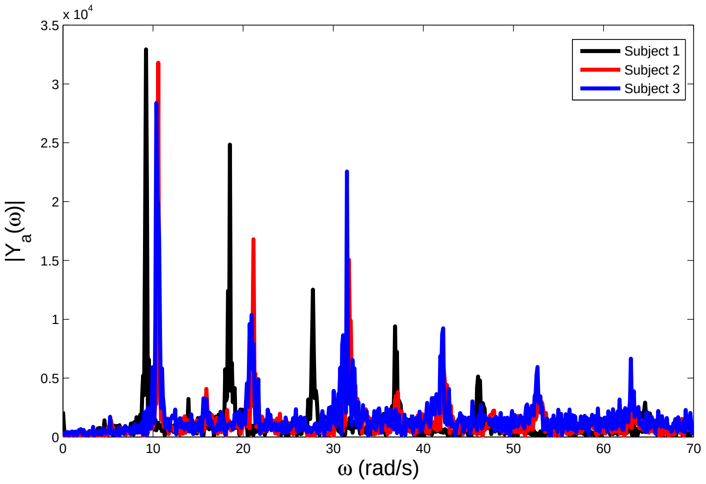

Figure 8.2: Frequency content of acceleration due to walking motion for subjects 1 2 and 3.

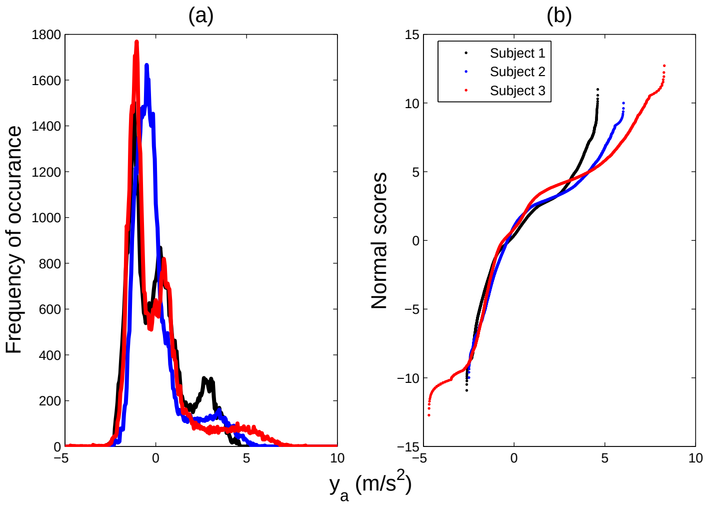

Figure 8.3: (a) Histogram and (b) quantile plot of acceleration due to walking motion for subjects 1 2 and 3.

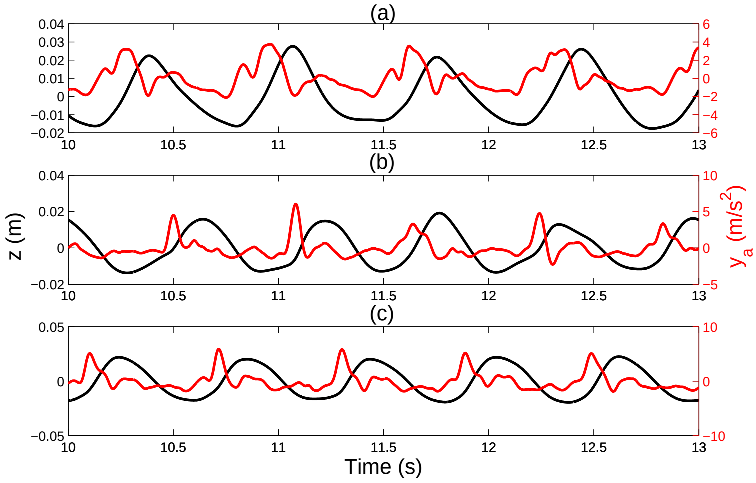

Figure 8.4: Displacement response of model (black) and acceleration due to walking motion (red) for (a) subject 1, (b) subject 2 and (c) subject 3 where $c_m = c_e = 0.08$ Ns/m , $m = 0.024$ kg and $k_3 = 0$ N/m^3.

the scenario where one is using a large network of sensors to monitor the structural health of a bridge. As a result, bridge vibrations are the second excitation type to be analysed is this paper. The acceleration data used here was gathered from the central span of the Humber bridge, East Yorkshire, England, over a period of two hours.

As with the previous example, the acceleration data was passed through a low pass filter to remove measurement noise. Upon studying Figure 8.5 one can see that, although filtered, the signal still appears to be fairly noisy. This is confirmed when one considers the frequency content of the signal (as shown in Figure 8.6) where it is shown that, compared with the walking excitation, the power in the bridge excitation signal is dispersed over a greater range of frequencies. Upon consulting the quantile plot of data shown in Figure 8.7 (b), one can see that the bridge excitation is not Gaussian.

Again, using the excitation as an input to the digital model for equation (8.1), Figure 8.8 shows that a near periodic relative displacement response (z) is induced.

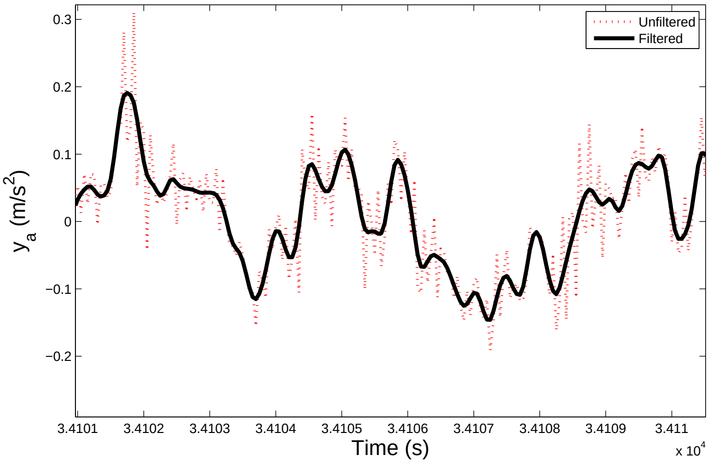

Figure 8.5: Comparison of raw and filtered acceleration time histories where the dotted and solid lines represent the raw and filtered data respectively.

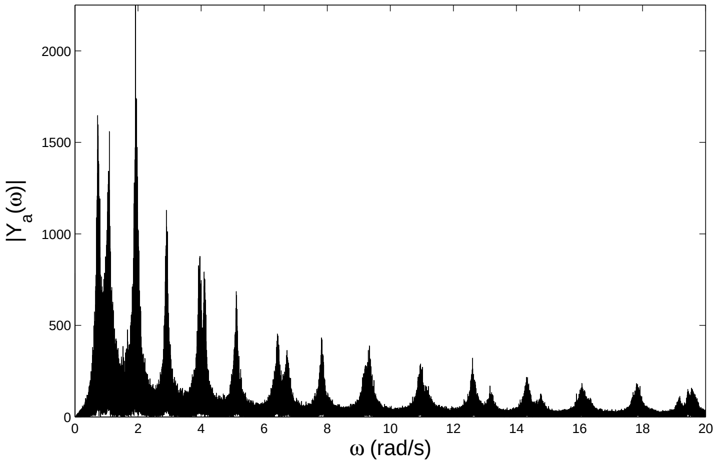

Figure 8.6: Frequency content of acceleration from bridge motion.

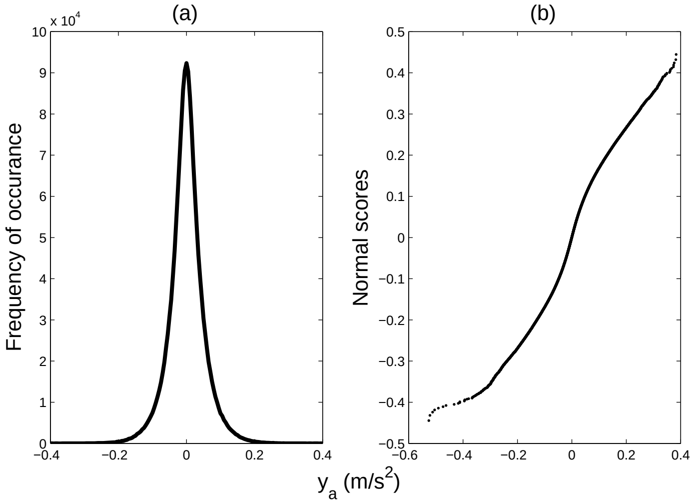

Figure 8.7: (a) Histogram and (b) quantile plot of acceleration due from bridge motion.

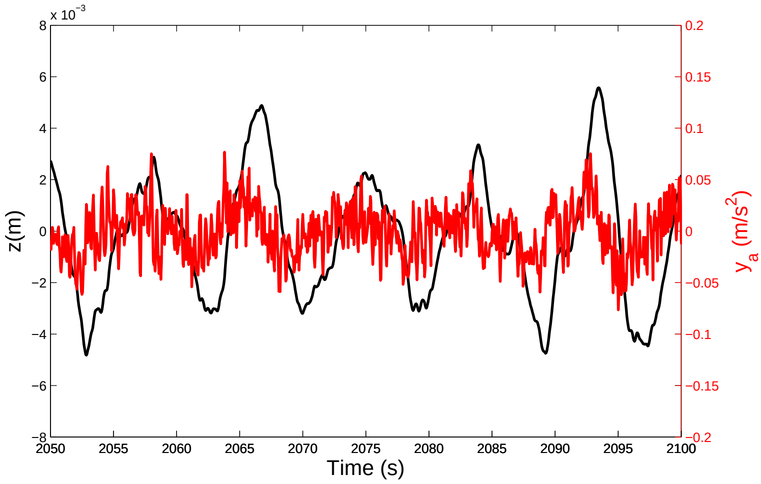

Figure 8.8: Displacement response of model (black) and acceleration due to bridge excitation (red) for $c_m = c_e = 0.08$ Ns/m , $m = 0.024$ kg and $k_3 = 0$ N/m^3.

Parameter	Value	Units
m	0.0236	kg
c_m	0.088	Ns/m
c_e	0.083	Ns/m

Table 8.1: Parameters of monostable nonlinear device.

8.4 Monostable nonlinear energy harvesting

This analysis begins by investigating the Mann and Sims device (which has been the main focus of this work thus far). The aim of this section was to investigate whether the benefits of Duffing-type nonlinearities that were identified in Chapter 6 can be extended to the human motion and bridge vibration scenarios. The device parameters were chosen to be similar to those identified in Chapter 3 as they can be considered close to what can be achieved practically - these are shown in Table 8.1.

Using the walking excitation data of subject 2 as an input to the digital model of the device, Figure 8.9 shows the variation of expected power delivered to the electrical domain (defined as $p = c_e\dot{z}^2$) and the displacement variance of the device for different values of linear and nonlinear stiffness (k and k_3). With regards to the response of the linear device (solid lines on Figure 8.9) the first thing to be noticed is that the device achieves maximum power output and, consequently, maximum displacement, when its natural frequency is tuned to the dominant frequency of excitation (a rather intuitive result). As k is increased one can see an increase in power output when the device is tuned to the second harmonic of the excitation ($k \approx 11$ N/m). With the nonlinear spring term set to 5000 N/m^3 (dashed lines on Figure 8.9) one observes that the optimum value of k (with regards to power output) has been reduced. This is a consequence of the ‘skewing’ effect that is caused by hardening spring nonlinearities - the nonlinear spring term has increased the resonant frequency of the device such that a lower value of linear stiffness is now required to tune the device to the dominant frequency of excitation. The key findings from these results are that, although the addition of the nonlinear stiffness term has reduced the displacement of the device, this reduced displacement has been accompanied by a reduction in the power output. This is contrary to the findings shown in Chapter 6, thus highlighting the potential difficulties involved with transferring findings developed under the assumption of a Gaussian white noise excitation to a real world energy

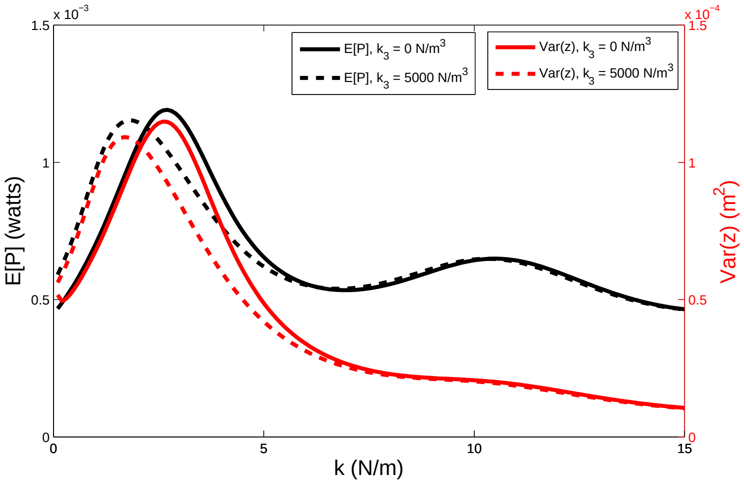

Figure 8.9: Response of device to excitation from subject 2 walking motion: the variation of displacement and power with linear stiffness where the solid and dashed lines represent cases where $k_3 = 0$ and 5000 N/m^3 respectively. All other parameters are as shown in Table 8.1.

harvesting scenario. Similar results to that shown in Figure 8.9 were found when the walking data from the other participants were used. The conclusions drawn from these results were also found to be independent of the damping levels used in each simulation.

The aim of the next phase of the analysis was to identify the effect of the nonlinear spring term on the response of the device when it is tuned such that its power output is maximised. Figure 8.10 shows the variation of expected power and displacement variance for different values of k_3 where, for every data point, k was chosen such the power output of the device was maximised. Consequently, the notation k_{opt} and p_{opt} is used to denote the optimum linear stiffness and resulting power output while $\text{Var}(z|p_{opt})$ represents the displacement variance of the displacement given that the device has been optimised with regards to power output. Clearly, any benefit with regards to device rattle space has come at the expense of power output.

8.4.1 Response to bridge motion

In the previous section it was shown that, for the case of walking motion, it is difficult to realise the benefits of Duffing-type nonlinearities (as identified in Chapter 6) without harming the power output of the device. The aim of the work in this sec-

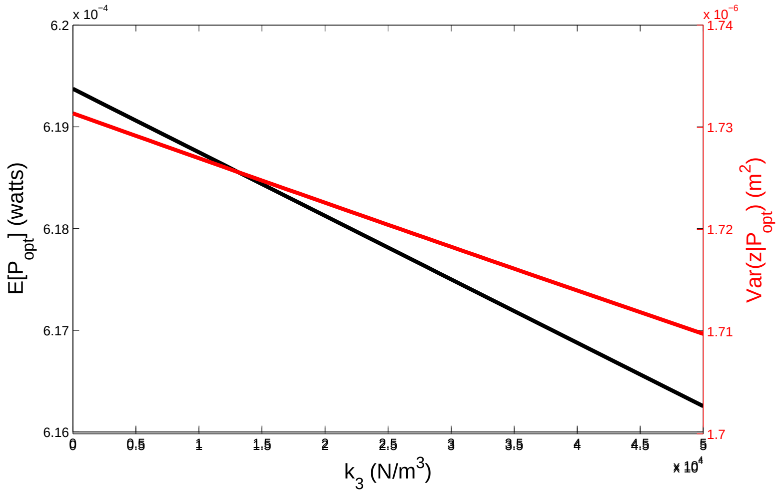

Figure 8.10: Response of device to excitation from subject 2 walking motion: the variation of displacement and power with nonlinear stiffness where $k = k_{opt}$. All other parameters are as shown in Table 8.1.

tion was to carry out a similar analysis using a different type of ambient excitation - bridge motion. Using 2 hours of acceleration data obtained from the midspan of the Humber bridge, the effects of varying the linear and nonlinear stiffness of the device was analysed in a similar manner to the previous section. The results of this investigation are shown in Figure 8.11 where it can be seen that, once again, any benefits with regards to displacement variance have come at the expense of reduced power output. Additionally, as with the walking motion case, the optimum linear stiffness has been reduced as a consequence of the addition of the nonlinear stiffness term. With the dominant frequencies of excitation being so low, this has resulted in the optimum level of linear stiffness approaching zero.

As before, the variation of expected power and displacement variance was plotted for different values of nonlinear stiffness where, at every data point, the linear stiffness was chosen to maximise power output (Figure 8.12). Once again it is clear that, while reducing the displacement variance, the introduction of the nonlinear spring term also reduces power output.

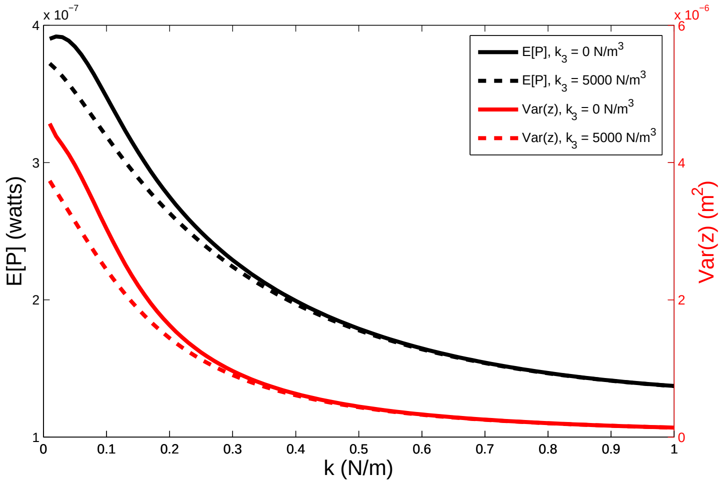

Figure 8.11: Response of device to bridge excitation: the variation of displacement and power with linear stiffness where the solid and dashed lines represent cases where $k_3 = 0$ and 5000 N/m^3 respectively. All other parameters are as shown in Table 8.1.

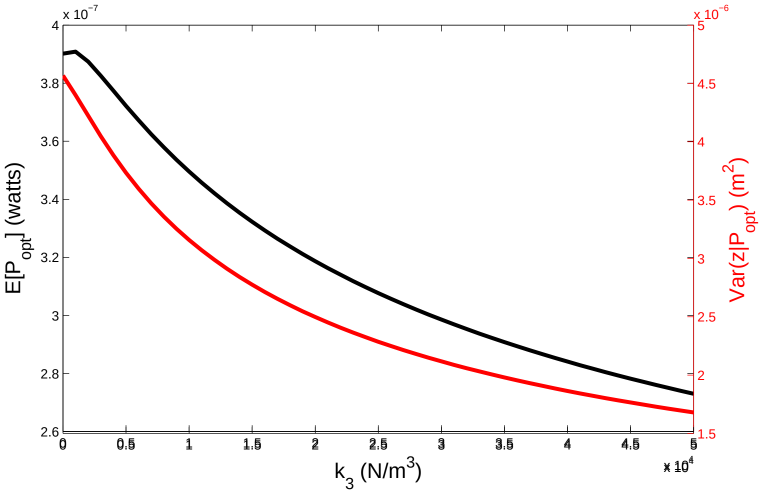

Figure 8.12: Response of device to bridge excitation: the variation of displacement and power with nonlinear stiffness where $k = k_{opt}$. All other parameters are as shown in Table 8.1.

8.5 Bistable nonlinear energy harvesting

Having investigated the application of a monostable nonlinear energy harvesting solution, attention is now directed towards bistable energy harvesters - the configuration of several different bistable energy harvesters was discussed in Chapter 2.

In the majority of the literature, the equation of motion for bistable energy harvesters is approximated by that of the bistable Duffing oscillator:

$$m\ddot{z} + c\dot{z} - kz + k_3 z^3 + F_e = -m y_a. \tag{8.3}$$

where it should be noted that equation (8.3) now contains a negative value of k such that, upon the appropriate selection of k and k_3, a device with a bistable potential is created.

8.5.1 Response to walking motion

As mentioned previously, it is clear that the power in the walking excitation signal is distributed over a relatively large range of frequencies. The purpose of this investigation was to identify whether a bistable device can harvest energy over a larger bandwidth such that it outperforms a linear resonant device. Figure 8.13 shows how the power delivered to the electrical domain varied with different values of k and k_3. Interestingly, the optimum amount of power is harvested when k is positive and k_3 approaches zero - in other words, the monostable linear device out performs the nonlinear bistable device. This can be seen more clearly in Figure 8.14 which shows two cross sections taken from the aforementioned contour plot.

The first point to note with regards to Figure 8.14 is that the power output in the region where $k = -10$ N/m and $k_3 = 8000$ N/m^3 is relatively small. In an effort to understand why, a phase portrait for the system with the afore mentioned values of linear and nonlinear stiffness was plotted (Figure 8.15). It is clear that the system is entrapped in one energy well and is unable to jump into the other well. Figure 8.16 shows a phase portrait for the case when $k = -3$ N/m and $k_3 = 8000$ N/m^3. Interwell dynamics have been activated although this has yielded little benefit with regards to power output. Finally, Figure 8.17 shows the phase portrait for the linear

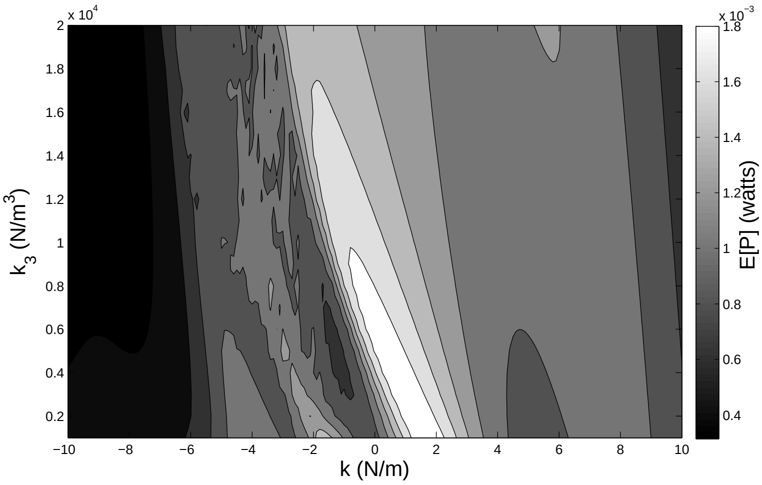

Figure 8.13: Walking excitation (subject 1): variation of power delivered to the electrical domain with changes in k and k_3. All other parameters are as shown in Table 8.1.

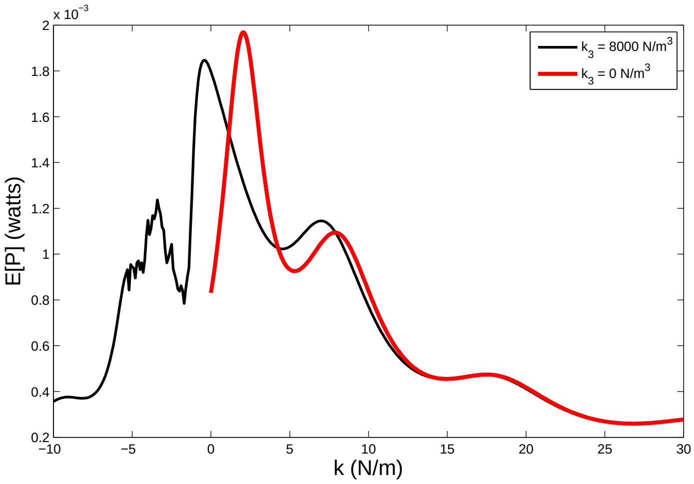

Figure 8.14: Walking excitation (subject 1): variation of power delivered to the electrical domain with changes in k where the black and red lines represent simulations where $k_3 = 8000$ and 0 N/m^3 respectively. All other parameters are as shown in Table 8.1.

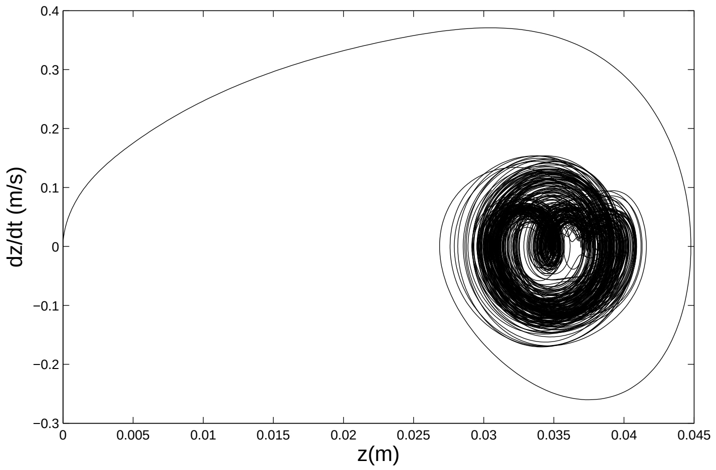

Figure 8.15: Phase portrait of bistable oscillator under walking excitation (subject 1) where k = -10 N/m and k_3 = 8000 N/m^3 and all other parameters are as shown in Table 8.1.

monostable case. In this case the linear monostable device has outperformed the nonlinear bistable device. Again, similar results were found for all three subjects.

8.5.2 Response to bridge motion

Analysing the response of a bistable device to the bridge excitation, the contour plot in Figure 8.18 was realised. Interestingly in this case, there are regions where the bistable device produces a power output similar to that of the linear monostable device. Figure 8.19 shows that, when k_3 = 2000 N/m^3, there is a region where having a negative value of k results in a power output very close to the linear case.

Again, to further understand the dynamics of the device, phase portraits were plotted using different values of linear and nonlinear stiffness. Setting $k = -0.1$ N and $k_3 = 2000$ N/m^3 such that device was in a 'high power' region of Figure 8.18 the phase portrait shown in Figure 8.20 was realised. The device is clearly demonstrating interwell dynamics - an interesting result as, with regards to the walking excitation case, this seemed to harm device performance. This result shows that the benefits of inducing interwell dynamics are certainly excitation specific. Moving into one of the relatively low power regions ($k = -0.2$ N and $k_3 = 2000$ N/m^3) then, as shown in Figure 8.21, it is clear that the device is entrapped in one energy well

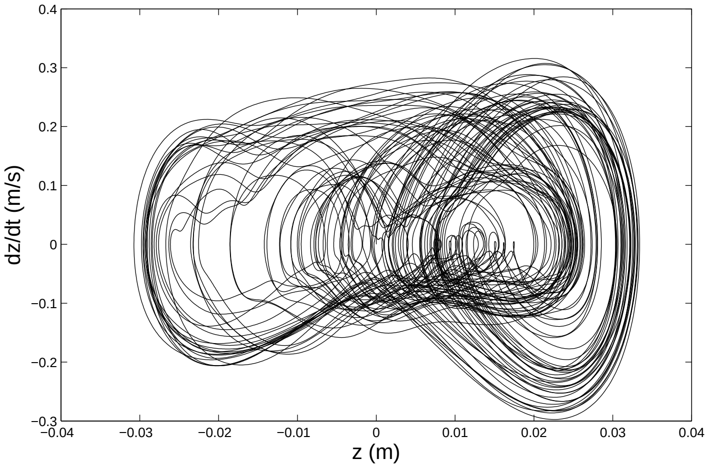

Figure 8.16: Phase portrait of bistable oscillator under walking excitation (subject 1) where k = -3 N/m and $k_3 = 8000$ N/m^3 and all other parameters are as shown in Table 8.1.

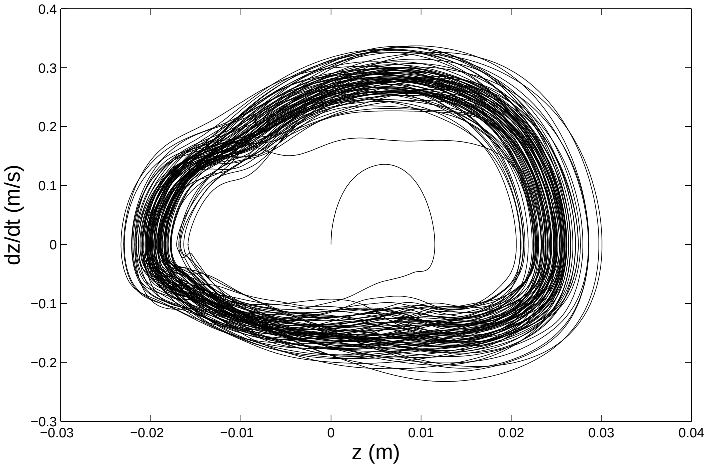

Figure 8.17: Phase portrait of bistable oscillator under walking excitation (subject 1) where $k = 2.5$ N/m and $k_3 = 0$ N/m^3 and all other parameters are as shown in Table 8.1.

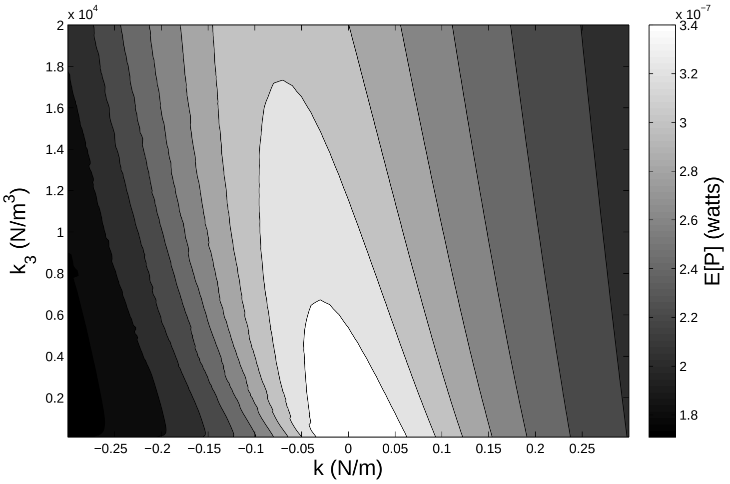

Figure 8.18: Bridge excitation: variation of power delivered to the electrical domain with changes in k and k_3. All other parameters are as shown in Table 8.1.

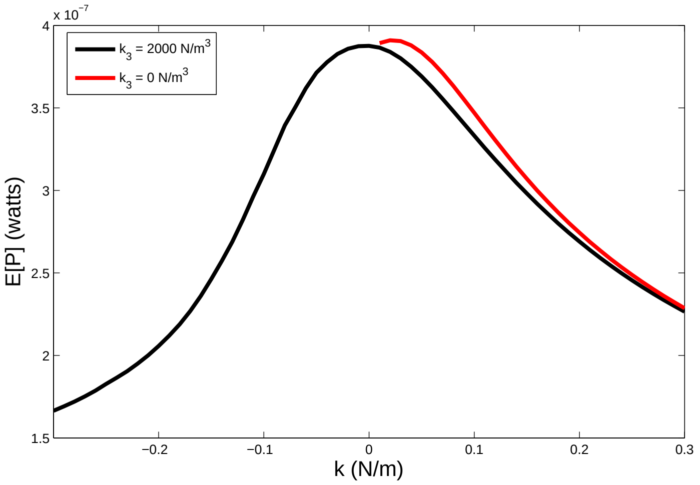

Figure 8.19: Bridge excitation: variation of power delivered to the electrical domain with changes in k where the black and red lines represent simulations where $k_3 =$ 2000 and 0 N/m^3 respectively. All other parameters are as shown in Table 8.1.

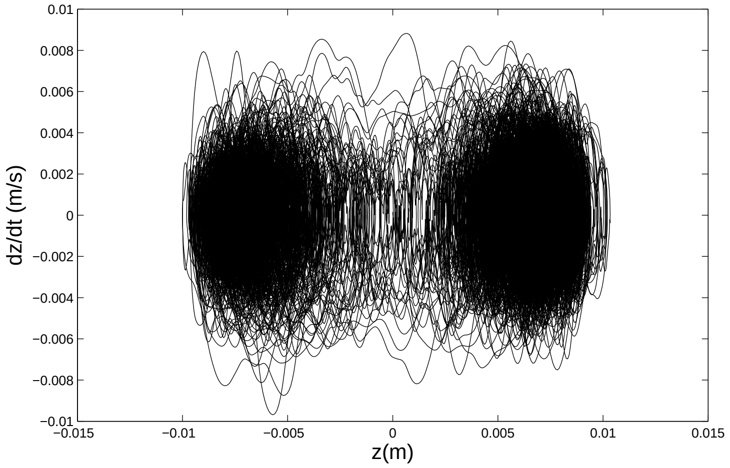

Figure 8.20: Phase portrait of bistable oscillator under bridge excitation where $k =$ -0.1 N/m and $k_3 = 2000$ N/m^3 and all other parameters are as shown in Table 8.1.

from which it is is unable to escape. It is also interesting to note that only a small alteration in linear stiffness ($\approx$ 0.1 N/m) was required to move from a device which can active interwell dynamics to one which cannot. This suggests that, if one did want to create a device capable of jumping between energy wells, one would have to tune its linear stiffness very precisely. In fact, this is exactly what one would have to do if they were attempting to tune the natural frequency of a linear device to the dominant frequency of excitation - therefore prompting one to ask whether there is any point in selecting a bistable energy harvester over a linear resonant energy harvester.

8.6 Future work and discussion

The main aim of this chapter is to emphasise that, for the development of energy harvesting solutions to be successful, the nature of ambient vibration sources will have to be analysed in more detail. This is something which may be possible to accomplish through use of the 'real vibration database' which was outlined in [77].

Another issue which is touched on in this chapter but not discussed thoroughly is the fact that both types of ambient excitation investigated have very low dominant frequencies. Constructing a small device to harvest energy from such frequencies would be difficult as, to achieve such a low natural frequency, one would require a

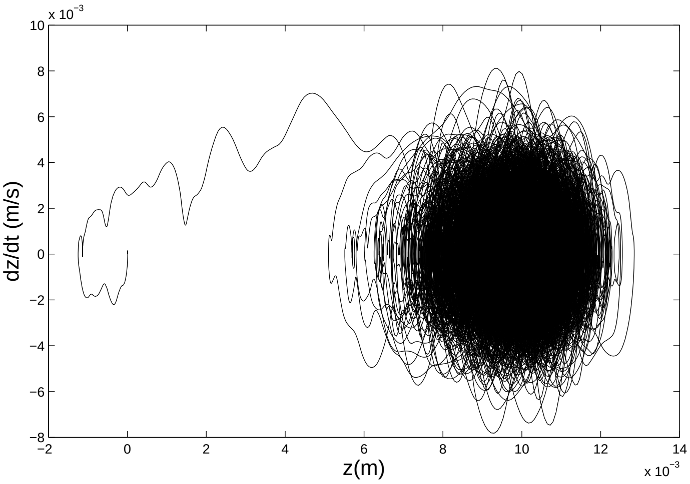

Figure 8.21: Phase portrait of bistable oscillator under bridge excitation where $k =$ -0.2 N/m and $k_3 = 2000$ N/m^3 and all other parameters are as shown in Table 8.1.

large mass or weak restoring force. While there are devices which are specifically designed for such purposes [42, 78] their reported natural frequencies are not as low as the dominant frequencies of the excitations shown in this paper.

The issue of low frequency energy harvesting brings one to question the suitability of electromagnetic and piezoelectric conversion mechanisms. The circuitry of piezoelectric devices are usually modelled as containing a capacitance and load resistance [45]. As it is known that a series combination of capacitor and resistor creates a high pass filter, it is intuitive to suggest that a piezoelectric device would be poorly suited to harvesting energy from low frequencies. On the other hand, electromagnetic devices whose circuitry is often modelled as a series combination of inductor and resistor would not suffer from such issues as, even if the inductance was large (which is unlikely in a small device), the circuit would be acting as a low pass filter - thus allowing it to harvest electrical energy from low frequencies.

With regards to nonlinear energy harvesting from low frequency vibrations, some recent works [49, 50] have suggested that Duffing-type nonlinearities could be introduced such that the device response contained subharmonics (frequencies below its natural frequency). In the author's opinion it is certainly worth investigating whether subharmonics could be used to allow a device with a relatively high natural frequency harvest energy from relatively low frequencies.

The final remark worthy of interest is with regards to bistable energy harvesters which are designed to exhibit a chaotic response. An interesting point that was raised in [47] is that, even if power output could be improved by inducing a chaotic response in the device there is the school of though that, even if this did maximise the power delivered to the electrical domain, its unperiodic nature would make it difficult to collect and store the electrical energy. This is certainly an area in which further research could be directed.

8.7 Summary

The aim of the work in this chapter was to assess whether nonlinear energy harvesting solutions which were developed under the assumption that ambient vibration sources can be approximated successfully by Gaussian white noise can be applied ubiquitously in the real world. Two possible ambient vibration sources were considered: human walking motion and bridge vibrations. It was shown that, although the benefits of deliberately inducing dynamic nonlinearities into such devices has been shown for the case of Gaussian white noise excitations, the same benefits could not be realised for the excitation types investigated here. Consequently, the main contribution of this investigation is to emphasise the fact that universally applicable energy harvesting solutions cannot be realised without more careful thought about the nature of ambient vibrations.

The second important finding from this chapter is that, to successfully harvest energy from ambient vibration sources, one will likely need to develop a device which is capable of operating at very low frequencies. It is stated here that electromagnetic energy harvesters will be better suited to this type of problem as the circuitry of piezoelectric devices are known to act as a high pass filters - thus removing low frequency electrical signals. There is certainly much scope in investigating whether dynamic nonlinearities can be used to aid the harvesting of energy from low frequency vibrations.

Chapter 9

CONCLUSIONS AND FUTURE WORK

9.1 Thesis Summary

Shown here is a brief summary of the chapters from this thesis.

Chapter 2 - Literature review

Chapter 2 details a review of energy harvesting literature relevant to this thesis. It identifies key papers which aided the transition from the deterministic analyses of linear energy harvesters to the probabilistic analyses of nonlinear energy harvesters (which forms a large part of this thesis). Of specific relevance to this thesis is the work of Mann and Sims [30] in which it was suggested that energy harvester performance could be aided through the deliberate introduction of Duffing-type nonlinearities.

Chapter 3 - Experiment

In this chapter a mathematical model of the Mann and Sims electromagnetic energy harvester [30] is developed and validated using experimental data. It is shown that the device response is sensitive to the effects of friction. Consequently, after a detailed analysis of several different friction models of varying levels of complexity it is shown that the inclusion of a combination of viscous and Coulomb damping can be used to accurately model the mechanical losses in the device.

With regards to the electrical portion of the device, it is shown that inductance has a negligible effect on device performance and that the flux displacement curve of the device can safely be approximated by a linear relationship.

Chapter 4 - Harmonic excitations

With a validated model of the Mann and Sims device developed, the method of harmonic balance is used alongside digital simulations to approximate its response to sinusoidal excitations of different frequencies. The significant effects on device power output as a result of relatively small changes in friction is demonstrated. As well as this, expressions are developed which are shown to accurately predict at what point friction in the device will prevent it from functioning.

Chapter 5 - Random Excitations: Monte Carlo Simulation

Given the stochastic nature of many ambient vibration sources, Monte Carlo simulations are used to analyse the response of the Mann and Sims device to Gaussian white and coloured noise excitations. Through dimensional analysis the model developed in Chapter 3 is validated over a region of parameter space. Simulations are then used to shown that, over the parameter space investigated, Duffing-type nonlinearities do not enhance the power output of the white noise excited device. As well as this, the detrimental effects of friction and potential tuning capabilities of the nonlinear spring are demonstrated.

Chapter 6 - Random Excitations: FPK Equation

Building on the work in Chapter 5, the Fokker-Planck-Kolmogorov equation is used to develop a closed form expression detailing the response of the Mann and Sims device to Gaussian white noise excitations. Using this expression it is shown that Duffing-type nonlinearities can be used to reduce the rattle space of the device without effecting its power output thus allowing the construction of smaller devices.

An expression detailing the effect of the nonlinear spring term on device size is developed and validated. It is also shown that, when delivering power to a load resistor, the optimum load resistance is a function of the magnetic flux in the device and different from that which is dictated by impedance matching. This is then validated experimentally.

Chapter 7 - Random Excitations: Equivalent Linearisation

In this chapter Equivalent Linearisation is used to develop a relatively simple expression approximating the benefits of Duffing-type nonlinearities with regards to device size. As well as this it is shown that the effects of friction on the power output of the randomly excited device can be closely approximated analytically.

Chapter 8 - Ambient Excitations

In this chapter the applicability of nonlinear energy harvesting solutions developed using Gaussian white noise excitations to the scenarios of harvesting of energy from human walking motion and bridge vibrations is investigated. This analysis differs from the preceding chapters in that a range of current nonlinear energy harvesting solutions are considered alongside that which was proposed by Mann and Sims. The key contribution of this chapter is the finding that the successful application of nonlinear energy harvesting solutions is very much dependent on the excitation type. This finding provides much scope for future work - as discussed more in section 9.3.

9.2 Contributions to Knowledge

Briefly detailed here are the main contributions to knowledge from this thesis as well as reference to the publications in which they appear (publications currently under review are not included).

- To accurately model the Mann and Sims energy device one must include friction effects. Following an investigation into several different friction models it was found that friction in the device can be modelled to a high degree of accuracy using Coulomb damping. These findings were experimentally validated

[79, 80, 81].

- Assumptions of a linear flux-displacement relationship and negligible inductance in modelling the electronic component of an electromagnetic energy harvester were confirmed experimentally. This shows that future investigations into the effects of inductance and/or nonlinear flux displacement relationships on device performance are unlikely to be relevant in real energy harvesting applications [82].

- Expressions showing the effects of Duffing-type and friction nonlinearities on the harmonically excited Mann and Sims energy harvester were developed and used to demonstrate the effect of such nonlinear terms on the frequency response of the device. An expression detailing at what point friction will prevent the device from functioning was also developed [80].

- Simulations showing the effects of Duffing-type and friction nonlinearities on the randomly excited device were conducted (white and coloured noise excitations) [80].

- The FPK equation used to show that Duffing-type nonlinearities can be used to reduce device size without effecting power output (when excited by Gaussian white noise) thus providing a method for constructing smaller energy harvesters without harming device performance. This result is particularly important with regards to energy harvesters whose target application dictates that they must be of a small size (wearable energy harvesters for example) [82, 83].

- FPK equation used to show the the optimum load resistance of a randomly excited electromagnetic energy harvester is not equal to that which is dictated by impedance matching but is in fact a function of the rate of change of magnetic flux. This was then validated experimentally [83, 82].

- The techniques of equivalent linearisation was used to develop an expression approximating the effect of friction on power output of a randomly excited device. This is of importance as the performance of electromagnetic energy harvesters are likely to be sensitive to friction affects [81].

- Difficulties with applying current nonlinear energy harvesting solutions to real scenarios highlighted [84].

- Low frequency nature of ambient vibrations indicate that electromagnet energy harvesters are more suitable to real world applications than piezoelectric energy harvesters [84].

9.3 Future Work and Discussion

9.3.1 Modelling

Chapter 3 detailed the development and validation of a digital model of the Mann and Sims energy harvester. The conclusions drawn from this work are, in some respects, the most significant of this thesis. The finding that the response of the device could not be accurately modelled without accounting for the effects of friction are of particular importance - the vast majority of the work on this type of energy harvester model its mechanical losses as a viscous damper. This does make the modelling process somewhat simpler - friction is a particularly complicated form of nonlinearity for which many of the available models are difficult to analyse using a strictly analytical approach (especially when one considers random excitation conditions). However, it is the author's opinion that nonlinear energy harvesting solutions that have been developed using models which, in reality, are not capable of replicating the response of real devices will likely be ineffective. This is compounded by the results shown in Chapters 4 and 7 where it was shown that small changes in friction can greatly effect device performance for the cases of harmonic and random excitations respectively. Future work should be mindful of friction effects when developing energy harvesting solutions.

With regards to device electronics there is the school of thought that the effects of inductance on the performance of electromagnetic energy harvesters is of importance ([16] and [59] provided a detailed analysis of the effect of inductance of sinusoidally and randomly excited energy harvesters respectively). In Chapter 3 it was shown that one can model the power output of an electromagnetic energy harvester to a good degree of accuracy despite assuming inductance effects are negligible. While the author accepts that a series combination of inductor and resistor will act as a low pass filter which may result in the loss of high frequency electrical signals, the number of coils of wire needed to create a level of inductance that would significantly effect device performance is unrealistic - especially when one considers the very low frequency nature of ambient vibrations (such as those shown in Chapter 8). With regards to those nonlinearities whose presence in energy harvesters devices are inevitable (as opposed to by design), for future work to be beneficial to energy harvesting research it should be focused more on investigating the effects of friction than the effects of inductance.

A significant part of Chapter 3 was devoted to analysing several ‘off the shelf’ friction models in an attempt to find which one was the most suitable for this particular problem. From a system identification point of view this is interesting as the modelling of friction is an example of a problem where several different models may be compatible with a given set of experimental observations. In such a scenario one needs to somehow ‘rate’ how the models perform relative to each other. This is complicated by the fact that, generally, by adding complexity to a model one will generally improve its performance. This means that one has to trade off model performance with model complexity. For example, in Chapter 3 it was shown that the added complexity of the LuGre friction model did not significantly improve the ability of the model to replicate the experimental results compared to relative simple Coulomb damping model. In a recent work [85] Worden and Hensman utilised a measure known as the Deviance Information Criterion (DIC) - a model selection indicator which is chosen such that it penalises model complexity while simultaneously rewarding model performance. With friction being present in the majority of dynamic systems it is the author’s opinion that much good would come from investigating the performance of friction models using such a model selection criteria.

9.3.2 Energy harvester optimisation

The most important contribution from Chapter 5 is the finding that, when excited with Gaussian white noise, Duffing-type nonlinearities can be used to reduce the rattle space of an electromagnetic energy harvester without affecting its power output. It is interesting to note that in [43] the finding that Duffing-type nonlinearities cannot increase power output led to the conclusion that they are of no benefit. This emphasises the fact that, when considering the optimisation of energy harvester performance, one cannot only focus on the maximisation of power delivered to the electrical domain. Future works should also consider the optimisation of device size, weight, cost of manufacture, sensitivity to changes in excitation and ability to provide an electrical energy signal which can easily be stored. This last point is particularly relevant to those devices which are designed to deliver a relatively large amount of energy to the electrical domain through the induction of chaotic vibrations (as discussed in Chapter 8) as it may be that the energy in electrical signals of this type are difficult to store [47]. To address this type of issue future work on energy harvesters will have to be conducted simultaneously from an electrical, as well as mechanical, perspective.

9.3.3 Ambient excitations

The order of this thesis was chosen such that, reading front to back, the reader would have an idea of the trends in energy harvesting research over recent years. This was to show how the focus of energy harvesting research has very much switched from analysing sinusoidally excited devices to those which are subjected to random excitations. This is important as it it acknowledges the fact that many ambient vibration sources appear to be of a stochastic nature and that, consequently, probabilistic methods need to be used to evaluate energy harvester performance.

In Chapter 8 it was shown that it was difficult to extrapolate the results from some of these works to the scenarios of harvesting energy from human walking motion and bridge vibrations. This does not mean that previous work on randomly excited energy harvesters is unimportant. It is not the authors intention to convey the belief that all energy harvesting solutions developed under the assumption of Gaussian white noise cannot be applied to real energy harvesting scenarios - only two out of a huge range of possible vibrational energy sources were considered in this thesis. The aim of the work shown in Chapter 8 was to emphasise that in the future development of energy harvesting solutions researchers will have to pay more careful consideration into the types of energy source from which power is to be harvested. With this in mind future work could be directed towards investigating the sensitivity of energy harvesting solutions to the excitation type using well established sensitivity analysis techniques (such as those shown in [86]).

One of the most important things to consider when designing an energy harvester is the fact that ambient vibration sources often have time dependent dominant frequencies. Although this thesis has been focused on nonlinear energy harvesters it is worth noting that much research has also been devoted towards the development of tuneable devices (a brief description of these works is given in Chapter 2). Theoretically, such a device would be able to adapt its natural frequency in response to changes in the dominant frequency of excitation. The obvious draw back of such a device is that it would require some kind of electrically powered mechanism which was capable of monitoring the frequency content of the excitation. However, some researchers have recently turned their attention to investigating 'self-tuning' energy harvesters which are constructed such that they can adapt their natural frequency without requiring any additional electrical equipment. An example of this is shown in [26] where a device was designed which could be placed inside a rotating tyre. This is of particular interest as the construction of this energy harvester was such that it was able to adapt to changes in the angular velocity of the tyre. In the author's opinion future work should certainly be devoted towards the development of self-tuneable energy harvesters.

Appendix A

PUBLICATIONS BY AUTHOR

Accepted Publications

Journal Papers

- P L Green, K Worden, K Atallah and N D Sims. The benefits of Duffing-type nonlinearities and electrical optimisation of a mono-stable energy harvester under white Gaussian excitations. Journal of Sound and Vibration, 331(20):4504 4517, 2012.
- P L Green, K Worden, K Atallah and N D Sims. The effect of Duffing-type non-linearities and Coulomb damping of the response of an energy harvester to random excitations. Journal of Intelligent Material Systems and Structures, 2012, DOI: http://dx.doi.org/10.1177/1045389X12446520. **Article in Press.**

Conference Papers

- N Perisic, P L Green, and K Worden. Identification of time-varying non-linear systems using differential evolution algorithm. Proceedings of IMAC XXX, Conference and Exposition on Structural Dynamics - Orange County, California, 11 - 14 Feb, 2013.
- P L Green and K Worden. Modelling Friction in a Nonlinear Dynamic System

via Bayesian Inference. Proceedings of IMAC XXX, Conference and Exposition on Structural Dynamics - Orange County, California, 11 - 14 Feb, 2013.

- P L Green, E Papatheou, and N D Sims. Energy harvesting from human motion: an evaluation of current nonlinear energy harvesting solutions. Proceedings of MPSVA 2012, Conference on Modern Practice in Stress and Vibration Analysis - Glasgow, 29-31 August 2012.
- P L Green, K Worden, K Atallah, and N D Sims. The modelling of friction in a randomly excited energy harvester. Proceedings of ISMA 2012, Conference on Noise and Vibration Engineering, Leuven, Belgium, 20-22 September 2012.
- P L Green, K Worden, K Atallah, and N D Sims. The benefits of duffing-type nonlinearities and electrical optimisation of a randomly excited energy harvester. Proceedings of IMAC XXX, Conference and Exposition on Structural Dynamics - Jacksonville, Florida, 30 Jan - 2 Feb, 2012.
- E Papatheou, P L Green, V Racic, Brownjohn JMW, and N D Sims. A short investigation of the effect of an energy harvesting backpack on the human gait. Proceedings of SPIE 2012, Smart Structures/NDE, San Diego, California, 2012.
- P L Green, K Worden, K Atallah, and ND Sims. The effect of Duffing-type nonlinearities and Coulomb damping on the response of an energy harvester to random excitations. EuroMech Colloquium 530: Structural Control and Energy Harvesting - Bristol, UK, 25-27 July 2011.
- P L Green, K Worden, K Atallah, and ND Sims. Performance of linear and nonlinear resonant frequency energy harvesters under uncertain loading conditions. USD2010: 3rd International Conference on Uncertainty in Structural Dynamics - Leuven, Belgium, 20-22 September 2010.

Publications Under Review

Journal Papers

- P L Green, E Papatheou and N D Sims. Energy harvesting from human motion and bridge vibrations: an evaluation of current nonlinear energy harvesting solutions. Journal of Intelligent Material Systems and Structures (**Under review**).
- P L Green, K Worden and N D Sims. On the identification and modelling of friction in a randomly excited energy harvester. Journal of Sound and Vibration (**Under review**).

Appendix B

USEFUL DERIVATIONS

B.1 Power per cycle of linear SDOF energy harvester under sinusoidal excitations

B.1.1 Transfer Function

Consider a device with equation of motion:

$$\ddot{z} + 2\zeta\omega_n\dot{z} + \omega_n^2 z = -\ddot{y}, \tag{B.1}$$

where y is base displacement, z is relative displacement between the mass and base and ω_n and ζ represent the natural frequency and damping ratio respectively. On can then assume an excitation of the form $y = Y\sin(\omega t + \phi)$ and response $z = Z\sin(\omega t)$ such that, using elementary trigonometric relations, the equation of motion can be written:

$$-\omega^2 Z\sin(\omega t) + 2\zeta\omega_n\omega Z\cos(\omega t) + \omega_n^2 Z\sin(\omega t)$$

$$= \omega^2 Y(\sin(\omega t)\cos(\phi) + \cos(\omega t)\sin(\phi)). \tag{B.2}$$

Equating coefficients of $\sin(\omega t)$ and $\cos(\omega t)$ one obtains two equations:

$$-\omega^2 Z + \omega_n^2 Z = \omega^2 Y \cos(\phi), \tag{B.3}$$

$$2\zeta\omega_n\omega Z = \omega^2 Y \sin(\phi), \tag{B.4}$$

which, when squared and added lead to the expression:

$$\frac{Z^2}{Y^2} = \frac{\omega^4}{(-\omega^2 + \omega_n^2)^2 + (2\zeta\omega_n\omega)^2}. \tag{B.5}$$

such that:

$$\frac{Z}{Y} = \frac{\omega_r^2}{\sqrt{(1-\omega_r^2)^2 + (2\zeta\omega_r)^2}} \tag{B.6}$$

where $\omega_r = \omega/\omega_n$.

B.1.2 Power per Cycle

Assuming sinusoidal motion, the average power per cycle will be given by:

$$p_{av} = \frac{1}{T}\int_0^T p(t)dt, \tag{B.7}$$

where T is the time for one cycle. Given that the power extracted by a viscous damper is given cy $c\dot{z}^2$ and it is known that $\dot{z} = \omega Z \cos(\omega t)$ allows one to write:

$$\begin{aligned} p_{av} &= \frac{\omega^2 c Z^2}{T}\int_0^T \cos^2(\omega t)dt \\ &= \frac{\omega^2 c Z^2}{2T}\int_0^T 1 + \cos(2\omega t)dt \\ &= \frac{\omega^2 c Z^2}{2T}\left\{[t]_0^T + \frac{1}{2\omega}[\sin(2\omega t)]_0^T\right\} \\ &= \frac{\omega^2 c Z^2}{2}. \end{aligned} \tag{B.8}$$

Recalling the transfer function of the linear system (equation B.6) therefore allows one to write the average power per cycle as:

$$\begin{aligned} p_{av} &= \frac{c}{2}\frac{\omega^2\omega_r^4Y^2}{(1-\omega_r^2)^2+(2\zeta\omega_r)^2} \\ &= \frac{\zeta\omega^3\omega_r^3Y^2m}{(1-\omega_r^2)^2+(2\zeta\omega_r)^2}. \end{aligned} \tag{B.9}$$

B.2 From autocorrelation to power spectral density

The variable x is defined as a continuous random variable with an expected value of zero. Recalling that the autocorrelation of x is defined as:

$$\phi_{xx} = E[x(t)x(t+\tau)] \tag{B.10}$$

and the property that:

$$E[x] \approx \frac{1}{T}\int_0^T x(t)dt \tag{B.11}$$

allows one to write:

$$\phi_{xx}(\tau) = E[x(t)x(t+\tau)] = \int_{-\infty}^{\infty} x(t)x(t+\tau)dt. \tag{B.12}$$

It should be noted that a constant in front of the integral in equation (B.12) has been omitted. This is just to simplify the following analyses - one should think of the constant as being removed by a normalisation. Now, if one recollects the well known convolution theorem:

$$\mathcal{F}^{-1}[X(\omega)^2] = \int_{-\infty}^{\infty} x(t-\tau)x(\tau)d\tau, \tag{B.13}$$

(where $\mathcal{F}^{-1}$ is the inverse Fourier transform and $X(\omega)$ is the frequency domain representation of $x(t)$) then one can write the following relation:

$$\phi_{xx}(\tau) = \mathcal{F}^{-1}[X(\omega)^2], \tag{B.14}$$

such that the power spectral density (PSD) of the signal $P_{xx}(\omega)$ can be found from the Fourier transform of the autocorrelation function:

$$P_{xx}(\omega) = \mathcal{F}[\phi_{xx}(\tau)]. \tag{B.15}$$

Additionally, it allows one to write the autocorrelation function as:

$$\phi_{xx} = \mathcal{F}^{-1}[P_{xx}(\omega)]. \tag{B.16}$$

B.3 Formation of FPK equation for SDOF system with nonlinear stiffness

Recalling the 2D Chapman-Kolmogorov equation after expansion by the Taylor series:

$$\begin{aligned}\frac{\partial P(x_1, x_2, t+\delta t)}{\partial t} &= -\sum_{i=1}^{2}\left[\frac{\partial P(x_1, x_2, t)}{\partial x_i}\frac{\bar{z}_i}{\delta t}\right] \\ &+\frac{1}{2}\sum_{i=1}^{2}\sum_{j=1}^{2}\left[\frac{\partial^2 P(x_1, x_2, t)}{\partial x_i \partial x_j}\frac{\bar{z}_i\bar{z}_j}{\delta t}\right]\end{aligned} \tag{B.17}$$

where

$$\bar{z}_i = \int_{-\infty}^{\infty}\int_{-\infty}^{\infty} z_i Q(z_1, z_2, \delta t) dz_1 dz_2 \tag{B.18}$$

and

$$\bar{z}_i\bar{z}_j = \int_{-\infty}^{\infty}\int_{-\infty}^{\infty} z_i z_j Q(z_1, z_2, \delta t) dz_1 dz_2. \tag{B.19}$$

Consider the SDOF system:

$$\ddot{x} + c\dot{x} + \Phi(x) = w(t) \tag{B.20}$$

where $w(t)$ is a zero mean white noise Gaussian process and $\Phi(x)$ is a nonlinear stiffness function. Defining state space variables:

$$x_1 = x \tag{B.21}$$

$$x_2 = \dot{x} \tag{B.22}$$

then, for this system:

$$\frac{\bar{z}_1}{\delta t} = \frac{E[z_1]}{\delta t} = \frac{E[\delta x_1]}{\delta t} = \frac{\delta t E[x_2]}{\delta t} = x_2. \tag{B.23}$$

Also:

$$\frac{\bar{z}_2}{\delta t} = \frac{E[\delta x_2]}{\delta t} = \frac{\delta t E[\dot{x}_2]}{\delta t} = E[f(t) - cx_2 - \Phi(x_1)], \tag{B.24}$$

therefore, recalling that $E[w(t)] = 0$:

$$\frac{\bar{z}_2}{\delta t} = -cx_2 - \Phi(x_1). \tag{B.25}$$

Finally, one needs to identify the values of $\bar{z}_i \bar{z}_j / \delta t$. Starting with $i = 1$ and $j = 1$:

$$\frac{\bar{z}_1^2}{\delta t} = \frac{E[\delta x_1^2]}{\delta t} = \delta t E[x_2] \tag{B.26}$$

and so, as δt approaches zero

$$\frac{\bar{z}_1^2}{\delta t} = 0 \tag{B.27}$$

By a similar analysis it can be shown that $\bar{z}_1 \bar{z}_2 / \delta t = \bar{z}_2 \bar{z}_1 / \delta t = 0$. Setting $i = 2$, $j = 2$:

$$\frac{\bar{z}_2^2}{\delta t} = \frac{E[\delta x_2^2]}{\delta t} = \frac{E[(\delta t \dot{x}_2)^2]}{\delta t} = \frac{E[(\delta t(f(t) - C(x_2) - \Phi(x_1))^2]}{\delta t} \tag{B.28}$$

After expanding the brackets, letting δt converge to zero and using the covariance relation for white noise one can show that:

$$\frac{\bar{z}_2^2}{\delta t} = \frac{S}{2} \tag{B.29}$$

Consequently, the FPK equation for this system is:

$$\frac{\partial p_J(x_1,x_2,\delta t)}{\partial t} = -x_2\frac{\partial P(x_1,x_2,t)}{\partial x_1} + \frac{\partial}{\partial x_2}\left[(cx_2+\Phi(x_1))P(x_1,x_2,t)\right] + \frac{S}{4}\frac{\partial^2 P(x_1,x_2,t)}{\partial x_2^2}. \tag{B.30}$$

B.4 Displacement and velocity variance of SDOF system under Gaussian white noise excitation

B.4.1 Stationary Probability Density Function

Consider the system:

$$m\ddot{z} + c\dot{z} + kz = w(t) \tag{B.31}$$

where $w(t)$ is zero mean Gaussian white noise with autocorrelation:

$$\phi_{ww}(\tau) = \frac{S}{2}\delta(\tau). \tag{B.32}$$

Defining the state space variables $z_1 = z$ and $z_2 = \dot{z}$ then the stationary probability density function (PDF) of the system is given by:

$$P(z_1,z_2) = P(z_1)P(z_1) \tag{B.33}$$

where

$$P(z_1) = A_1\exp\left(-\frac{2kz_1^2c}{Sm^2}\right), \tag{B.34}$$

and

$$P(z_2) = A_2\exp\left(-\frac{2z_2^2c}{Sm}\right) \tag{B.35}$$

where A_1 and A_2 are normalisation constants. Having found the PDF of the afore mentioned linear system, one can then calculate the relative displacement and velocity variances.

B.4.2 Displacement Variance

Given that $E[z_1] = 0$ then the displacement variance is given by:

$$\sigma_{z_1}^2 = E[z_1^2] = \int_{-\infty}^{\infty} P(z_1) z_1^2 dz_1. \tag{B.36}$$

Using equation (B.34) allows one to write:

$$\sigma_{z_1}^2 = A_1 \int_{-\infty}^{\infty} \exp\left(-\frac{2kz_1^2c}{Sm^2}\right) z_1^2 dz_1. \tag{B.37}$$

With the aim of integrating by parts, one can define:

$$u = z_1, \tag{B.38}$$

such that:

$$du = dz_1. \tag{B.39}$$

Also, defining:

$$\frac{dv}{dz_1} = z_1 \exp\left(-\frac{2kz_1^2c}{Sm^2}\right) \tag{B.40}$$

and noting that :

$$\frac{d}{dz_1}\exp\left(-\frac{2kz_1^2c}{Sm^2}\right) = -\frac{4kz_1c}{Sm^2}\exp\left(-\frac{2kz_1^2c}{Sm^2}\right), \tag{B.41}$$

such that:

$$\frac{d}{dz_1}\left\{-\frac{Sm^2}{4kc}\exp\left(-\frac{2kz_1^2c}{Sm^2}\right)\right\} = z_1 \exp\left(-\frac{2kz_1^2c}{Sm^2}\right), \tag{B.42}$$

allows one to write:

$$v = -\frac{Sm^2}{4kc}\exp\left(-\frac{2kz_1^2c}{Sm^2}\right). \tag{B.43}$$

One can now integrate equation (B.37) by parts to find that:

$$\sigma_{z_1}^2 = A_1\left\{\left[z_1\left(-\frac{Sm^2}{4kc}\exp\left(-\frac{2kz_1^2c}{Sm^2}\right)\right)\right]_{-\infty}^{\infty} + \frac{Sm^2}{4kc}\int_{-\infty}^{\infty}\exp\left(-\frac{2kz_1^2c}{Sm^2}\right)dz_1\right\} \tag{B.44}$$

$$= \frac{Sm^2}{4kc}\int_{-\infty}^{\infty}A_1e\left(-\frac{2kz_1^2c}{Sm^2}\right)dz_1 \tag{B.45}$$

$$= \frac{Sm^2}{4kc}\int_{-\infty}^{\infty}P(z_1)dz_1. \tag{B.46}$$

Recalling that the total area underneath a probability distribution function must be unity then:

$$\sigma_{z_1}^2 = \frac{Sm^2}{4kc}. \tag{B.47}$$

B.4.3 Velocity Variance

Following a similar procedure to the previous section, the analysis begins with the relative velocity PDF (equation (B.35)):

$$P(z_2) = A_2\exp\left(-\frac{2z_2^2c}{Sm}\right), \tag{B.48}$$

such that the velocity variance can be found from:

$$\sigma_{z_2}^2 = \int_{-\infty}^{\infty}P(z_2)z_2^2dz_2 = A_2\int_{-\infty}^{\infty}\exp\left(-\frac{2z_2^2c}{Sm}\right)z_2^2dz^2. \tag{B.49}$$

As before, defining:

$$u = z_2, \tag{B.50}$$

and

$$dv = z_2 \exp\left(-\frac{2z_2^2 c}{Sm}\right), \tag{B.51}$$

such that,

$$du = dz_2, \tag{B.52}$$

and

$$v = -\frac{Sm}{4c} \exp\left(-\frac{2z_2^2 c}{Sm}\right), \tag{B.53}$$

then the relative velocity variance can be found by integrating equation (B.49) by parts such that:

$$\sigma_{z_2}^2 = \frac{Sm}{4c}. \tag{B.54}$$

Bibliography

[1] F. Khoshnoud and C.W. De Silva. Recent advances in mems sensor technology-mechanical applications. *IEEE Instrumentation and Measurement Magazine*, 15(2):14–24, 2012.

[2] F. Khoshnoud and C.W. De Silva. Recent advances in mems sensor technology-biomedical applications. *IEEE Instrumentation and Measurement Magazine*, 15(1):8–14, 2012.

[3] F. Khoshnoud and C.W. De Silva. Recent advances in mems sensor technology-thermo-fluid and electro-magnetic devices. *IEEE Instrumentation and Measurement Magazine*, 15(3):16–20, 2012.

[4] R.S. Sanders and M.T. Lee. Implantable pacemakers. *Proceedings of the IEEE*, 84(3):480–486, 1996.

[5] I.D. Capel, H.M. Dorrell, E.P. Spencer, and M.W.L. Davis. The amelioration of the suffering associated with spinal cord injury with subperception transcranial electrical stimulation. *Spinal Cord*, 41(2):109–117, 2003.

[6] G.J. Renzenbrink and M.J. Ijzerman. Percutaneous neuromuscular electrical stimulation (p-nmes) for treating shoulder pain in chronic hemiplegia. effects on shoulder pain and quality of life. *Clinical Rehabilitation*, 18(4):359–365, 2004.

[7] K. Baert, B. Gyselinckx, T. Torfs, V. Leonov, F. Yazicioglu, S. Brebels, S. Donnay, J. Vanfleteren, E. Beyne, and C. Van Hoof. Technologies for highly miniaturized autonomous sensor networks. *Microelectronics Journal*, 37(12):1563–1568, 2006.

[8] S. Roundy, P.K. Wright, and J. Rabaey. A study of low level vibrations as a power source for wireless sensor nodes. *Computer Communications*, 26(11):1131–1144, 2003.

[9] R.L. Harne. Concurrent attenuation of, and energy harvesting from, surface vibrations: Experimental verification and model validation. *Smart Materials and Structures*, 21(3), 2012.

[10] S.P. Beeby, M.J. Tudor, and N.M. White. Energy harvesting vibration sources for microsystems applications. *Measurement Science and Technology*, 17(12):R175, 2006.

[11] J.J. Kiely, D.V. Morgan, D.M. Rowe, and J.M. Humphrey. Low cost miniature thermoelectric generator. *Electronics Letters*, 27(25):2332 –2334, dec. 1991.

[12] S. Roundy. *Energy Scavenging for Wireless Sensor Nodes with a Focus on Vibration to Electricity Conversion.* PhD thesis, Dept. of EECS, UC Berkeley, 2003.

[13] C.B. Williams and R.B. Yates. Analysis of a micro-electric generator for microsystems. *Sensors and Actuators A: Physical*, 52(1-3):8 – 11, 1996.

[14] P.D. Mitcheson, T.C. Green, E.M. Yeatman, and A.S. Holmes. Architectures for vibration-driven micropower generators. *Journal of Microelectromechanical Systems*, 13(3):429–440, JUN 2004.

[15] N.G. Stephen. On energy harvesting from ambient vibration. *Journal of Sound and Vibration*, 293(1-2):409 – 425, 2006.

[16] B.P. Mann and N.D. Sims. On the performance and resonant frequency of electromagnetic induction energy harvesters. *Journal of Sound and Vibration*, 329(9):1348–1361, APR 26 2010.

[17] C.B. Williams, C. Shearwood, M.A. Harradine, P.H. Mellor, T.S. Birch, and R.B. Yates. Development of an electromagnetic micro-generator. *IEE Proceedings: Circuits, Devices and Systems*, 148(6):337–342, 2001.

[18] S. Beeby and N. White. *Energy Harvesting for Autonomous Systems.* Smart Materials, Structures, and Systems. Artech House, 2010.

[19] S.M. Shahruz. Design of mechanical band-pass filters for energy scavenging. *Journal of Sound and Vibration*, 292(3-5):987–998, 2006.

[20] Q. Ou, X. Chen, S. Gutschmidt, A. Wood, N. Leigh, and A.F. Arrieta. An experimentally validated double-mass piezoelectric cantilever model for broadband vibration-based energy harvesting. *Journal of Intelligent Material Systems and Structures*, 23(2):117–126, 2012.

[21] A. Aladwani, M. Arafa, O. Aldraihem, and A. Baz. Cantilevered piezoelectric energy harvester with a dynamic magnifier. *Journal of Vibration and Acoustics, Transactions of the ASME*, 134(3), 2012.

[22] H. Liu, Z. Huang, T. Xu, and D. Chen. Enhancing output power of a piezoelectric cantilever energy harvester using an oscillator. *Smart Materials and Structures*, 21(6), 2012.

[23] V.R. Challa, M.G. Prasad, Y. Shi, and F.T. Fisher. A vibration energy harvesting device with bidirectional resonance frequency tunability. *Smart Materials and Structures*, 17(1), 2008.

[24] W. Al-Ashtari, M. Hunstig, T. Hemsel, and W. Sextro. Frequency tuning of piezoelectric energy harvesters by magnetic force. *Smart Materials and Structures*, 21(3), 2012.

[25] R. Masana and M.F. Daqaq. Electromechanical modeling and nonlinear analysis of axially loaded energy harvesters. *Journal of Vibration and Acoustics, Transactions of the ASME*, 133(1), 2011.

[26] Y.-J. Wang, C.-D. Chen, C.-K. Sung, and C. Li. Natural frequency self-tuning energy harvester using a circular halbach array magnetic disk. *Journal of Intelligent Material Systems and Structures*, 23(8):933–943, 2012.

[27] D. Zhu, M.J. Tudor, and S.P. Beeby. Strategies for increasing the operating frequency range of vibration energy harvesters: a review. *Measurement Science & Technology*, 21(2), FEB 2010.

[28] B. Yang, C. Lee, W. Xiang, J. Xie, H.H. Johnny, K.K. Rama, P.L. Siew, and H. Feng. Electromagnetic energy harvesting from vibrations of multiple frequencies. *Journal of Micromechanics and Microengineering*, 19(3), MAR 2009.

[29] S.S. Rao. *Mechanical vibrations*. Addison-Wesley, 1995.

[30] B.P. Mann and N.D. Sims. Energy harvesting from the nonlinear oscillations of magnetic levitation. *Journal of Sound and Vibration*, 319(1-2):515–530, JAN 9 2009.

[31] D.W. Jordan and P. Smith. *Nonlinear Ordinary Differential Equations: An Introduction to Dynamical Systems*. Oxford Applied and Engineering Mathematics. Oxford University Press, 1999.

[32] J.J. Stoker. *Nonlinear Vibrations*. Pure and applied mathematics. Interscience, 1950.

[33] A.H. Nayfeh. *Perturbation methods*. Physics textbook. John Wiley & Sons, 2000.

[34] K. Worden and G.R. Tomlinson. *Nonlinearity in structural dynamics: detection, identification, and modelling*. Institute of Physics Pub., 2001.

[35] J.M.T. Thompson and H.B. Stewart. *Nonlinear dynamics and chaos*. Wiley, 2002.

[36] D.D. Quinn, A.L. Triplett, L.A. Bergman, and A.F. Vakakis. Comparing linear and essentially nonlinear vibration-based energy harvesting. *Journal of Vibration and Acoustics, Transactions of the ASME*, 133(1), 2011.

[37] S.C. Stanton, C.C. McGehee, and B.P. Mann. Reversible hysteresis for broadband magnetopiezoelastic energy harvesting. *Applied Physics Letters*, 95(17), 2009.

[38] D.A.W. Barton, S.G. Burrow, and L.R. Clare. Energy harvesting from vibrations with a nonlinear oscillator. *Journal of Vibration and Acoustics, Transactions of the ASME*, 132(2):0210091–0210097, 2010.

[39] B. Marinkovic and H. Koser. Demonstration of wide bandwidth energy harvesting from vibrations. *Smart Materials and Structures*, 21(6), 2012.

[40] G. Manla, N.M. White, and M.J. Tudor. Numerical model of a non-contact piezoelectric energy harvester for rotating objects. *IEEE Sensors Journal*, 12(6):1785–1793, 2012.

[41] B. Marinkovic and H. Koser. Smart sand-a wide bandwidth vibration energy harvesting platform. *Applied Physics Letters*, 94(10), 2009.

[42] H. Liu, C. Lee, T. Kobayashi, C.J. Tay, and C. Quan. A new s-shaped mems pzt cantilever for energy harvesting from low frequency vibrations below 30 hz. *Microsystem Technologies*, 18(4):497–506, 2012.

[43] M.F. Daqaq. Response of uni-modal duffing-type harvesters to random forced excitations. *Journal of Sound and Vibration*, 329(18):3621–3631, AUG 30 2010.

[44] F. Cottone, H. Vocca, and L. Gammaitoni. Nonlinear energy harvesting. *Physical Review Letters*, 102(8), 2009.

[45] R. Masana and M.F. Daqaq. Relative performance of a vibratory energy harvester in mono- and bi-stable potentials. *Journal of Sound and Vibration*, 330(24):6036–6052, 2011.

[46] B.P. Mann and B.A. Owens. Investigations of a nonlinear energy harvester with a bistable potential well. *Journal of Sound and Vibration*, 329(9):1215–1226, 2010.

[47] A. Erturk and D.J. Inman. Broadband piezoelectric power generation on high-energy orbits of the bistable duffing oscillator with electromechanical coupling. *Journal of Sound and Vibration*, 330(10):2339–2353, 2011.

[48] D.N. Betts, H.A. Kim, C.R. Bowen, and D.J. Inman. Optimal configurations of bistable piezo-composites for energy harvesting. *Applied Physics Letters*, 100(11), 2012.

[49] N. Cohen, I. Bucher, and M. Feldman. Slow-fast response decomposition of a bi-stable energy harvester. *Mechanical Systems and Signal Processing*, 2012.

[50] R. Masana and M.F. Daqaq. Energy harvesting in the super-harmonic frequency region of a twin-well oscillator. *Journal of Applied Physics*, 111(4), 2012.

[51] L. Gammaitoni, I. Neri, and H. Vocca. Nonlinear oscillators for vibration energy harvesting. *Applied Physics Letters*, 94(16), 2009.

[52] M.F. Daqaq. Transduction of a bistable inductive generator driven by white and exponentially correlated gaussian noise. *Journal of Sound and Vibration*, 330(11):2554 – 2564, 2011.

[53] H. Vocca, I. Neri, F. Travasso, and L. Gammaitoni. Kinetic energy harvesting with bistable oscillators. *Applied Energy*, 97:771–776, 2012.

[54] A.J. Sneller and B.P. Mann. On the nonlinear electromagnetic coupling between a coil and an oscillating magnet. *Journal of Physics D: Applied Physics*, 43(29), 2010.

[55] K. Worden and G. Manson. On the identification of hysteretic systems, part i: an extended evolutionary scheme. *Proceedings of IMAC XVIII, Conference and Exposition on Structural Dynamics, Jacksonville, Florida*, 2010.

[56] K. Worden and G. Manson. On the identification of hysteretic systems. part i: Fitness landscapes and evolutionary identification. *Mechanical Systems and Signal Processing*, 29(0):201 – 212, 2012.

[57] de Wit, C. Canudas, H. Olsson, K.J. Astrom, and P. Lischinsky. New model for control of systems with friction. *IEEE Transactions on Automatic Control*, 40(3):419–425, 1995.

[58] J.J. Brophy. *Basic electronics for scientists*. Schaum's Outline Series in Electronic & Electrical Engineering. McGraw-Hill, 1989.

[59] M.F. Daqaq. On intentional introduction of stiffness nonlinearities for energy harvesting under white gaussian excitations. *Nonlinear Dynamics*, pages 1–17, 2011.

[60] MathWorks. roots. *Matlab Help Files*, 2004.

[61] S. Goldberg. *Probability: an introduction*. Prentice-Hall mathematics series. Dover Publications, 1986.

[62] D.J.C. MacKay. *Information Theory, Inference, and Learning Algorithms*. Cambridge University Press, 2003.

[63] R.M. Neal. Probabilistic inference using markov chain monte carlo methods, 1993.

[64] A.T. Fuller. Analysis of nonlinear stochastic systems by means of the fokker-planck equation. *International Journal of Control*, 9(6), 1969.

[65] T.K. Caughey. Derivation and application of the fokker-planck equation to discrete nonlinear dynamic systems subjected to white random excitation. *Journal of the Acoustical Society of America*, 35(11), 1963.

[66] K.A. Stroud and D.J. Booth. *Advanced Engineering Mathematics*. Palgrave Macmillan Limited, 2011.

[67] C.W.S. To. *Nonlinear random vibration: analytical techniques and applications*. Advances in Mechanical Engineering Series. Swets & Zeitlinger Publishers, 2000.

[68] Y.K. Lin and G.Q. Cai. *Probabilistic structural dynamics: advanced theory and applications*. McGraw-Hill, 1995.

[69] T.K. Caughey and F. Ma. The exact steady-state solution of a class of non-linear stochastic systems. *International Journal of Non-Linear Mechanics*, 17(3):137–142, 1982.

[70] M. Abramowitz and I.A. Stegun. *Handbook of mathematical functions with formulas, graphs, and mathematical tables*. Number v. 55, no. 1972 in Applied mathematics series. U.S. Govt. Print. Off., 1964.

[71] R.H. Good. *Classical electromagnetism*. Number v. 1 in Saunders golden sunburst series. Saunders College Pub., 1999.

[72] L.C. Rome, L. Flynn, E.M. Goldman, and T.D. Yoo. Biophysics: Generating electricity while walking with loads. *Science*, 309(5741):1725–1728, 2005.

[73] E. Papatheou, P.L. Green, V. Racic, Brownjohn J.M.W., and N.D. Sims. A short investigation of the effect of an energy harvesting backpack on the human gait. *Proceedings of SPIE 2012, Smart Structures/NDE, San Diego, California*, 2012.

[74] L. Mateu and F. Moll. Optimum piezoelectric bending beam structures for energy harvesting using shoe inserts. *Journal of Intelligent Material Systems and Structures*, 16(10):835–845, 2005.

[75] C.R. Saha, T. O'Donnell, N. Wang, and P. McCloskey. Electromagnetic generator for harvesting energy from human motion. *Sensors and Actuators, A: Physical*, 147(1):248–253, 2008.

[76] E. Papatheou and N.D. Sims. Developing a hardware in-the-loop simulator for a backpack energy harvester. *Journal of Intelligent Material Systems and Structures*, 23(7):827–835, 2012.

[77] I. Neri, , F. Travasso, R. Mincigrucci, H. Vocca, F. Orfei, and L. Gammaitoni. A real vibration database for kinetic energy harvesting application. *Journal of Intelligent Material Systems and Structures*, 2012.

[78] Y. Zhang and C.S. Cai. A retrofitted energy harvester for low frequency vibrations. *Smart Materials and Structures*, 21(7), 2012.

[79] P.L. Green, K. Worden, K. Atallah, and N.D. Sims. The effect of duffing-type nonlinearities and coulomb damping on the response of an energy harvester to random excitations. *EuroMech Colloquium 530: Structural Control and Energy Harvesting - Bristol, UK, 25-27 July 2011*, 2011.

[80] P.L. Green, K. Worden, K. Atallah, and N.D. Sims. The effect of duffing-type non-linearities and coulomb damping on the response of an energy harvester to random excitations. *Journal of Intelligent Material Systems and Structures*, 0(0):0, 2012.

[81] P.L. Green, K. Worden, K. Atallah, and N.D. Sims. The modelling of friction in a randomly excited energy harvester. *Proceedings of ISMA 2012, Conference on Noise and Vibration Engineering, Leuven, Belgium, 20-22 September 2010*, 2012.

[82] P.L. Green, K. Worden, K. Atallah, and N.D. Sims. The benefits of duffing-type nonlinearities and electrical optimisation of a mono-stable energy harvester under white gaussian excitations. *Journal of Sound and Vibration*, 331(20):4504 – 4517, 2012.

[83] P.L. Green, K. Worden, K. Atallah, and N.D. Sims. The benefits of duffing-type nonlinearities and electrical optimisation of a randomly excited energy harvester. *Proceedings of IMAC XXX, Conference and Exposition on Structural Dynamics - Jacksonville, Florida, 30 Jan - 2 Feb, 2012*, 2012.

[84] P.L. Green, E. Papatheou, and N.D. Sims. Energy from human motion: an evaluation of current nonlinear energy harvesting solutions. *Proceedings of MPSVA 2012, Conference on Modern Practice in Stress and Vibration Analysis - Glasgow, 29-31 August 2012*, 2012.

[85] K. Worden and J.J. Hensman. Parameter estimation and model selection for a class of hysteretic systems using bayesian inference. *Mechanical Systems and Signal Processing*, 2012.

[86] A. Saltelli, M. Ratto, T. Andres, F. Campolongo, J. Cariboni, D. Gatelli, M. Saisana, and S. Tarantola. *Global Sensitivity Analysis: The Primer*. Wiley, 2008.